Performance of Full-Scale Reinforced Concrete Columns Subjected to Extreme Earthquake Loading

A Dissertation
SUBMITTED TO THE FACULTY OF
UNIVERSITY OF MINNESOTA
BY

Alireza Nojavan

IN PARTIAL FULFILLMENT OF THE REQUIREMENTS
FOR THE DEGREE OF
DOCTOR OF PHILOSOPHY

Advisor:
Arturo E. Schultz

December 2015

Acknowledgements

This project was supported by the National Science Foundation under award No. CMMI-10041633. I would like to acknowledge the Department of Civil, Environmental and Geo-Engineering of the University of Minnesota for the Departmental Fellowship Award.

I would like to also acknowledge all who made this research possible. First and foremost, I would like to express my extreme gratitude to my advisor, Prof. Arturo E. Schultz for his support, and valuable advice and directions during the course of my research. He was not only a kind teacher, but also a source of motivation. I would also like to acknowledge Prof. Catherine French, Prof. Lev Khazanovich, and Prof. Ryan Elliott for serving on my thesis committee and for their helpful comments. Special thanks are due to Prof. Shih-Ho Chao at University of Texas, Arlington (UTA) for directing the experimental part of this project and for his comments.

The experimental part of this research could not be possible without help from several others. I would like to acknowledge help from the staff at the MAST Lab of the University of Minnesota. Special thanks are due to Paul Bergson, Rachel Gaulke, and Mary Vancura who helped during all stages of the tests. Michael Boldischar is thanked for his help during setting up cameras and recording and uploading test data. I am also thankful to Tanner Swenson, Charles Vermace, Lauren Snyder, Anton Tillmann and Andrew Morgan for their help during assembly, instrumentation, and testing of the specimens. Help of many others at UTA in construction of the specimen is also appreciated.

Dedicated to

my parents and my wife

ABSTRACT

Seven full-scale reinforced concrete (RC) columns were tested at the Multi-Axial Subassemblage Testing (MAST) Laboratory of the University of Minnesota to investigate their performance under extreme seismic events that would produce near-collapse conditions. One of the goals of the tests was to investigate any potential differences in performance with column size, thus, the test specimens were larger than nearly all of the columns tested previously. In order to investigate the adequacy of current provisions, the specimens were designed according to seismic provisions of ACI 318-11 and featured two different cross sections (36×28 in. and 28×28 in.). Another goal of the program was to investigate the influence of loading history, thus the column specimens were subjected to several large displacement loading protocols, including monotonic and uniaxial and biaxial cyclic loading protocols. The last overall goal of the program was to investigate the post-peak behavior of the specimens at near-collapse conditions, hence loading on the specimens continued beyond the stopping criteria in previous tests until the specimens exhibited severe strength loss and stiffness degradation.

Results from these tests were combined with the available dataset of RC column tests to study the effects of cross-sectional size on parameters representing seismic performance of columns including moment capacity, effective stiffness, drift capacity, displacement ductility, and reinforcing bar buckling. It was revealed that unlike the other parameters, specimens featuring larger cross-sectional depths are more prone to in-plane bar buckling, a failure mechanism that has never been reported during previous tests of RC columns.

Unlike outward buckling of bars, in-plane bar buckling is not generally controlled by confining reinforcement; rather it is the concrete surrounding the bars that restrain them from in-plane buckling. To better understand this phenomenon, finite element (FE) models of isolated bars as well as a three-dimensional (3D) FE model of the lower portion of the tested specimens were analyzed. A parametric study indicates that concrete compressive strength, bar size and overall cross-sectional size of the columns can affect bar buckling while the effects of longitudinal bar and tie spacing are minor.

The evolution of damage during application of the various loading protocols was quantified using several cumulative and noncumulative damage index models. In addition, observed visual damage to the specimens was used to assess calculated damage indices based on different models. Calculated and measured damage quantities were considered in combination with the lateral force-deformation cyclic envelope, strength loss, stiffness reduction, and hysteretic energy dissipation of the specimens to study the effects of applied loading protocols on the performance of tested column specimens.

Table of Contents

List of Tables

List of Figures

CHAPTER 1

INTRODUCTION

1.1. BACKGROUND

The recently advanced performance-based design philosophy anticipates a structure to dissipate energy during an earthquake and accepts certain levels of damage depending on the expected risk of occurrence of earthquakes during their lifetime, and the importance of the structure. In fact, there are different structural design objectives in the performance-oriented seismic design philosophy, and these are based on various levels of accepted damage (i.e., limit states) under distinct levels of earthquake loads that are expected during lifetime of the structure. Estimated structural demands (e.g. required strength, or stiffness) to meet the structural objectives are then compared against capacity of the structure (e.g. available strength, stiffness, or deformation capacity). Evaluation of structural capacity, on the other hand, relies primarily on numerical modeling tools that are calibrated against test results. In the case of reinforced concrete (RC) columns, the test results are used to estimate lateral load and deformation capacities under simulated seismic loadings.

A large number of experimental efforts have been undertaken on RC columns to enhance knowledge on their performance under gravity and lateral loads, and to develop and improve design code provisions. Properties of more than 300 of such tests are collected in the ACI 369 Rectangular Column Database (Ghannoum et al., 2012) as well as in the PEER structural performance database (Berry, Parrish, & Eberhard, 2004). Primary variables in these tests include axial load ratio, lateral loading scheme, cross-sectional dimensions, shear span–to-depth ratio, and amount and distribution of transverse reinforcement.

While many tests have been conducted on RC columns, their performance, specifically in the post-peak region, is not completely understood. This lack of knowledge in the softening regime of response for the columns is mainly due to the fact that almost all of the previous tests were terminated once the specimens lost 20% or less of their lateral load capacity. While an arbitrary definition of structural failure can be tied to the aforementioned condition, RC columns can still survive collapse when loaded beyond this arbitrary point of failure. Therefore, to investigate the seismic performance of RC columns and to generate and calibrate component models, especially at the near-collapse stage, RC column specimens are required to undergo large deformation levels under which they exhibit significant strength loss (i.e., 50% or more) and post-peak behavior (i.e., up to residual strengths 50% or less of the peak resistance). Development of such improved models—which is important, according to the National Institute of Standards and Technology (NIST) and the National Earthquake Hazards Reduction Program (Advisory Committee on Earthquake Hazards Reduction, 2008; National Institute of Standards and

Technology, 2009)—requires that the shortcomings in available RC column test data be addressed.

Additionally, many of the previous tests were conducted on columns with smaller dimensions than those currently used in mid- or high-rise buildings mainly due to limitations of the testing facilities. The average cross-sectional depth of the rectangular RC columns in the more recent database (i.e., ACI 369 Rectangular Column Database, 2012) is 12.5 in. (318 mm) with lower 5% and upper 95% bounds of 6.3 in. (160 mm) and 21.65 in. (550 mm), respectively. More specifically, an analysis of these databases indicates that columns with flexural failure modes feature a maximum cross-sectional dimension of 24 in. (610 mm). While these tests provide a valuable dataset for RC columns, a careful study is required to assess the validity and applicability of their results to estimate seismic performance of actual columns with larger dimensions.

Last but not least, unlike RC bridge columns, there are limited previous experimental efforts that have focused on the effects of applied loading protocols on RC building columns and during which similar test specimens were subjected to monotonic and cyclic loading protocols. Considering the uncertainty in the amplitude and number of cycles that RC columns in a building structure may sustain during an earthquake, their performance under distinct simulated loading protocols is needed in order to more accurately estimate their force-deformation (i.e., “backbone”) capacity curves, as well as to accurately characterize damage during the various stages of loading.

1.2. RESEARCH OBJECTIVES AND SUMMARY

To enhance understanding of the behavior of RC columns that are representative of those commonly used in mid- and high-rise buildings and to address the shortcomings of the aforementioned data set for rectangular RC columns, eight full-scale columns were tested as a part of this research at the Multi-Axial Subassemblage Testing (MAST) Laboratory of the University of Minnesota. These column specimens were subjected to a constant axial load and various loading schemes, including uniaxial and biaxial symmetric cyclic, near-collapse unsymmetric cyclic, and single-cycle loading protocols. The protocols were designed to attain drift ratios exceeding 10% such that the specimens would lose most of their lateral loading capacity and exhibit significant loss of flexural strength and stiffness. The specimens were representative of actual columns in the ground floor of a 20-story building located in a high seismic region and featuring two different cross-sectional dimensions (36×28 in. and 28×28 in.), both which are larger than all flexure-critical columns tested previously.

Results from the tests that were conducted at the MAST Lab as part of this research were utilized along with those from previous tests that are included in the ACI 369 Rectangular Column Database (2012) to investigate the effect of cross-sectional size of RC columns, and on the parameters that represent their seismic performance including the moment capacity, effective stiffness, drift capacity, ductility, and drift at the onset of buckling.

During the tests that were carried out at the MAST Lab, a failure mechanism was observed that has never been observed in previous tests of RC columns. In this failure mechanism, reinforcing bars buckled parallel to the face of the columns, which is referred to as in-plane buckling in this study, while the common assumption is that longitudinal bars would only buckle in the outward direction (i.e., perpendicular to the column face). Unlike outward buckling, transverse ties were observed to have little effect in preventing in-plane buckling of bars. This unobserved failure mechanism is investigated numerically using 3D FE analysis of the columns to obtain a better understanding of the column characteristics that affect it.

Last but not least, RC columns experienced severe damage during these tests resulting in significant strength loss and stiffness degradation of the specimens. The extent of damage in each specimen was calculated using several well-known damage index models for RC elements. Measured damage indices were then compared against observed damage during tests at the MAST Lab. Finally, measured and observed damage to the specimens were considered along with cyclic force-deformation response, and energy dissipation of the specimens to investigate the effect of the applied loading protocols.

1.3. THESIS ORGANIZATION

Chapter 2 describes characteristics of the tests that were conducted as part of this research at the MAST Lab including details of specimens, material properties, instrumentation, loading protocols, and brief test observations. Detailed information regarding each test as well as measured response of specimens during loading are made available via digital object identifier (DOI) links provided in the chapter. While the current study focuses on the behavior of seven columns that were constructed with normal strength concrete, this chapter also presents brief information regarding a specimen that was constructed with ultra-high-performance fiber-reinforced concrete (UHP-FRC) and tested as part of the experimental program. A detailed information regarding this specimen and its behavior during the test can be found elsewhere (Palacios, 2015).

A study on the effect of cross-sectional size of the RC columns on their seismic performance is investigated in Chapter 3 by analyzing moment capacity, effective stiffness, drift capacity, displacement ductility, and longitudinal bar buckling. For the purpose of this analysis, tested column specimens that are included in the ACI 369 Rectangular Column Database (2012) as well as those constructed with normal strength concrete (i.e., specimens SP1 – SP7) and tested as part of this research are considered.

In-plane buckling of longitudinal bars, an unobserved failure mechanism during previous tests, is described in Chapter 4. The chapter also presents information regarding the FE modeling of isolated bars, as well as that related to the 3D FE modeling of the lower portion of tested specimens. Results from a parametric study on the effects of parameters that control in-plane buckling of reinforcing bars is also included.

In Chapter 5, the evolution of damage during each test is quantified by cumulative and noncumulative damage index modes. Also, the observed damage are categorized and compared against measured damage indices. The chapter concludes by presenting the effect of loading protocols on the performance of column specimens.

Finally, a summary of this research and conclusions obtained are presented in Chapter 6. Based on these conclusions, recommendations for future study are offered.

CHAPTER 2

A NEW DATASET FOR FULL-SCALE REINFORCED CONCRETE COLUMNS UNDER COLLAPSE-CONSISTENT LOADING PROTOCOLS[1]

2.1. SUMMARY

A series of eight full-scale reinforced concrete column tests was recently carried out at the NEES (Network for Earthquake Engineering Simulation) Multi-Axial Subassemblage Testing (MAST) site at the University of Minnesota as part of a National Science Foundation (NSF) NEES research program. The tests were conducted to address the shortcomings in the available database of reinforced concrete (RC) columns tested with large drift ratios under monotonic and cyclic loading protocols. The specimens were designed based on ACI 318-11 and featured two different cross-sectional dimensions, both larger than nearly all of the columns tested previously. They were subjected to several large displacement loading protocols, including a monotonic and a cyclic biaxial loading

---

[1] Nojavan, A., Schultz, A.E., Haselton, C., Simathathien, S., Liu, X., and Chao, S-H. (2015). “A New Dataset for Full-Scale RC Columns under Collapse-Consistent Loading Protocols,” Earthquake Spectra, EERI, 31(2): 1211-1231.

protocol. Also, to investigate the effectiveness of novel materials, one specimen was constructed with ultra-high-performance fiber-reinforced concrete (UHP-FRC). This chapter presents a description of and potential uses for the data set that is made accessible via a digital object identifier (DOI) (data set DOI: 10.4231/D33T9D65T).

2.2. INTRODUCTION

One of the primary goals of conducting tests on RC columns is to enhance knowledge of their behavior and to develop component models that can predict the columns' seismic performance in a structural system. For the purpose of seismic performance–based design, improved component models are required to capture the post-peak behavior of columns more accurately. Development of such improved models—which is important, according to the National Institute of Standards and Technology (NIST) and the National Earthquake Hazards Reduction Program (Advisory Committee on Earthquake Hazards Reduction (ACEHR), 2008; National Institute of Standards and Technology (NIST), 2009)—requires that the shortcomings in available RC column test data be addressed.

A large number of experimental investigations have been carried out to understand the behavior of RC columns subjected to various loading protocols. The properties of 326 tests on rectangular RC columns are presented by (Ghannoum et al., 2012). Primary variables in these tests include axial load ratio, lateral loading scheme, cross- sectional dimensions, shear span–to-depth ratio, amount and distribution of transverse reinforcements, and bond-slip characteristics. Figure 2.1 illustrates the maximum

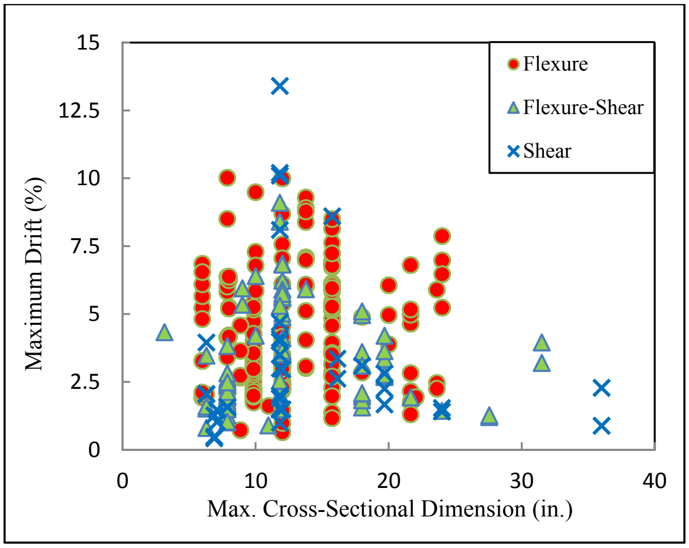

Figure 2.1. Properties of Previous Tests on Rectangular RC Columns.

cross-sectional dimension, maximum drift ratio, and failure mode of column specimens in previous experiments. It shows that columns with flexural failure modes feature a maximum cross-sectional dimension of 24 in. A few of the smaller specimens were loaded to drift ratios of 10% or more; columns with larger cross-sectional dimensions were loaded to drift ratios smaller than 5% because they failed in more brittle modes, either in shear or in flexure-shear.

There are no data on flexure-dominated column sections of sufficiently large dimensions to realistically represent those used in the lower stories of multistory buildings and loaded to sufficiently large drifts (~10%) to elucidate their degradation characteristics for calibration of collapse simulation models. Therefore, to investigate the seismic performance of flexure-dominated RC columns and to generate and calibrate component models, especially at the near-collapse stage, specimens that are representative of those typical in tall buildings are required to undergo large deformation levels under which they exhibit significant strength loss (i.e., 80%) and post-peak behavior (i.e., up to residual strengths equal to approximately 20% of peak resistance). Several studies have explored the effects of loading protocols on the behavior of RC members (Applied Technology Council (ATC), 2009a; Dhakal & Fenwick, 2008; Ingham, Liddell, & Davidson, 2001; William C. Stone, Cheok, & Stanton, 1995; Takemura & Kawashima, 1997). However, in only a limited number of investigations were identical specimens placed under both monotonic and cyclic loading protocols (Applied Technology Council (ATC), 2009a; Haselton, Liel, Lange, & Deierlein, 2008). Also, in many experiments column specimens were subjected to symmetric cyclic reversals of lateral displacements, in addition to either a constant (Dawn E. Lehman & Moehle, 1998; Jaradat, McLean, & Marsh, 1998; Esmaeily-Gh & Xiao, 2002) or a variable (Gilbersten & Moehle, 1980; Kreger & Linbeck, 1986) axial load. However, in an actual earthquake small loading cycles are often followed by large unsymmetric displacement excursions that can lead to major plastic deformations in one direction and in turn to structural collapse due to P-delta effect. Therefore, it is necessary to investigate the effect of unsymmetric cyclic loading protocols that represent what columns will experience during earthquakes.

To address the shortcomings of the available data set for rectangular RC columns, a series of eight full-scale columns were subjected to a constant axial load and various loading schemes, including uniaxial and biaxial symmetric cyclic, near-collapse unsymmetric cyclic, and single-cycle loading protocols. The protocols were designed to attain drift ratios exceeding 10% such that the specimens would lose most of their lateral loading capacity and exhibit significant loss of flexural strength. The specimens were representative of actual columns in the ground floor of a 20-story building located in a high seismic region and featuring two different cross-sectional dimensions (36×28 in. and 28×28 in.) that are larger than all flexure-critical columns tested previously.

In a related matter, limited investigation was conducted on the helpful effects of ultra-high-performance fiber-reinforced concrete (UHP-FRC) in improving damage tolerance when applied in large column specimens. To study the effects of this emerging innovative material in enhancing the seismic performance of columns, one of the specimens was constructed with UHP-FRC consisting of a mixture of high-strength steel microfibers and concrete with a compressive strength of 25 ksi at 28 days.

The experimental data recorded during the eight tests are available through DOI links provided in this paper. The DOIs also contain all required pre- and post-test information, including assembly of the specimens, cross-sectional details for each specimen, material properties, location and orientation of the sensors and instrumentations (LVDTs, string pots, tiltmeters, and strain gages), and video and still images for each specimen. The data set is provided in complete accordance with available databases such as the ACI 369 Rectangular Column Database (Ghannoum et al., 2012), and the Pacific Earthquake Engineering Research center (PEER) Structural Database (Berry et al., 2004). The data set described here will provide an opportunity for researchers to explore the performance of RC columns in various cyclic loading conditions. It will also help researchers enhance their knowledge of the seismic performance of full-size columns under severe loading conditions and to employ it to develop enhanced computational tools and seismic code provisions for structural design.

2.3. TEST SETUP

Eight full-scale RC columns with two different cross-sectional dimensions were built and tested under distinct axial load ratios and various lateral loading protocols. All of the specimens were constructed and cast in an upright position in the Civil Engineering laboratory of the University of Texas at Arlington, Texas, and were tested at the Multi-Axial Subassemblage Testing (MAST) laboratory of the University of Minnesota. The six-degree-of-freedom (6-DOF) loading system at the MAST lab is capable of applying up to 1,320 kips of vertical force, 880 kips of lateral force in two orthogonal horizontal directions, 8,910 kip-ft of moments, and maximum displacements of ±20 in: and ±16 in: in the vertical and horizontal directions, respectively (French et al., 2004). The loading crosshead of the MAST lab is controlled by an MTS 6-DOF controller that computes the required movement for each of the actuators (in their current configuration and along their local coordinate system) to apply a desired boundary condition to the specimen considering the effect of geometric nonlinearity. Each DOF defining the position of the crosshead can be controlled either in displacement or in force mode, and the global coordinate system of the crosshead remains constant regardless of the movement of the specimen. Users specify the history of displacement or load for each of the six global DOFs, and the controller computes the required forces or displacements of the local DOFs for each of the actuators.

Figure 2.2 illustrates the assembly of a specimen under the loading crosshead at the MAST lab and the definition of the MAST and specimen coordinate systems.

The specimens were oriented at a 45° angle (X′ -Y′ axes) with respect to the MAST lab primary coordinate system (X-Y axes) to provide a larger stroke capacity of ±22.6 in. in the diagonal direction (X ′ or Y′) for the actuators, as opposed to ±16 in. stroke capacity in the X (or Y) direction. The test specimen comprised the lower portion of a column in double curvature plus a short segment above the point of inflection such that the latter was located 10 in. below the soffit of the top block of the specimen. To keep the inflection point at the desired location, a flexural moment was introduced by the crosshead on top of the specimen (Figure 2.3).

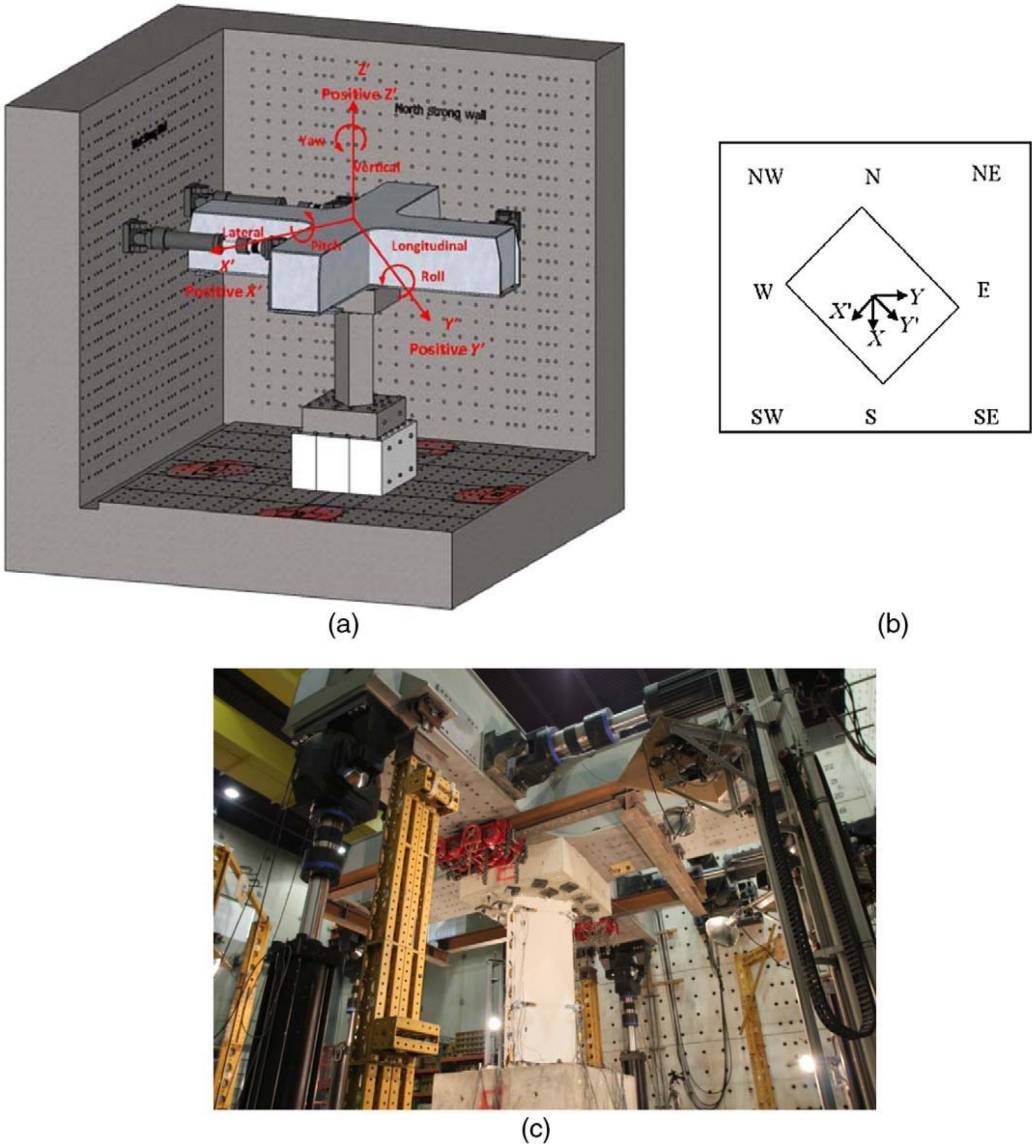

Figure 2.2. (a) Assembly of the Specimen under the Loading Crosshead (Vertical Actuators are not Shown for Clarity) (b) Definition of the Coordinate System and (c) Specimen Connection to the Crosshead.

2.4. SPECIMENS

The specimens were representative of the lower portion of a column bent in double curvature (Figure 2.3) at the ground floor of a 20-story prototype moment-resistant frame building. Columns were designed according to seismic provisions in Chapter 21 of ACI 318-11 (ACI Committee 318, 2011) and were designated as perimeter frame (PF) or space frame (SF) depending on their location in the floor plan, representing an interior column along the perimeter frame and an interior column in a space frame, respectively. The PF specimens had a rectangular cross section of 36×28 in. with 16 #9 longitudinal bars; the SF specimens featured a 28 in. square cross section with 12 #8 longitudinal bars

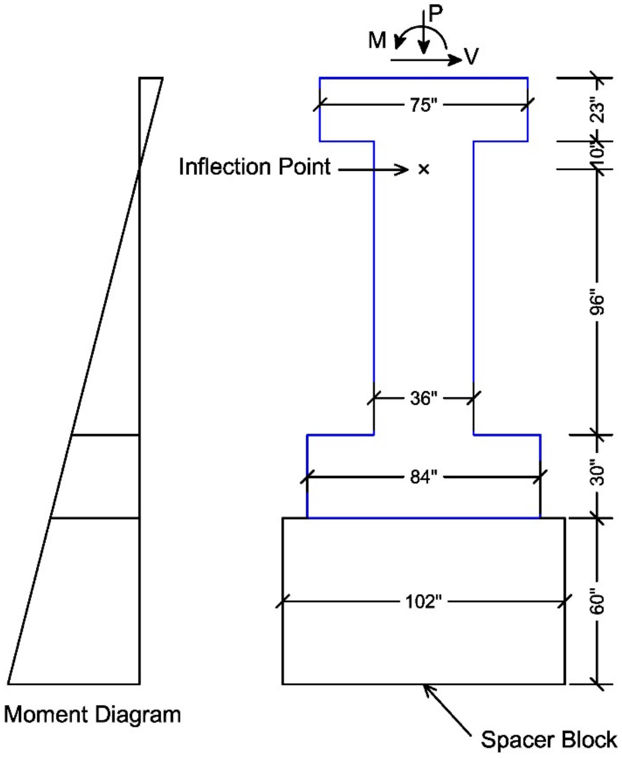

Figure 2.3. Location of the Inflection Point and Definition of the Top Moment

(Figure 2.4). In both specimen types, the longitudinal bars were tied with closed hoops bent from #5 bars and placed with 5- or 6-in. center-to-center spacing depending on their location relative to the column base. The column portion of all specimens were 106 in. tall and were cast along with an 84×84×30 in. footing block and a 75×75×23 in. loading (top) block. The footing block enabled connection to a post-tensioned, three-piece concrete base block of 102×102×60 in. dimensions, which itself was attached to the lab strong

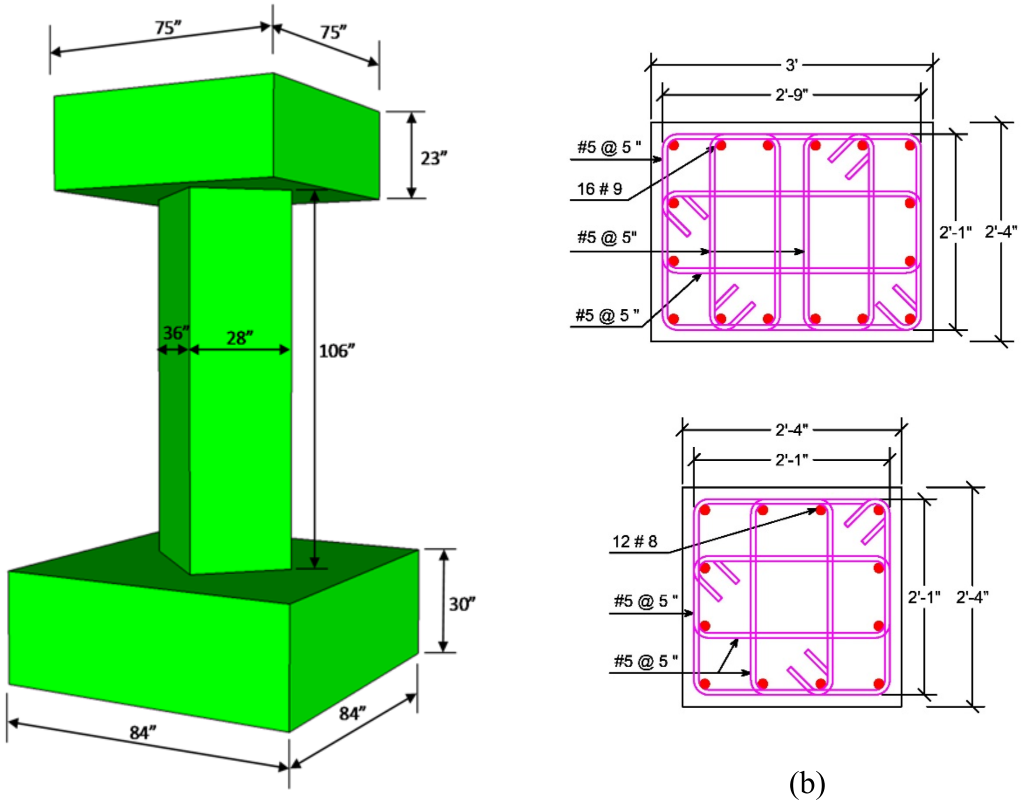

(a)

(b)

Figure 2.4. (a) 3D Rendering of PF Specimens and (b) Cross-Sectional Detailing of PF (Top) and SF Specimens (Bottom)

floor using 1.5 in. ASTM A193 Grade-B7 threaded rods with a minimum yield strength of 125 ksi. The loading block connected to the MAST crosshead using the same threaded rods. The entire testing assembly had a height of 219 in. under the crosshead. Figure 2.4 illustrates a typical PF specimen along with cross-sectional details of both specimen types.

2.5. MATERIALS

The specimens were built using ASTM A706 (2003) Grade-60 reinforcing steel and normal-strength, normal-weight concrete except the last specimen (SP8), which was built with UHP-FRC. The concrete used for the specimens was self-compacting with a maximum aggregate size of 3/8 in. and a specified nominal 28-day compressive strength of 5,000 psi. The concrete strength of each specimen was determined using standard cylinder tests according to ASTM C39C (2003). For each specimen, three 4×8 in. cylinders were tested on the day the specimen was tested. The concrete mix design for the column specimens is presented in Table 2.1. Average measured specimen compressive strengths on the testing day are presented in Table 2.2. The UHP-FRC specimen was constructed with concrete with a compressive strength at 28 days of 25 ksi along with a 3% volume fraction of high-strength steel microfibers to improve its ductility and seismic performance.

Uniaxial tensile tests were conducted on steel coupons according to ASTM A370-03a (2003) to measure the mechanical properties of the steel bars. Samples of 18 in. lengths were cut from each heat of reinforcing bars. The samples were instrumented with an 8-in. gage length and pulled at a constant rate of 0.125 in/min. using a 200-kip universal testing machine with hydraulic grips. In addition to the applied force and displacement, strains were captured by an extensometer located at the middle of the gage length of each sample. Mechanical properties of the longitudinal and transverse bars are presented in Table 2.2, where b × h show the cross-sectional dimension of each specimen and f_y, f_u, and ε_u represent reinforcement yield, ultimate stress, and ultimate strain, respectively.

Table 2.1. Normal Strength Concrete Mix-Design

Weight (lb) for 1 Cu. Yd. of Normal Strength Concrete					
Cement	Sand	Coarse Aggregate (3/8")	Water	W/C	Total Weight
748	1227	1666	404	0.54	4045

Table 2.2. Material Properties of the Specimens

Spec.	$b \times h$ (in.)	f_c (psi)	Age of testing (days)	Longitudinal Bars				Transverse Bars			
				Bar Size	f_y (ksi)	f_u (ksi)	ε_u	Bar Size	f_y (ksi)	f_u (ksi)	ε_u
SP1	36×28	4,860	28	9	74	112	0.2	5	69	104	0.12
SP2	36×28	5,400	28	9	74	112	0.2	5	66	108	0.12
SP3	36×28	5,300	28	9	74	112	0.2	5	65	105	0.12
SP4	36×28	5,370	20	9	74	112	0.2	5	65	105	0.12
SP5	28×28	5,270	21	8	59	102	0.15	5	64	103	0.12
SP6	36×28	4,610	19	9	74	112	0.2	5	65	105	0.12
SP7	36×28	4860	14	9	74	112	0.2	5	62	103	0.11
SP8	28×28	23000	24	8	59	102	0.15	5	63	104	0.12

2.6. INSTRUMENTATION

Linear variable differential transformers (LVDTs) were installed in a vertical configuration on each specimen to measure column deflections from which curvature could be calculated. Also, horizontal LVDTs and diagonal string potentiometers (pots) were installed to measure specimen shear deformation at 36 and 96 in. from the column base, as shown in Figure 2.5. Additional string pots were connected to the specimen at 96 in. from the top of the base block to track displacement at the inflection point. A tiltmeter was installed at this point to measure specimen rotations. Strain gages were used to record strains on longitudinal bars and transverse hoops and in the concrete core in each specimen; their location is shown on Figure 2.6. In the figure, "XX" after the each strain gage name refers to its specific location along the specimen height. The total number of different sensor types for each specimen is given in Table 2.3.

Besides the sensors, high- and extra-high-resolution still cameras as well as high-resolution video cameras were applied during each test. Still images were captured by eight Canon SX110IS 9.0-megapixel still-image cameras located at two different elevations on four telepresence towers at the four corners of the MAST strong floor, as shown in Figure 2.7. Also, high-definition (HD) videos were recorded by eight Sony EVI-HD1 video cameras located next to the image cameras on telepresence towers. Each still camera and video recorder was adjusted to focus on a single face of the column specimens. Still images were taken either at every 1-in. displacement of the crosshead or at the peak displacement of each drift cycle, whereas videos were recorded continuously

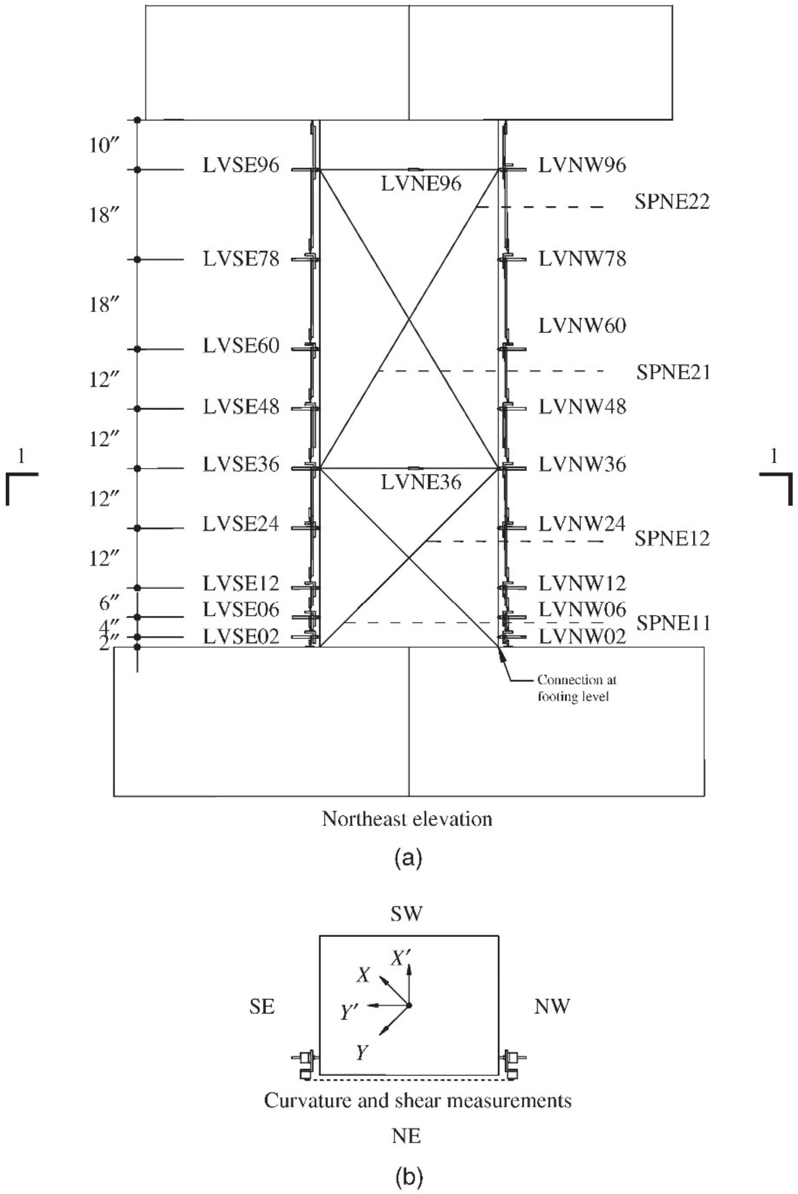

Figure 2.5. LVDTs (LV) and String Pots (SP): (a) Location along the Height and (b) Section 1-1

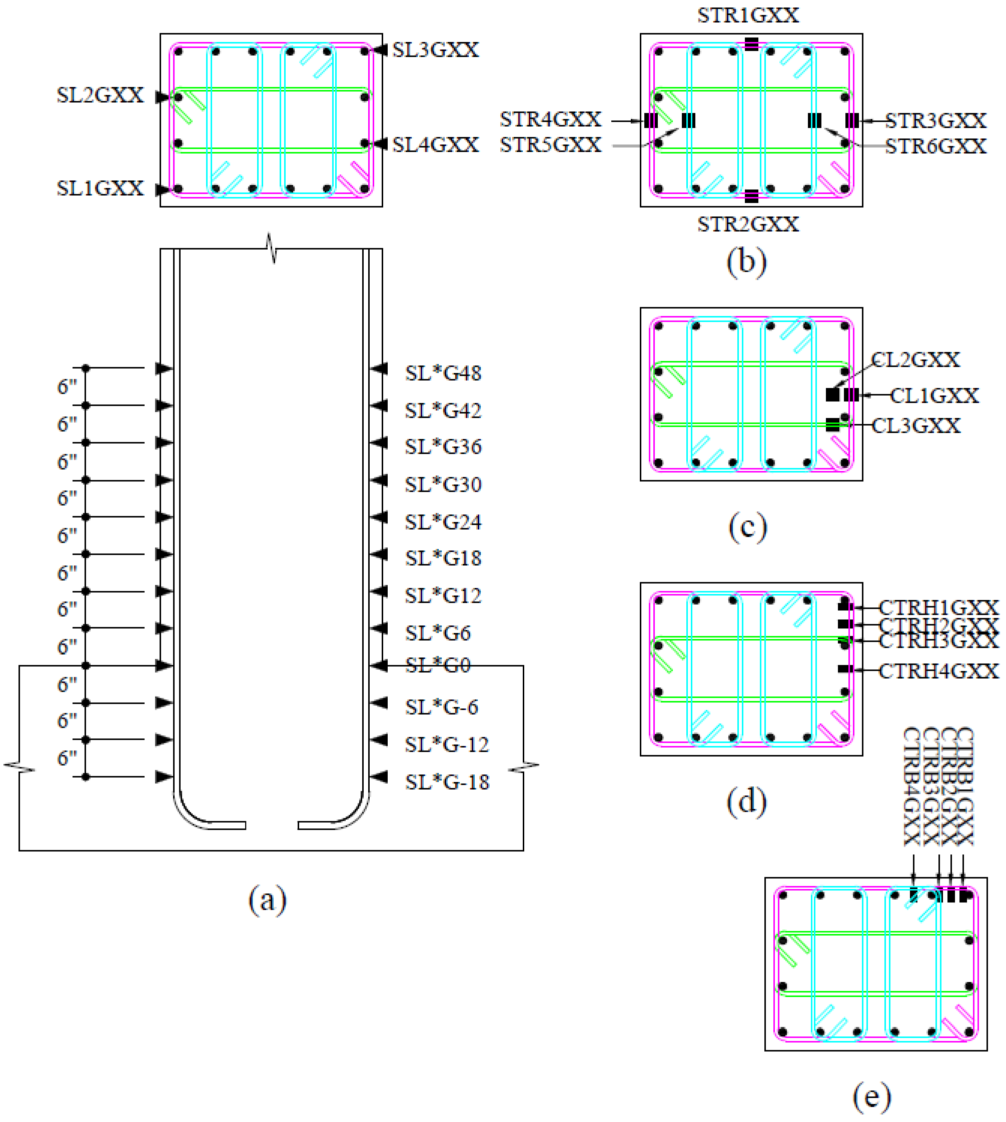

Figure 2.6. Locations of Strain Gages: (a) on Longitudinal Bars (b) on Transverse Hoops (c) and (d) Horizontally within the Concrete and (e) Vertically within the Concrete

Table 2.3. Number of Different Types of Sensors for Each of the Specimens

Spec.	LVDT		String Pots		Strain Gages				Tiltmeter	**Total**
	Vert.	Horiz.	Diag.	Horiz.	Long. Bars	Hoops	Horiz. (in concrete)	Vert. (in concrete)		
SP1	20	8	4	2	52	36	34	7	-	**163**
SP2	20	8	4	2	53	36	34	7	1	**165**
SP3	20	8	4	2	48	36	42	7	1	**168**
SP4	20	8	4	2	52	42	34	11	1	**174**
SP5	20	8	4	2	68	36	34	9	1	**182**
SP6	20	8	4	2	68	36	32	10	1	**181**
SP7	38	10	8	4	100	32	36	12	-	**240**
SP8	20	8	4	2	64	34	38	11	1	**182**

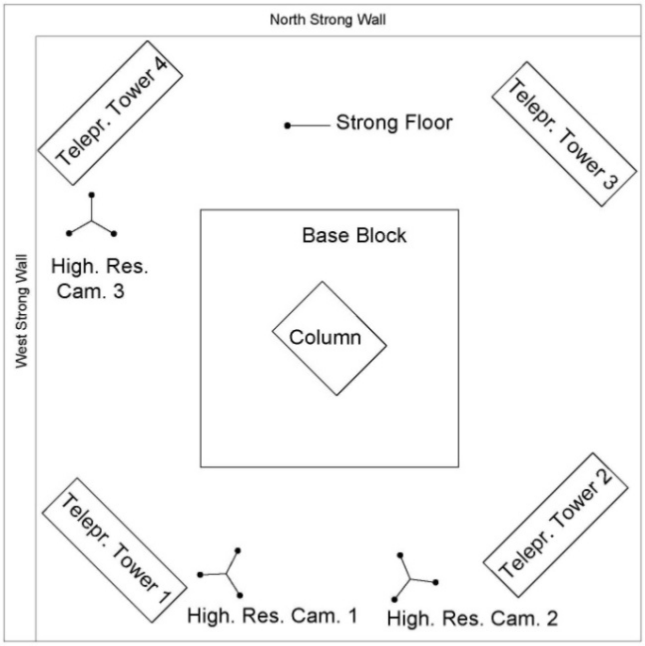

Figure 2.7. Location of the Telepresence Towers and High-Resolution Cameras at the MAST Lab

during the tests. Additionally, three high-resolution cameras, including two Nikon D600 24.3-megapixel digital SLRs and a Nikon D3200 24.2-megapixel digital SLR captured high-resolution still images continuously during each test at a rate of one image per 10 s. Moreover, time-lapse images were captured by a 6-megapixel Canon Powershot Pro Series S3 every 30 s during the test and every 5 min during specimen preparation.

Table 2.4 summarizes the amount of visual data (still images and videos) recorded during each test. Contact sensors (mini-accelerometers) and air-coupled ultrasonic transmitters were used on specimens SP6, SP7, and SP8 for nondestructive evaluation (NDE) based on ultra- sonic testing. A nondestructive testing (NDT) technique was conducted on SP6 using ultrasonic shear-wave tomography, known as MIRA, to detect internal defects in the cross section. Discussion of the applied ultrasonic methodology and the results obtained are discussed elsewhere.

Table 2.4. Amount of Image and Video Data Recorded During Each Test (GB)

Sp.	Still and timelapse images	Extra High Resolution images	Total images	Videos	Total image and video
SP1	7.7	75.4	83.1	33.97	**117.0**
SP2	6.7	286.1	292.8	24.1	**316.9**
SP3	8.1	112	120.1	16.9	**137.0**
SP4	7.8	128.7	136.5	17.3	**153.8**
SP5	6.2	106.2	112.4	15.8	**128.2**
SP6	4.4	41.3	45.7	10.0	**55.7**
SP7	10.2	200.9	211.1	41.5	**252.6**
SP8	7.7	153.8	161.5	30.7	**192.2**

2.7. LOADING PROTOCOLS

The RC specimens were subjected to six different loading protocols to investigate the effect of various seismic loading events. At the beginning of each test, an axial load was applied and its magnitude and vertical orientation were kept constant during the tests using the eight actuators that drive the MAST crosshead. The movement of each actuator is computed internally by the MTS controller to ensure the commands defined for the global DOFs at the crosshead. Therefore, there is no need for the user to modify the movement to account for geometric nonlinearity. The magnitude of the axial load for the specimens constructed with normal-weight concrete was selected according to the estimated structural demands of the PF and SF columns in the prototype structure and with consideration of their cross-sectional dimensions and concrete strengths such that the axial load ratio (P/f'_cA_g) was 0.15 and 0.3 for PF and SF specimens (except the UHP-FRC specimen), respectively, where A_g is the gross cross-sectional area of concrete for each specimen.

While the axial load was kept constant, the specimens were subjected to lateral displacement cycles, as shown on Figure 2.8 and described in Table 2.5. A single-cycle loading protocol (i.e., monotonic cycle) was applied to the first specimen (SP1), whereas all other specimens were subjected to progressively increasing displacement cycles until they exhibited severe damage and strength loss. The loading stopped when one of the following conditions was satisfied: (1) the specimen showed significant strength loss such that the residual strengths were less than or equal to 20% of the peak strengths in both

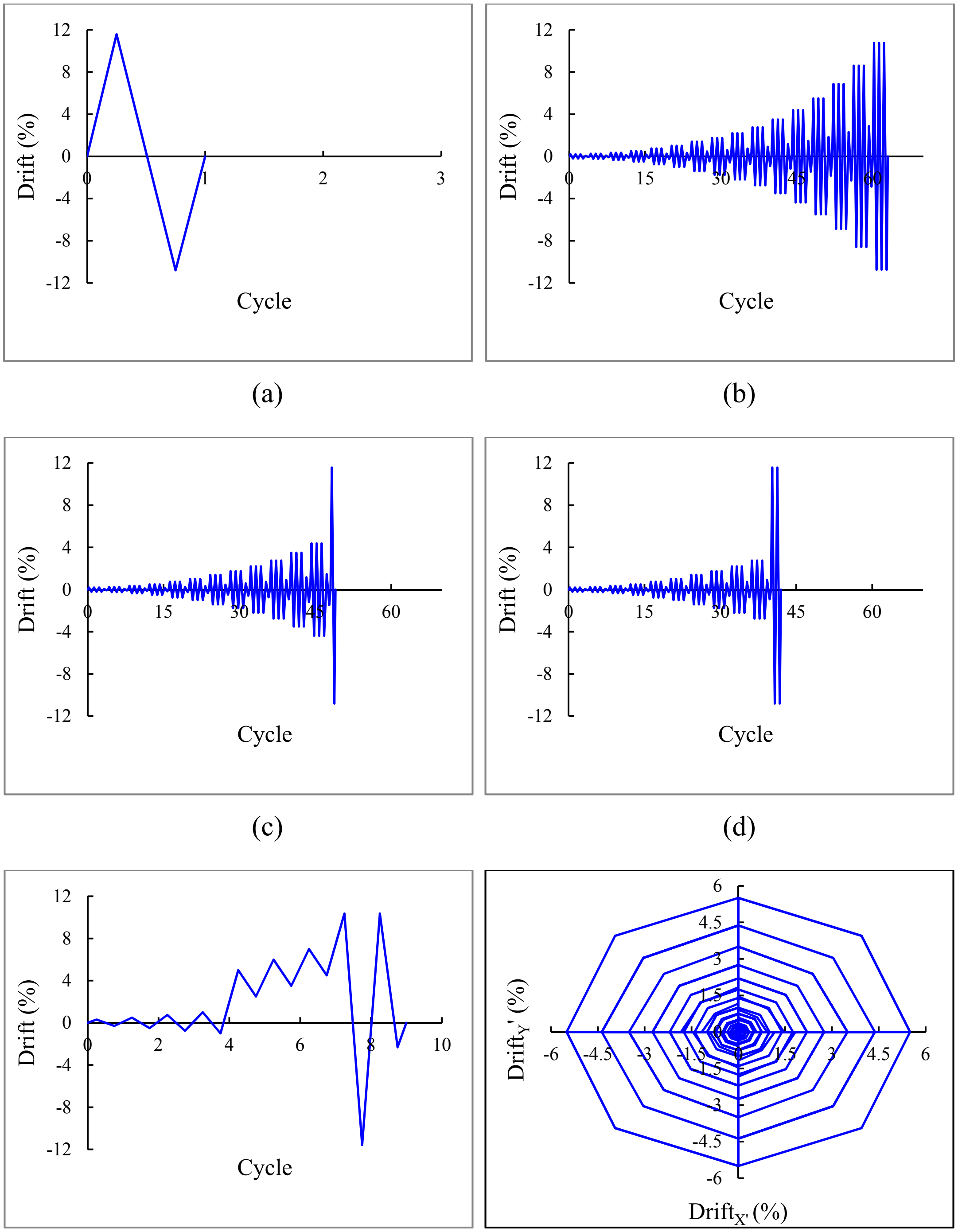

(a) (b)

(c) (d)

(e) (f)

Figure 2.8. Loading Protocols for Specimens: (a) SP1; (b) SP2, SP5, and SP8; (c) SP3; (d) SP4; (e) SP6; (f) SP7

Table 2.5. Applied Loading Protocols

Specimen	*TYP.*	$b \times h$ (in.)	$P/f_c A_g$	Loading Protocol in Figure 2.8	Description of the Loading Protocol
SP1	PF	36×28	0.154	a	Monotonic
SP2	PF	36×28	0.139	b	Symmetric Cyclic (ACI 374)
SP3	PF	36×28	0.141	c	Symmetric Cyclic (ACI 374) Plus Monotonic Push
SP4	PF	36×28	0.140	d	Symmetric Cyclic (ACI 374) Plus Monotonic Push
SP5	SF	28×28	0.285	b	Symmetric Cyclic (ACI 374)
SP6	PF	36×28	0.163	e	Near-Collapse
SP7	PF	36×28	0.154	f	Biaxial
SP8	SF	28×28	0.065	b	Symmetric Cyclic (ACI 374)

directions exhibited during the test; and (2) the hydraulic actuators reached their maximum stroke or rotational capacity.

Except for SP1 and SP6, all other loading protocols were designed in accordance with ACI 374-05 (ACI Committee 374, 2005) guidelines. These protocols comprised three full-reversed displacement cycles at each drift level followed by a small cycle at 1/3 of the preceding drift level. This loading pattern was applied to SP2, SP5, and SP8 with progressively increasing drift cycles until one of the stopping criteria was satisfied; SP3 and SP4 experienced a monotonic push after a certain number of cycles. Displacement cycles were applied along the primary axis of the specimens (Y′ axis in Figure 2.2(b)), except for SP7, which was subjected to a biaxial loading protocol as shown on Figure 2.8(f).

SP6 was subjected to a near-collapse loading protocol that was developed using results from time-history analysis of a series of low- to high-rise buildings subjected to a set of far-field earthquake records. The near-collapse loading protocol consisted of symmetric cycles followed by large unsymmetric displacement cycles under which typical columns in the time history analysis showed significant yielding and strength loss.

2.8. TEST OBSERVATIONS

Figure 2.9 shows specimen damage initiated after application of early cycles when flexural cracks were observed on the SE and NW faces close to the column base. Also, shear-flexure cracks were observed on the SW and NE faces and distributed through the lower portion of the specimens. Cracking and spalling of the cover concrete was followed by yielding of the longitudinal bars. However, the specimens reached their peak strengths at larger displacement levels because of the resistance mobilized by the confining pressure of the transverse hoops as well as strain hardening of the longitudinal bars. Cracking and crushing of the concrete along the column perimeters and, more importantly, buckling and fracture of the longitudinal bars resulted in the loss of flexural resistance. In some specimens, spalling of the cover concrete and lateral pressure of the longitudinal bars caused some hoops to open. Buckled bars fractured at following large drift ratios, which resulted in sudden decreases in lateral load capacity. At the end of the tests, severe damage to the perimeter concrete and fracture of the longitudinal bars in the extreme faces were observed.

Figure 2.10 shows applied lateral loads for SP1, SP2, and SP3 plotted against their lateral drifts (measured at the idealized inflection point) and lateral displacements. The specimens subjected to these loading protocols [(a), (b), and (c)] were selected as representative of all loading protocols because they included a single cycle, a series of gradually increasing cycle groups, and a series of gradually increasing cycle groups followed by a collapse-level drift cycle. The loading protocols addressed one of the primary goals of this project that was testing of RC columns under large drift ratios and capturing their post-peak performance at the near-collapse state. In the first specimen (SP1), the loading was terminated at an approximate 12% drift ratio when the actuators reached their rotational capacity. However, the progression of damage and strength loss in SP2 and SP3 occurred at a greater rate such that the capacity of these specimens deteriorated to 20% or less of their peak strength at smaller drift ratios than that of SP1.

Strains in longitudinal bars, transverse hoops, and the concrete core were recorded during each test using embedded strain gages that are shown in Figure 2.6. On longitudinal bars, the strain gages were installed at closely spaced points along the lower portion of the column and in the footing block, by which the onset of yielding, strain hardening, and fracture of longitudinal bars could be identified during application of the loading protocols. As shown in Figure 2.11(a), at a 2.15% drift ratio for specimen SP2, yielding occurred over a large portion of one of the longitudinal bars. Nominal yielding in Figure 2.11 can

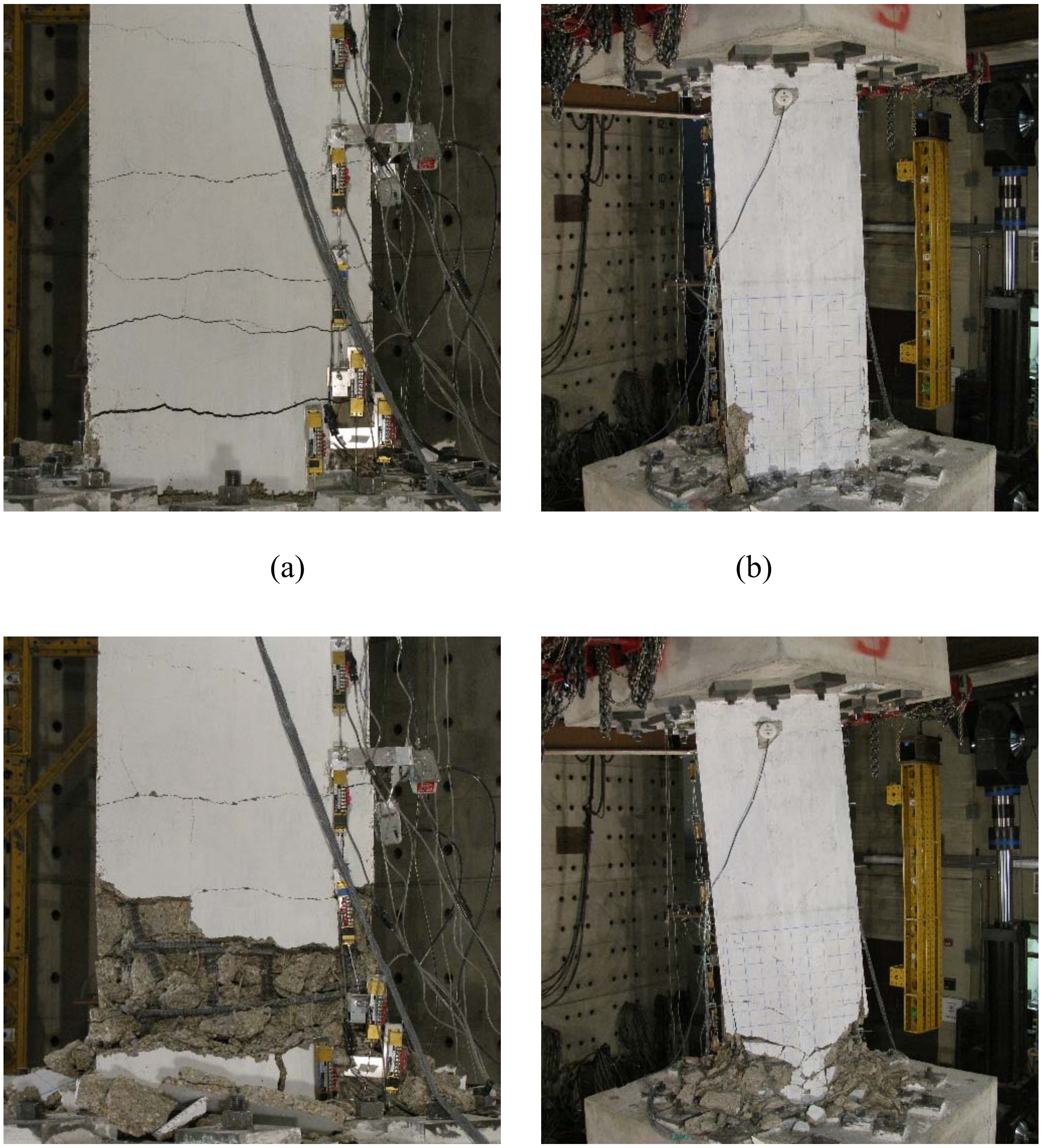

(a) (b)

(c) (d)

Figure 2.9. Progression of Damage on SP2: (a) SE Face at 2.2% Drift Ratio; (b) SW Face at 2.2% Drift Ratio; (c) SE Face at the End of the Test and (d) SW Face at the End of the Test

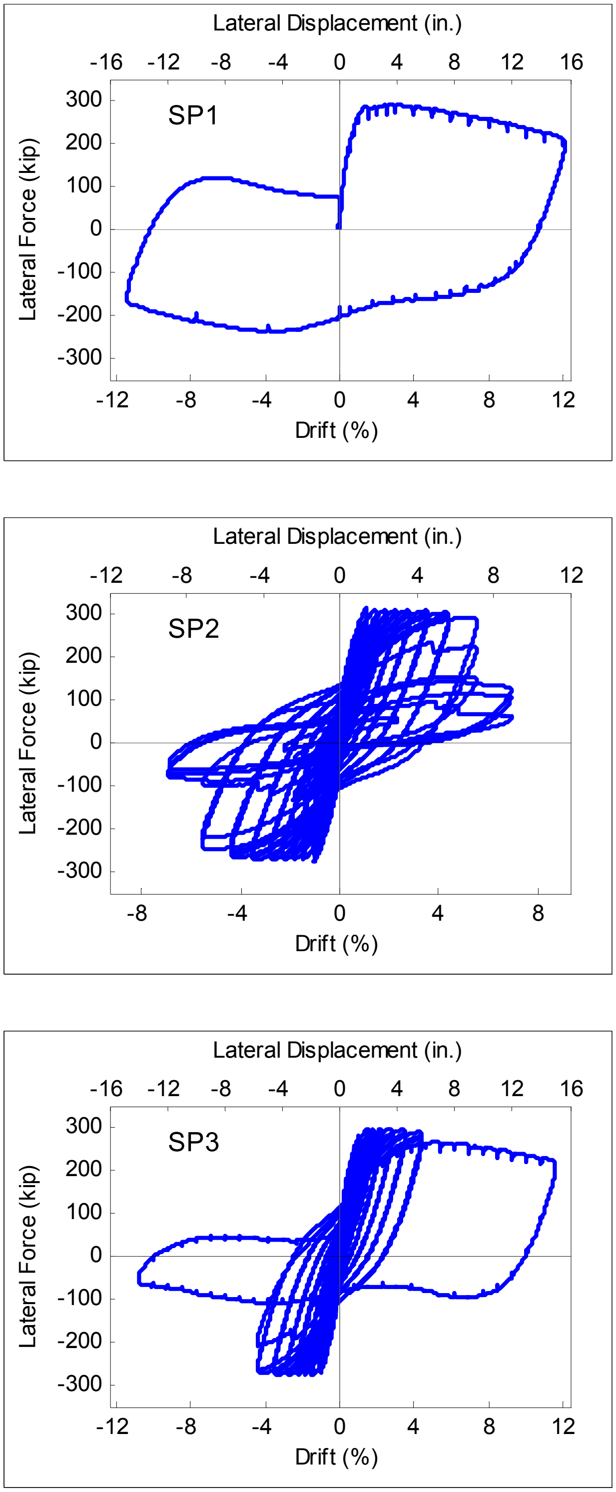

Figure 2.10. Applied Load vs. Crosshead Displacement and Drift Ratio

be recognized as a strain equal to 0.0025 in./in., as indicated by the dashed line. Also, at the same drift level transverse hoops started to yield at a location approximately 12 in. above the column base, as shown in Figure 2.11(b). On transverse hoops, strain gages were installed along the column height and at different locations in the cross section (Figure 2.6).

Besides longitudinal bars and transverse hoops, strains at different locations in the concrete core were measured using vertical and horizontal strain gages. Figures 2.12(a) and 2.12(b) show strain profiles measured along the height of SP2 and at a 2.15% drift ratio. In these figures, CL1G corresponds to the vertical strain gage located at the midpoint of the specimen's SE face; CTRH4G measures the horizontal strains (as shown on Figure 2.6). Horizontal strains measured by CRTH4G fell beyond the cracking strains for the concrete, which was confirmed by the formation of many horizontal flexural cracks as observed in Figure 2.9.

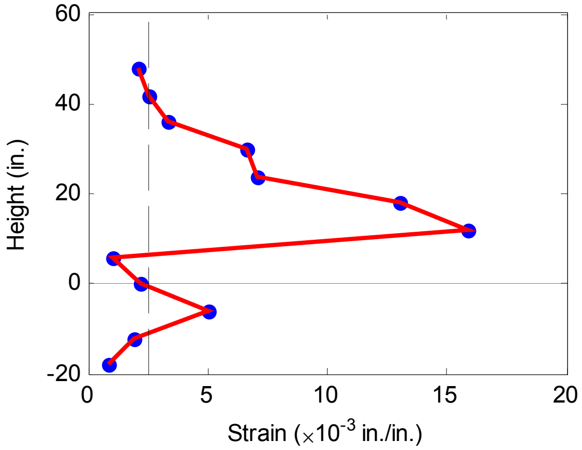

(a)

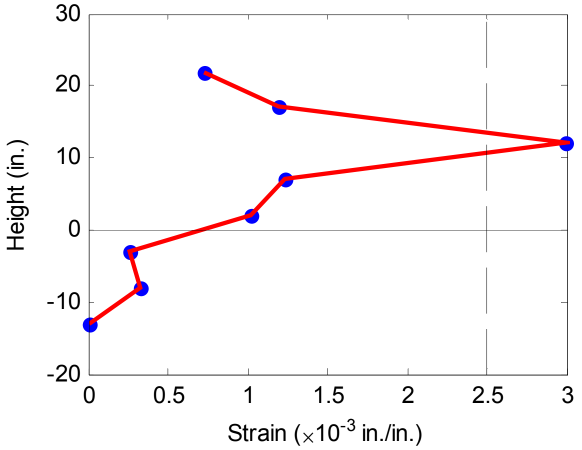

(b)

Figure 2.11. Reinforcement Strain Profiles along Column Height at 2.15% Drift Ratio for Specimen SP2: (a) Longitudinal Bar (SL1G); (b) Transverse Hoops (STR3G)

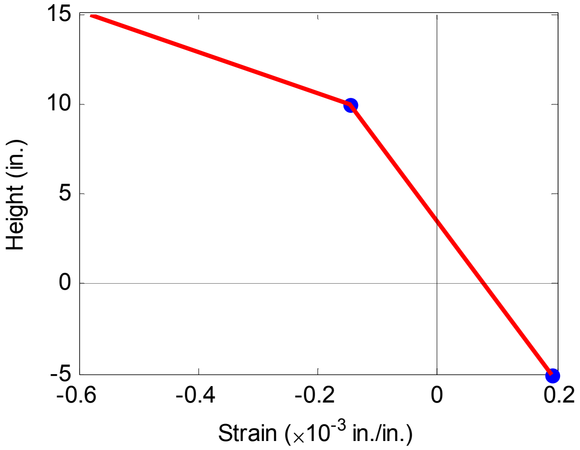

(a)

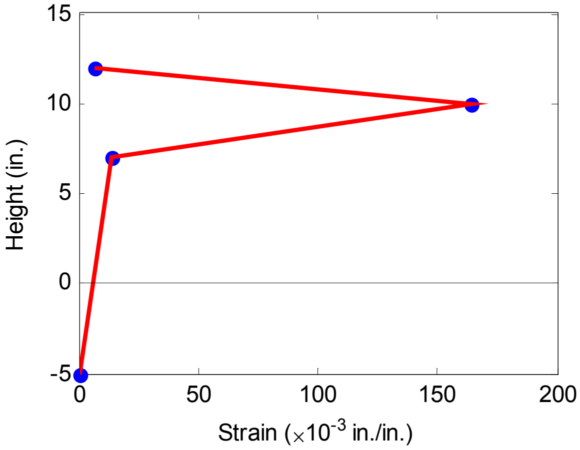

(b)

Figure 2.12. Concrete Core Strain Profiles along Column Height at 2.15% Drift Ratio for Specimen SP2: (a) Vertical Strain Gages (CL1G); (b) Horizontal Strain Gages (CTRH4G)

Along with strain gages, vertical LVDTs were installed on the specimens' SE and NW faces (Figure 2.5) to estimate flexural curvature along the column height. Such estimation was carried out for the lower portion of specimen SP2, as shown in Figure 2.13, which illustrates base moment for specimen SP2 against curvature measured 6 in. above the column base. Curvature at this point was calculated using measurements for the vertical LVDTs on the column's SE and NW faces. Also, the base moment included the first-order moment caused by application of the lateral load over the column height as well as the second-order moment resulting from the P-delta effect. The LVDT cores were connected to aluminum plates located on the footing block. These plates were anchored at a distance from the column so that they would not get loose after cracking of the concrete at the column base.

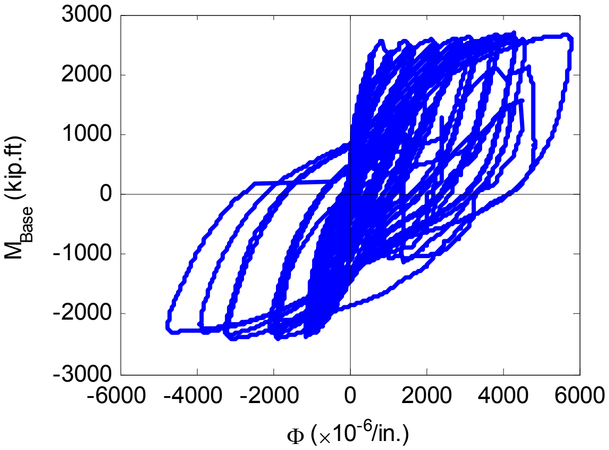

Figure 2.13. Moment vs. Curvature Relation for SP2 Measured 6 in. from the Column Base.

2.9. FUTURE USE OF THE DATA SET

Recorded data from eight full-scale column tests are available at NEEShub (NEES 2009) for researchers and structural engineers to investigate the observed behavior of the column specimens during the tests. These data include measurements from the MAST lab 6-DOF control system and the instrumentation (LVDTs, string pots, tiltmeters, and strain gages). Additionally, the high- and extra-high-resolution still images and high-resolution videos provide a visual record of damage for each face of the column specimens during testing. The data set will enhance understanding of the behavior of RC and UHP-FRC columns subjected to near-collapse loading protocols and can be used to calibrate finite-element models intended to simulate their behavior. Also, it can be utilized to improve collapse-predictive component models for performance-based design, to evaluate ACI code methodology for estimation of shear and moment capacity, to quantify the evolution of energy dissipation and secant (or tangent) stiffness during cyclic loading, and to assess the effects of loading protocols on damage state.

First, the test data from this experimental program can enhance knowledge of the behavior of RC and UHP-FRC columns subjected to large seismic events, and they can be used to assess and improve finite-element modeling. Previous experiments on RC columns were performed either on small- or medium-scale specimens or under small drift ratios. Accordingly, finite-element models were typically calibrated with test results that did not capture the complete range of column post-peak behavior. The loading protocols in this experimental program were extended to large drift ratios (~12%) until the specimens exhibited significant strength loss (i.e., 80% or more of their maximum strength in each loading direction) and stiffness deterioration. The data from this research program will enable finite element model calibration and validation against a wide range of structural performance. Developed models can then be utilized to assess the seismic performance of structures under various axial load ratios, cross-sectional dimensions, and loading protocols. Also, the tests performed on columns constructed with UHP-FRC material will enhance knowledge of the seismic performance and damage tolerance capabilities of columns constructed with this innovative material, and they will provide a tool to improve structural models that capture their behavior.

An important application of the recorded test data is the assessment and improvement of existing collapse-predictive component models in performance-based seismic design. A set of comprehensive test data is required for the development of representative nonlinear models and implementation of a reliable analysis for performance-based design. Improved component models represent an important step in predicting the collapse safety of existing buildings that are designed in accordance with modern codes as well as in designing reliable structures. They have been recognized as a requirement for the advancement of performance-based seismic engineering procedures (Applied Technology Council (ATC), 2009b). The tests conducted in this research were designed considering the critical need for collapse prediction in performance-based design procedures.

The proposed methodology in the ACI code for estimation of column shear and moment capacity can be evaluated using flexural moments, axial loads, and internal strains measured during each test. Nominal shear and moment capacities calculated following the ACI code approach can be compared to the specimen's actual strength exhibited during each test to assess the validity of the current design methodology for RC columns, including the capacity design procedures for evaluating seismic demands in RC moment frames. Also, the effects of the applied axial load level and the lateral loading protocol on shear and moment capacity can be estimated.

Finally, recorded test data during each test provide a measure to quantify the evolution of damage as represented by energy dissipation (or absorption) and the change in secant (or tangent) stiffness under cyclic loading protocols. Energy dissipation and stiffness change are both affected by characteristics of the loading protocol (i.e., target displacement, axial load level, and number of cycles). These characteristics can affect the extent of specimen damage produced. A larger target displacement, a higher axial load level, and a greater number of deformation cycles will typically result in more damage to the concrete as well as yielding, buckling, or ultimately fracturing of the reinforcing bars. The progression of damage in a RC column, on the other hand, is accompanied by energy dissipation and a reduction in secant (or tangent) stiffness. Therefore, recorded test data can be used to calculate energy dissipation and secant (tangent) stiffness at different test stages to estimate the extent of damage and identify the parameters that accelerate it.

2.10. CONCLUSIONS

A set of eight full-scale RC and UHP-FRC column tests was conducted at the MAST laboratory at the University of Minnesota to address the shortcomings in available test data for rectangular columns in high-rise buildings. The tests aimed to enhance understanding of the behavior of RC columns representative of those typically used in the ground floor of tall moment-resisting frame buildings at a near-collapse state, and to utilize this enhanced understanding to develop improved collapse-predictive component models for performance-based design. The data set can be accessed through a DOI and includes details of specimens, material properties, sensor and instrumentation layouts and their recorded data, and high- and extra-high-resolution images and high-resolution videos recorded during each test. It provides an opportunity for researchers and engineers in the field to enhance their knowledge of the seismic performance of RC columns under severe loading conditions. The recorded test data can be utilized to assess and improve finite element modeling tools as well as existing collapse simulation models to more accurately capture post-peak column behavior. Additionally, the data set can be employed to evaluate the current ACI code for estimating nominal RC column moment and shear capacity and for assessing the evolution of energy dissipation and stiffness deterioration under various loading protocols.

CHAPTER 3

INFLUENCE OF CROSS-SECTIONAL SIZE ON SEISMIC PERFORMANCE OF RC COLUMNS[2]

3.1. SUMMARY

Current ACI code provisions ACI 318-14 (ACI Committee 318, 2014) for the design of reinforced concrete (RC) columns are based on previous experiments on column specimens that featured smaller cross-sectional dimensions compared to those currently used in mid- or high-rise buildings. A study on a database of RC columns including those recently tested at the MAST Laboratory of the University of Minnesota as part of this research, and ACI 369 Rectangular Column Database (Ghannoum et al., 2012) suggests that flexural moment capacity, drift capacity, and displacement ductility of columns are not generally affected by column dimension (i.e. cross-sectional depth). However, the bar buckling can start earlier in larger columns. Additionally, observations from the MAST tests reveals a bar buckling mode that is seldom observed in tests on smaller columns, in

---

[2] Under review by ACI Structural Journal.

which the bars buckle parallel to the face of the column. A study that is presented herein suggests that larger columns are more prone to this in-plane mode of bar buckling.

Keywords: RC column, cross-sectional size, bar buckling

3.2. INTRODUCTION

Many experiments have been carried out on rectangular RC columns. Properties of more than 300 of such tests are collected in the ACI 369 Rectangular Column Database (2012) as well as in the PEER structural performance database (Berry et al., 2004). The primary goal of most of these tests was to investigate the behavior of RC columns subjected to gravity and seismic loadings and to develop and improve design code provisions for building columns. However, many of the tests were conducted on columns with smaller dimensions than those currently used in mid- or high-rise buildings mainly due to limitations of the testing facilities. The average cross-sectional depth of the rectangular RC columns in the more recent database (i.e., ACI 369 Rectangular Column Database (2012)) is 12.5 in. (318 mm) with the lower 5% and upper 95% bounds of 6.3 in. (160 mm) and 21.65 in. (550 mm), respectively. The smallest and largest columns in these databases that failed either in flexure or flexure-shear mode featured a cross-sectional depth of 3.15 in. (80 mm) (Zhou, Higashi, Jiang, & Shimizu, 1985) and 27.56 in. (700 mm) (Yarandi, 2007). While these tests provide a valuable dataset for RC columns, a careful study is required to assess the validity and applicability of their results to estimate seismic performance of actual columns with larger dimensions.

A clear understanding of the seismic performance of RC columns is crucial in designing earthquake resistant structures. In performance-based design, columns are designed to sustain a certain level of damage under the effect of applied loads, but to resist collapse. The state of damage in RC columns is usually linked to moment capacity, drift capacity, drift ratio at yield, and the drift at the onset of buckling.

RC columns are typically designed with sufficient flexural capacity to resist external loads. The flexural moment capacity of RC columns can be affected by many parameters including axial load magnitude, concrete compressive strength, and amount of transverse reinforcement. A well-designed RC column should be able to resist flexural moments due to lateral loading and associated P-Delta effects, and experience large deformations before failure. Therefore, the maximum flexural moment of a RC column during testing can be used to evaluate its seismic performance as well as the accuracy of the ACI approach to estimate flexural moment capacity.

Additionally, accurate estimation of the effective stiffness of RC columns is important in design because it affects load carrying capacity, deformation demands, and dynamic response characteristics. Most existing procedures specify the effective stiffness as a fraction of the gross stiffness depending on the axial load ratio (ACI Committee 318, 2014; American Society of Civil Engineers (ASCE), 2000, 2007; Paulay & Priestley, 1992). Further research (Elwood & Eberhard, 2009) showed that the effective stiffness of concrete columns is also strongly proportional to aspect ratio (the ratio of shear span to column depth in the direction of loading, *L/h*).

Moreover, drift capacity and displacement ductility are important parameters in performance-based design as they indicate the expected lateral deformation when reaching a certain level of strength loss, typically 20% of the peak lateral load capacity. The effect of column aspect ratios on the drift capacity depends on the level of axial load ratio. Increasing aspect ratio (*L/h*) will result in an increase in the drift capacity provided that the axial load ratio is small. In columns with large axial load ratios, on the other hand, increasing *L/h* can pronounce the P-Delta effect and result in a lower drift capacity (Bae & Bayrak, 2008).

Last but not least, seismic performance of RC columns can be significantly affected by reinforcing bar buckling as it is often followed by significant strength degradation and stiffness deterioration that lead to extensive and costly damage. Reinforcing bar buckling in RC columns can initiate right after spalling of the cover concrete or yielding of transverse hoops (Bae & Bayrak, 2008) and well before global collapse of the specimens. Early bar buckling can drastically affect ductility of RC columns and limit their drift capacity. Therefore, understanding the drift ratio at which the bar buckling initiates, is significantly important for practicing engineers. To achieve this understanding, analytical and experimental studies have been carried out to investigate the buckling of longitudinal bars. Early investigations employed Euler buckling theory to explain the observed buckling behavior of bars (Bresler & Gilbert, 1961; Scribner, 1986; Papia, Russo, & Zingone, 1988). Other researchers conducted analytical (Gomes & Appleton, 1997; Dhakal & Maekawa, 2002) and experimental studies on isolated bars (Mander, Priestley, & Park, 1984; Monti & Nuti, 1992; Rodriguez, Botero, & Villa, 1999; Bayrak & Sheikh, 2001) to investigate the constitutive relationship of steel reinforcing bars including the effect of buckling, and to study the parameters that affect bar buckling. However, experimental investigations on RC columns with specific focus on bar buckling are limited (Suda, Murayama, Ichinomiya, & Shimbo, 1996; Moyer & Kowalsky, 2003; Brown, Lehman, & Stanton, 2008). These experimental investigations have sought to define drift or displacement demands corresponding to the onset of bar buckling as a critical damage state in seismic performance-based design.

In this study, the selected database of RC columns is used to study the influence of cross-sectional size on seismic performance characteristics of columns, namely the moment capacity, drift capacity, ductility, and drift at the onset of buckling. For each seismic characteristic, the calculation scheme used with the information available in the database, as well as the key controlling parameters are discussed and employed to categorize the columns. The influence of cross-sectional size is then studied for columns in each category.

3.3. RESEARCH SIGNIFICANCE

RC columns can incorporate cross-sectional dimensions significantly larger than those tested previously and which were utilized to verify ACI code design provisions. A series of tests on rectangular RC columns with larger cross-sectional dimensions was carried out as part of this research to fill the gap in the existing database of RC columns. Results from these tests were employed along with an available database of RC columns (Ghannoum et al., 2012) to investigate the effects of cross-sectional size on seismic performance of RC columns including moment capacity, effective stiffness, drift capacity, displacement ductility, and bar buckling.

3.4. EXPERIMENTAL INVESTIGATION AND DATA SELECTION

Seven full-scale RC column tests, representative of modern mid- and high-rise RC moment frame buildings, were conducted at the Multi-Axial Subassemblage Testing (MAST) Laboratory of the University of Minnesota. These columns featured cross-sectional dimensions (36×28 in. and 28×28 in.) (914×711 mm. and 711×711 mm.) larger than most of the previous tests on RC columns subjected to cyclic loading protocols (Berry et al., 2004; Ghannoum et al., 2012). Each specimen was constructed horizontally along with a 84×84×30 in. (2134×2134×762 mm.) footing block and a 75×75×23 in. (1905×1905×584 mm.) loading block (Figure 3.1) and was placed on top of a spacer block under the MAST loading crosshead (Figure 3.2). Each test was started with application a constant axial load along Z′ axis followed by a lateral displacement loading protocol along X′ axis. Additionally, to focus this study on the effects of loading protocols and to eliminate changes in the response of columns due to dislocation of the inflection point a flexural moment was applied on top of the specimen to maintain the inflection point at 96 in. (2438 mm.) above the column base corresponding to one half of the height of the columns in the ground floor of the prototype building. However, during an actual earthquake, the inflection point typically shifts upward along the length of RC columns and hence a lower lateral load as compared to the case with fixed inflection point would be required to generate the plastic moment at their base. Therefore, RC columns in practice may exhibit lower drift capacity and drift ratio at the onset of buckling as those that were recorded during tests at the MAST Lab. Information regarding cross-sectional dimensions as well as concrete compressive strength (f'_c), axial load ratio (P/f'_cA_g), and aspect ratio (L/h) of these columns is presented in Table 3.1. The table also shows distinct lateral loading protocols applied to the specimens during each test.

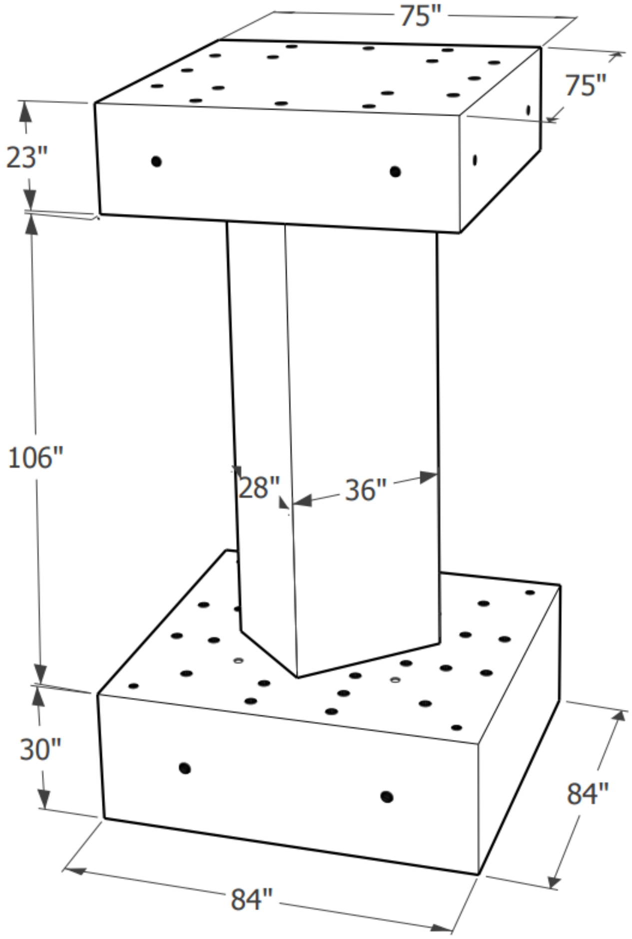

Figure 3.1. Overview of the Test Specimens

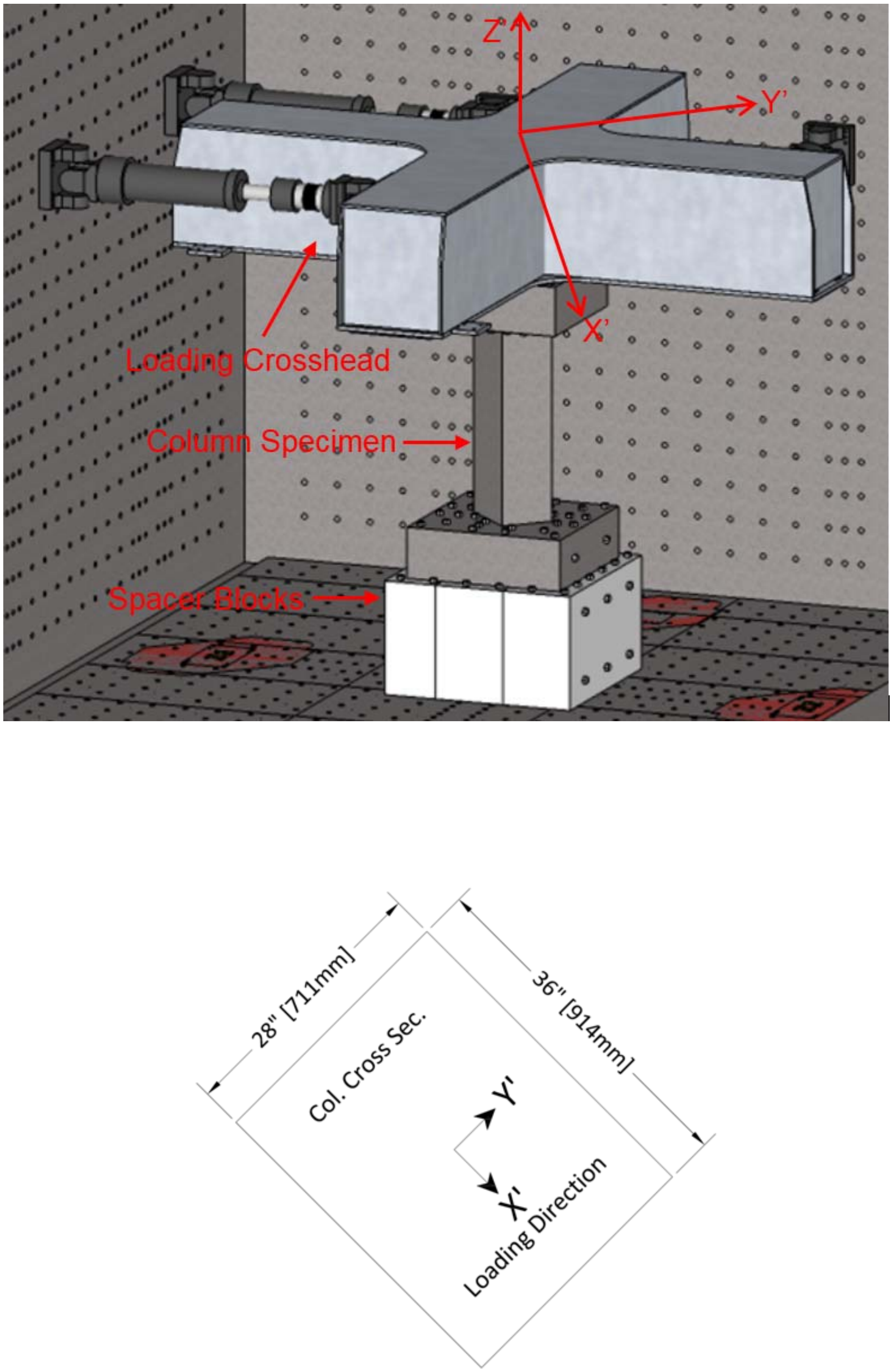

Figure 3.2. Overview of the Test Setup at the MAST Lab and Loading Direction

Table 3.1. Characteristics of the MAST Tests

Specimen	Loading Protocol	$b \times h$ in. ×in. (mm× mm)	f'_c, ksi (MPa)	L/h	P/f'_cA_g	M_{test}/M_n	δ_{80} (%)	K_{eff}/K_g	μ_Δ
SP1	Monotonic	36×28 (914×711)	4.86 (33.51)	2.67	0.15	1.30	10.74	0.19	10.15
SP2	Symmetric Cyclic (ACI 374-05 (2005))	36×28 (914×711)	5.40 (37.23)	2.67	0.14	1.26	7.13	0.26	5.31
SP3	Symmetric Cyclic Plus Monotonic Push	36×28 (914×711)	5.30 (36.54)	2.67	0.14	1.22	7.83	0.19	7.35
SP4	Symmetric Cyclic Plus Monotonic Push	36×28 (914×711)	5.37 (37.02)	2.67	0.14	1.35	10.19	0.21	8.78
SP5	Symmetric Cyclic (ACI 374-05 (2005))	28×28 (711×711)	5.27 (36.34)	3.43	0.28	1.33	4.09	0.38	4.53
SP6	Near-Collapse	36×28 (914×711)	4.61 (31.78)	2.67	0.16	1.28	12.47	0.17	9.60
SP7	Biaxial	36×28 (914×711)	4.90 (33.78)	2.67	0.15	1.19	5.09	0.14	4.79

A single cycle loading protocol was applied to the first specimen (SP1) to capture the monotonic force-displacement envelope of the test specimens in a single cycle. The second specimen (SP2) was subjected to progressively increasing displacement reversals which were defined according to the guidelines in the ACI 374-05 (ACI Committee 374, 2005). The applied lateral loading protocols were continued until the specimens lost most of their load carrying capacity (more than 80% of peak lateral load capacity). The lateral loading on SP3 and SP4 started with displacement cycles like those used in SP2. However, these two specimens were subjected to a final monotonic displacement segment after a specified number of cycles. The applied loading protocol and hysteretic force-displacement (or drift ratio) of specimen SP4 is represented in Figure 3.3**.** The last two specimens (i.e., SP6 and SP7) were subjected to a near-collapse cyclic loading protocol which was designed as part of this research, and a biaxial cyclic loading protocol, respectively. Further details regarding the applied loading protocols can be found elsewhere (Nojavan et al., 2014, 2015) and are not shown here for brevity. Results from these tests were employed along with ACI 369 Rectangular column database (Ghannoum et al., 2012) to investigate the influence of cross-sectional depth on the seismic performance of columns. The column dataset was screened to include only columns with concrete compressive strength between 2.5 ksi (17.24 MPa) and 10 ksi (68.94 MPa) in order to focus the study on structural columns constructed with normal and moderately high strength concrete. Additionally, it is assumed that columns in a typical building design based on standard code practice will not suffer shear failure and reach flexural capacity when subjected to extreme loadings. Thus, column specimens failing in shear were excluded from the dataset. A complete list of the test specimens utilized for the purpose of this study is not shown here for brevity. Instead, the range and statistics of important parameters (i.e. minimum, maximum, mean, and coefficient of variation (CV) of concrete compressive stress (f'_c), reinforcing yield stress (f_y), cross-sectional depth (h), and reinforcing bar diameter (d_b)) for the selected specimens are presented in Table 3.2.

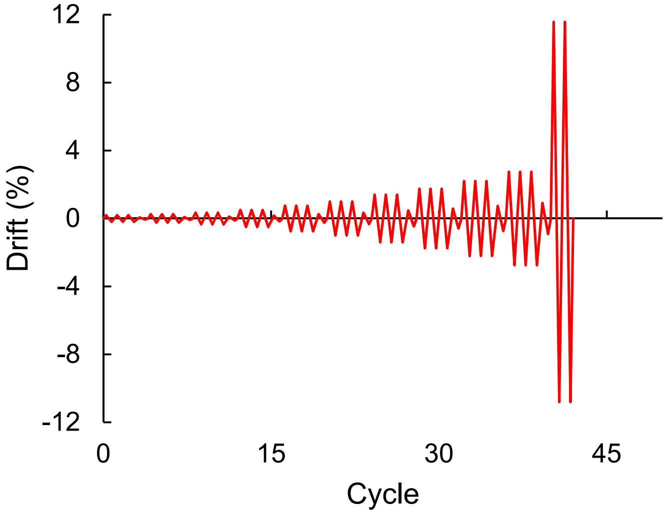

(a)

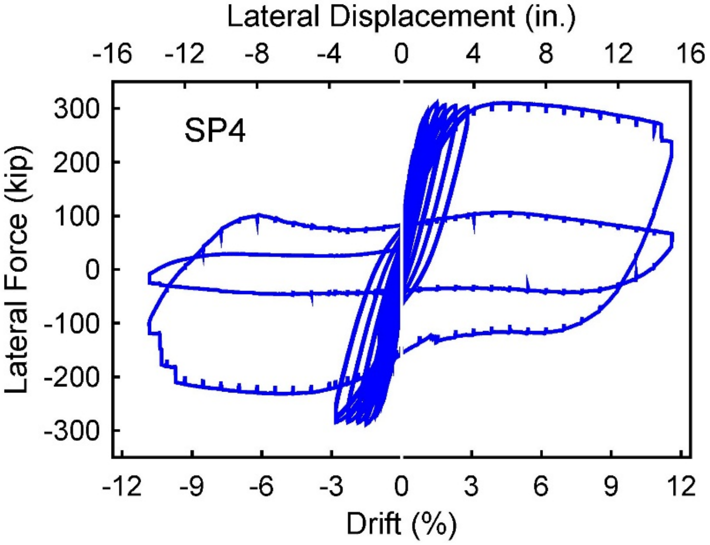

(b)

Figure 3.3. Behavior of Specimen SP4 under the Applied Loading Protocol: (a) Loading Protocol, (b) Variation of Lateral Force with Drift Ratio and Top Displacement

Table 3.2. Properties of Rectangular Columns in the ACI 369 Database

Parameter	Min.	Max.	Mean	COV
f'_c, *ksi (MPa)*	2.55 (17.6)	9.83 (67.8)	4.58 (31.6)	0.276
f_y, *ksi (MPa)*	46.8 (322.9)	85.1 (586.9)	62.1 (428.2)	0.154
h, in. (mm)	3.15 (80)	27.6 (700)	13.6 (345)	0.351
d_b, in. (mm)	0.24 (6)	1.25 (32)	0.71 (18)	0.281

3.5. FLEXURAL MOMENT CAPACITY

3.5.1. Calculation

The normalized flexural moment capacity of columns is defined here as the ratio of the maximum measured flexural moment during the test (M_{test}), including the P-Delta contribution (i.e. moment due to axial load and column lateral deflection), to its nominal moment capacity (M_n) calculated according to the provisions in ACI 318-14 (2014). To compute the nominal flexural moment capacity (M_n) for each column in the database, the nominal axial load-flexural moment (P-M) interaction diagram was computed using strain compatibility, and assuming an ultimate concrete compressive strain of 0.003 and an elastic-perfectly plastic reinforcing steel material model. Measured concrete and steel material properties were used. The location of the neutral axis was computed based on a linear strain distribution and was used to determine the depth of the compression region. For each level of strain, the compressive force provided by concrete was calculated based on an equivalent rectangular concrete stress block, following provisions in the ACI 318-14 (2014), and neglecting the confinement effect. The compressive force resultant in the concrete was considered along with the forces provided by reinforcing steel bars to compute the net axial force and the moment about the geometric centroid of the section. The moment associated with the applied axial load on the *P-M* interaction diagram was then taken as the flexural moment capacity of the column specimen (M_n).

3.5.2. Influence of Column Section Depth h

The normalized moment capacity (M_{test} / M_n) for all the columns in the database is plotted against their cross-sectional depths (Figure 3.4). It is noticed that columns failing in flexure exhibit a normalized moment capacity of at least one while this ratio is generally smaller for the columns that failed in shear (not shown for brevity). In other words, all of the column specimens developed their nominal moment capacity, computed according to ACI 318-14 (2014) regardless of their cross-sectional depth, unless they failed in shear. This observation confirms the ACI 318-14 (2014) flexural design provisions for RC columns to be appropriately conservative. The data in Figure 3.4 also indicate that the normalized moment capacity is not generally dependent on the cross-sectional depth of columns (i.e. the linear least squares trend line including the tests conducted at the MAST lab is nearly flat) for flexure dominated columns and the MAST Lab tests do not alter this trend.

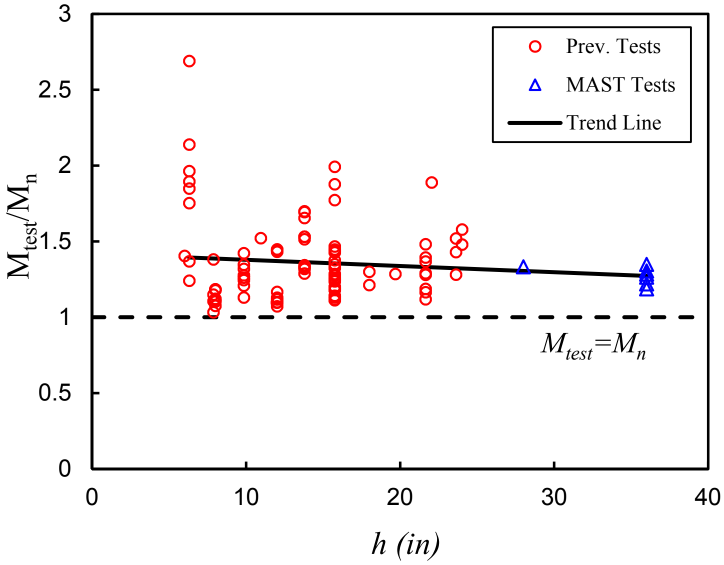

Figure 3.4. Normalized Moment Capacity vs. Cross-Sectional Depth for Columns Failing in Flexure

3.6. EFFECTIVE STIFFNESS

3.6.1. Calculation

A simple approach was employed to compute the effective stiffness (K_{eff}) of the columns (Figure 3.5). A secant passing through a point on the Lateral Force-Displacement (F-Δ) cyclic envelope corresponding to 70% of the maximum applied lateral load on the specimen ($0.7F_{max}$) is extended to intersect with the horizontal line at F_{max} as shown in Figure 3.5. The yield displacement is defined as intercept of a vertical line from the intersection point on the horizontal axis. This approach is similar to that used by Elwood and Eberhard (2009) to estimate $EI_{eff\ calc}$ except that they used the lateral load

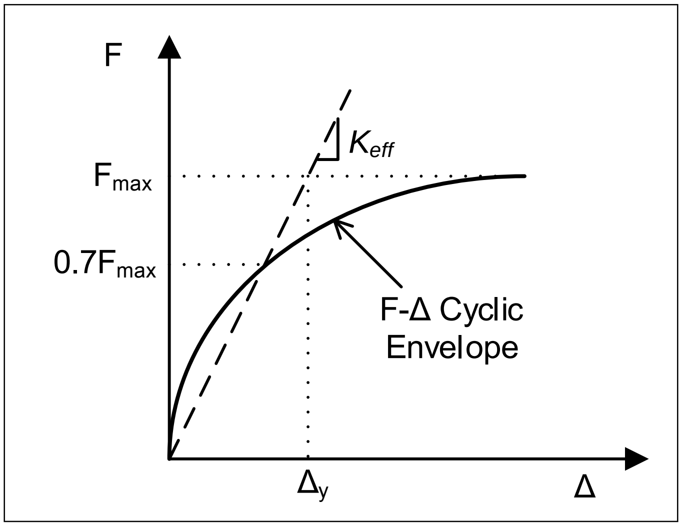

Figure 3.5. Definition of the Effective Stiffness

corresponding to a specified concrete compressive strain and yielding of reinforcing steel instead of F_{max} and $0.7F_{max}$. Reported values for F_{max} and drift ratio at yielding (δ_y) by Ghannoum et al. (2012) and Sivaramakrishnan (2010) that were calculated according to the aforementioned approach, were utilized to compute the effective stiffness of the columns in the dataset. Considering that concrete cracking typically happens before yielding of the longitudinal bars in RC columns, it would appear to be more realistic for the effective stiffness to be normalized by the stiffness computed based on cracked and transformed section properties. Mehanny et al. (2001) applied this idea to normalize the effective stiffness, but their proposed approach was shown to overestimate the normalized stiffness of both rectangular and circular columns (Elwood & Eberhard, 2009). Consequently, the gross section stiffness (K_g) was used to normalize the calculated effective stiffness, as was done by Elwood and Eberhard (2009).

3.6.2. Influence of Axial Loading and Aspect Ratio

The normalized effective stiffness of RC columns (K_{eff} / K_g) which is equal to EI_{eff} / EI_g can vary significantly depending on the applied axial load level and aspect ratio (Elwood & Eberhard, 2009). To investigate the effect of cross-sectional depth on effective stiffness, the columns in the database were subdivided into distinct categories depending on their axial load ratio (P/f'_cA_g) and aspect ratio (L/h) in order to separate the effects of these two parameters and identify the influence of column depth more easily. Four categories of axial load ratio ($P/f'_cA_g<0.2$, $0.2\leq P/f'_cA_g<0.3$, $0.3\leq P/f'_cA_g<0.4$, and $0.4\leq P/f'_cA_g$) and four categories of aspect ratio ($1\leq L/h<2$, $2\leq L/h<3$, $3\leq L/h<4$, $4\leq L/h$) were considered.

For the columns in the database, the normalized stiffness ratio (K_{eff} /K_g) was observed to be strongly dependent on the axial load and aspect ratios as illustrated in Figure 3.6. The trend line for each category was obtained using a linear least squares fit. The trend line in Figure 3.6(a) is calculated using all of the data shown, which includes the corresponding previous test data (i.e. test specimens in the ACI 369 database (Ghannoum et al., 2012) as well as most of the tests recently conducted at the MAST lab. The trend lines for the individual aspect ratio categories (Figure 3.6(b)) indicate that for columns with aspect ratios greater than 2, normalized effective stiffness generally increases with axial load ratio, and that the rate of increase further increases with increasing aspect ratio (L/h).

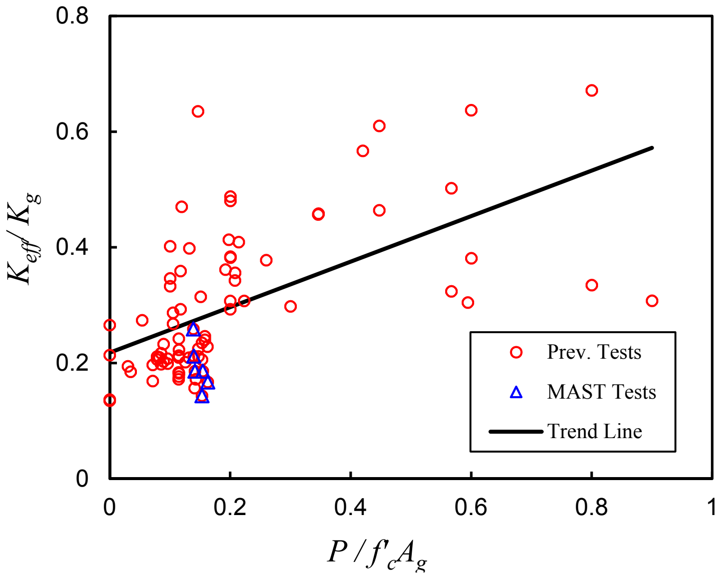

(a) $2 \leq L/h < 3$

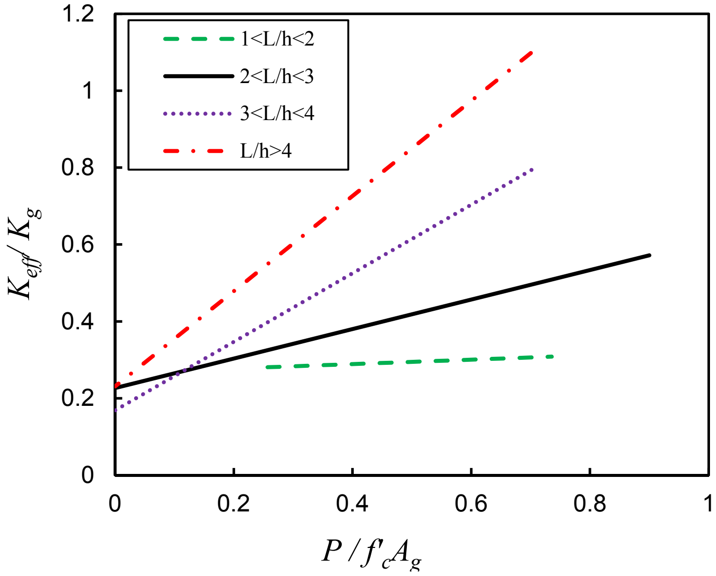

(b) Various *L/h*

Figure 3.6. Normalized Effective Stiffness vs. Axial Load Ratio

3.6.3. Influence of Column Section Depth h

The normalized effective stiffness is shown relative to column cross-sectional depth in Figure 3.7, and it suggests that normalized effective stiffness is not generally affected by column size. Given the large spread of data in Figure 3.7, plots were created for each column category depending on axial load and aspect ratios. The plots for two categories, that contained MAST test data, are illustrated in Figure 3.8. It is observed that including the MAST test results does not significantly change the observed trend. Among the MAST test specimens, SP2 which was subjected to a loading protocol that resembles that used for the rest of the columns in the database, exhibits a normalized stiffness that is pretty close to the trend line. These plots confirm the lack of dependence between normalized effective stiffness and the cross-sectional depth. Slight increasing or decreasing

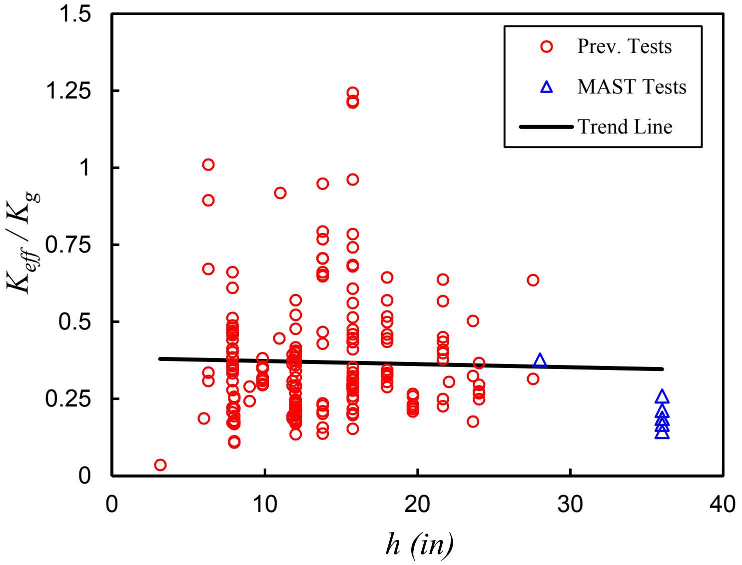

Figure 3.7. Normalized Effective Stiffness vs. Cross-Sectional Depth

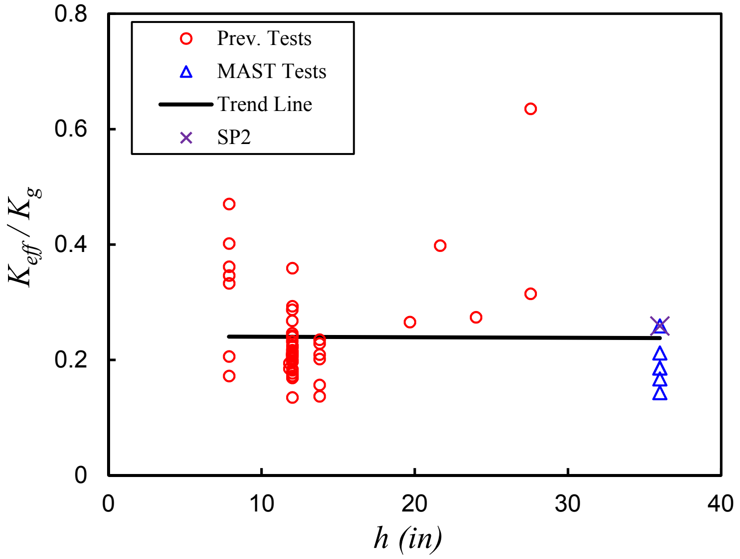

(a) $0 \leq P/f'_c A_g < 0.2$; $2 \leq L/h < 3$

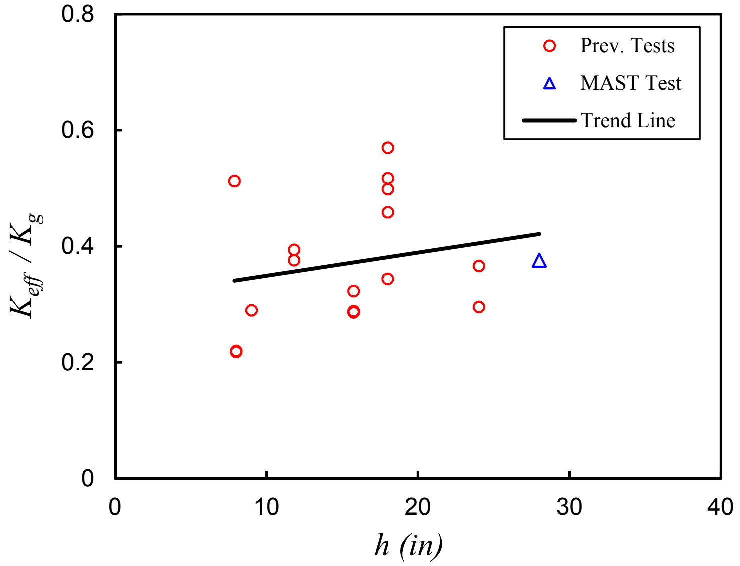

(b) $0.2 \leq P/f'_c A_g < 0.3$; $3 \leq L/h < 4$

Figure 3.8. Normalized Effective Stiffness vs. Cross-Sectional Depth

trends in some categories (i.e. the one shown in Figure 3.8(b) and others that are not shown for brevity) is believed to be related to the effects of other parameters which are not held constant, such as the reinforcement yield strength, longitudinal bar diameter, and reinforcement ratio.

3.7. DRIFT CAPACITY AND DISPLACEMENT DUCTILITY

3.7.1. Calculation

In this study, the drift capacity (δ_{80}) refers to the post-peak drift ratio corresponding to a 20% loss of the peak lateral loading capacity. Accordingly, the displacement ductility (μ_{Δ}) is defined as the ratio of drift capacity (δ_{80}) to drift at yield (δ_y) calculated according to the approach described in the previous section. Reported values for δ_{80} and δ_y by Ghannoum et al. (2012) and Sivaramakrishnan (2010) were utilized to investigate the influence of cross-sectional size on drift capacity and displacement ductility.

3.7.2. Influence of Axial Loading and Aspect Ratio

Similar axial load ratio and aspect ratio categories to those in the previous section were employed to investigate the effect of cross-sectional dimension. Drift capacities, shown in Figure 3.9(a) for $2 \leq L/h < 3$ which contains MAST test data, indicates a decreasing trend with axial load ratio. This trend is also present for more slender columns ($L/h > 3$) according to the trend lines given in Figure 3.9(b). Yet, for stocky columns ($L/h < 2$), the trend line in Figure 3.9(b) indicates that axial load ratio does not have a significant effect on the drift capacity. For slender columns ($L/h > 2$), a larger aspect ratio corresponds to a

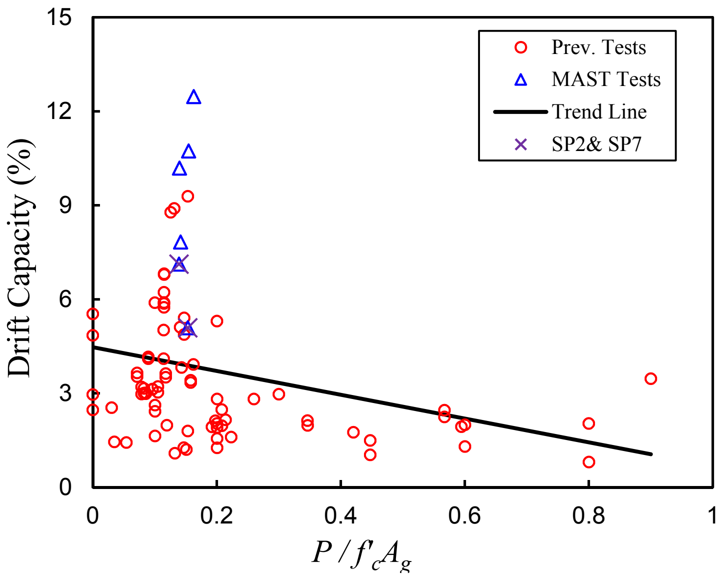

(a) $2 \leq L/h < 3$

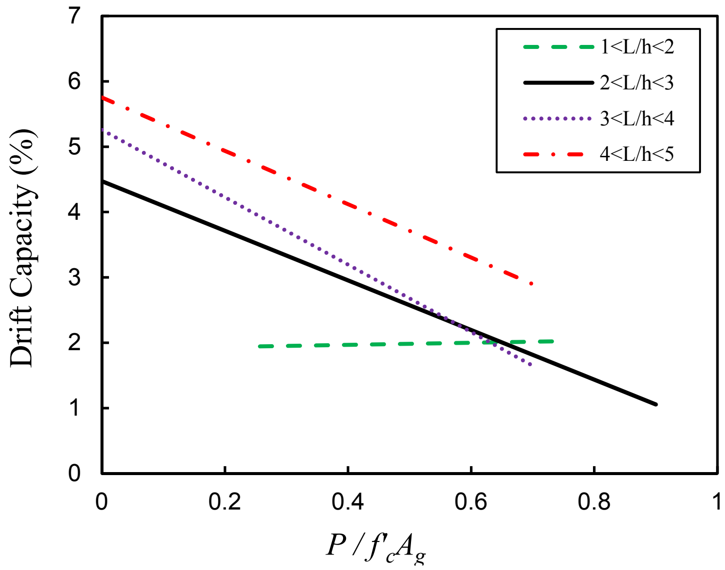

(b) Various *L/h*

Figure 3.9. Variation of Drift Capacity with Axial Load Ratio

smaller curvature demand to reach a desired drift ratio. But, it is accompanied by a more pronounced secondary (P-Delta) moment that results in a reduction in the drift capacity with increasing the axial load ratio. The drift capacity of the MAST test specimens exhibit a vertical distribution as shown in Figure 3.9(a) which is believed to be due to the effect of different loading protocols. In this figure, the column specimens subjected to fully symmetric loading protocols with many reversals (i.e. SP2, and SP7 that were subjected to loading protocols designed according to ACI 374-05 (ACI Committee 374, 2005) guidelines) exhibit the lowest drift capacities and fall much closer to the trend line than do the other MAST column specimens in the same category ($2 \le L/h < 3$).

Calculated values for displacement ductility exhibit more scattered patterns with variations in axial load and aspect ratio than those for drift ratio, such that a general trend could not be easily recognized and the plots are not shown here for brevity. This scatter can be traced to uncertainty in the estimation of the yield displacement from force-displacement plots of the specimens rather than measured yielding of the reinforcing bars.

3.7.3. Influence of Column Section Depth h

The drift capacity of the columns in the database are shown against their cross-sectional depths in Figure 3.10. To minimize the effect of aspect ratio and axial load ratio, the columns were categorized in the manner used in previous sections, however, only the data for column categories containing MAST data are shown in Figure 3.10(a) and Figure 3.10(b). The trend line in Figure 3.10(b), suggests that the drift capacity of columns is not generally a function of their cross-sectional size. Also, further analysis of the columns shown in Figure 3.10(a) reveals that the increasing trend in drift capacity with column size is dominated by the series of tests conducted at the MAST lab. The difference in the drift capacity of the MAST column specimens with similar cross-sectional depths (i.e. 36 in. (914 mm)) is related to their distinct loading protocols, and loading protocol was observed to have a significant effect on the drift capacity of columns. Similar observations have been reported (Pujol, 2002). Limiting the MAST data to include only the specimen with the symmetric cyclic loading protocol (i.e. column SP2 in Table 3.1), modifies the trend line in Figure 3.10(a) such that it is independent of the cross-sectional size. Therefore, the MAST tests reveal insensitivity of the drift capacity with variations in the cross-sectional depth for columns subjected to similar cyclic loading protocols.

Displacement ductility is expected to follow the same relationship with cross-sectional depth as does drift capacity, because the idealized drift at yield is independent h (not shown here for brevity). Comparison of the displacement ductility for the specimens relative to cross-sectional depth, shown in Figure 3.11, exhibits a similar relationship to that shown in Figure 3.10 for drift capacity. Slight ascending or descending trends in the ductility of these columns with h is believed to be related to the effect of the loading protocol, or to slight changes in aspect ratio and axial load ratio within each category.

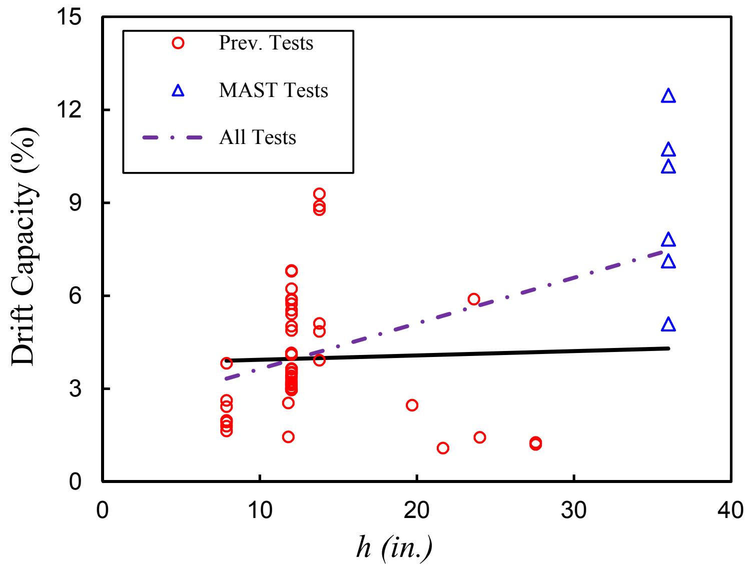

(a) $0 \le P/f'_cA_g < 0.2$; $2 \le L/h < 3$

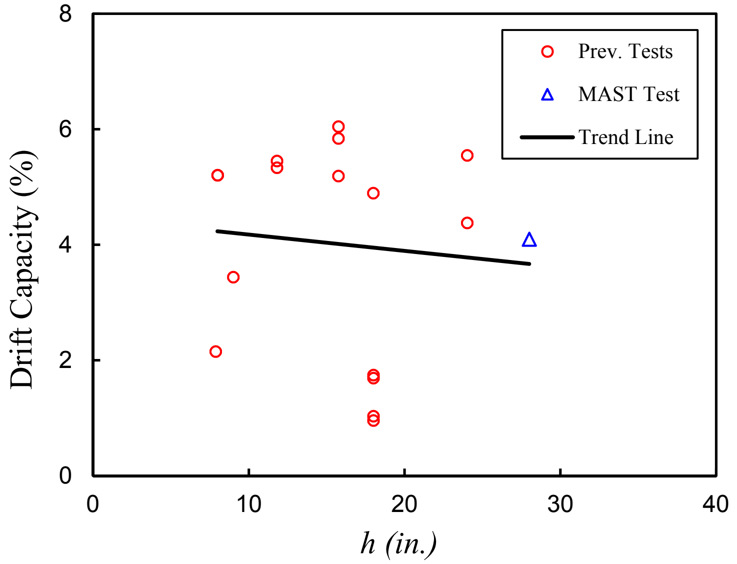

(b) $0.2 \le P/f'_cA_g < 0.3$; $3 \le L/h < 4$

Figure 3.10. Variation of Drift Capacity with Cross-Sectional Depth

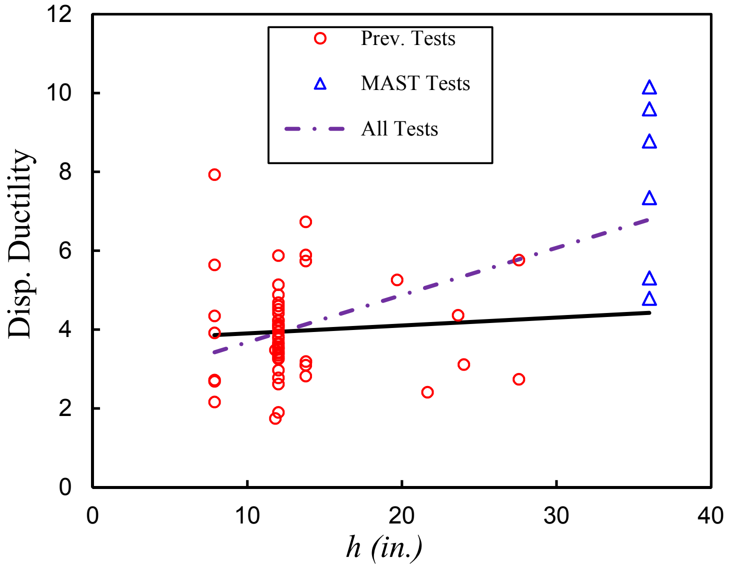

(a) $0 \leq P/f'_c A_g < 0.2$; $2 \leq L/h < 3$

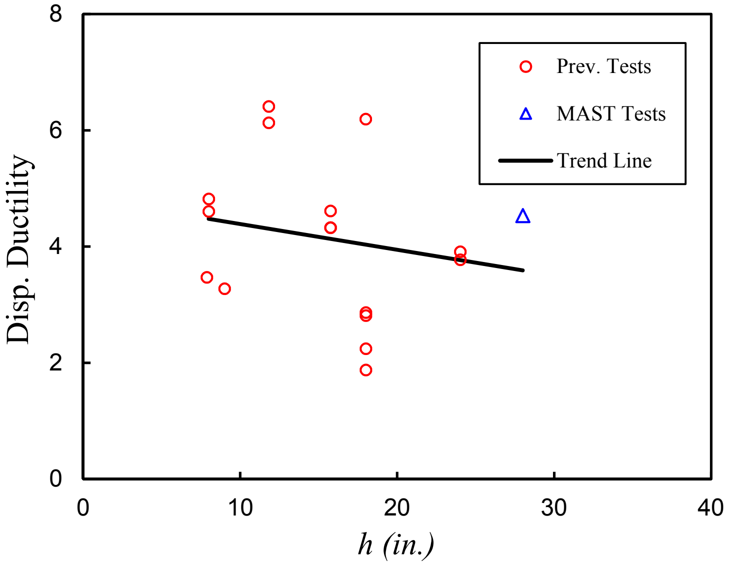

(b) $0.2 \leq P/f'_c A_g < 0.3$; $3 \leq L/h < 4$

Figure 3.11. Variation of Displacement Ductility with Cross-Sectional Depth

3.8. REINFORCING BAR BUCKLING

Buckling of reinforcing bars in an RC column is a complicated phenomenon that depends on the interaction of cover concrete, transverse reinforcement, concrete core, and loading history. Compression from applied forces on a RC column causes the concrete core to expand laterally due to Poisson’s effect, dilatation and shear deformation, which in turn mobilizes the confinement reinforcement that restrain the bars from buckling. Furthermore, the cover concrete, if un-cracked, can also restrain the bars from buckling outward. The longitudinal bars experience cyclic tension and compression during the evolution of a seismic event and eventually yield under larger deformations. Upon load reversal and before the cracks close, the longitudinal bars on one face of the column carry all of the axial load. Accumulation of plastic deformation in tension elongates the longitudinal bars, and when the elongation is combined with outward pressure from the concrete core and the high axial loads from building weight, bar buckling can occur. Once buckled, the bars lose a significant portion of their strength and stiffness and may eventually fracture due to large plastic strain reversals at the location where a kink forms in response to buckling.

3.8.1. Characterization of Reinforcing Bar Buckling

Different researchers have employed a variety of approaches to define the onset of buckling from experimental observations. Some researchers (Bayrak & Sheikh, 1996; Saatcioglu & Grira, 1999) recognized the onset of buckling based on observations at or near the end of the test. Brown et al. (2008) assumed an arbitrary lateral displacement of the bar equal to 1% of the column diameter, equivalent to 0.2 in. (51 mm.) for their test specimens, as the onset of buckling. On the other hand, Bournas and Triantafillou (2010), considered a sudden increase in the compressive strain of the longitudinal bars, after yielding, as a sign of bar buckling. Because there is no consensus for a unified method to measuring lateral displacement of the reinforcing bars at the onset of buckling in rectangular RC columns in the database, any general conclusion regarding the influence of the cross-sectional size on the drift ratio at the onset of buckling would lack sufficiently accurate supportive data. Instead, in this study, some observations from the tests conducted by the authors at the MAST Lab are presented to provide an insight into the effect of cross-sectional size on the mechanism of bar buckling.

For MAST tests, strain gages (Figure 3.12) were installed at a 6-in. (152.4-mm) spacing along the height of four longitudinal bars in each column specimen. While fracture of the longitudinal bars are typically followed by a marked drop in the load carrying capacity as shown in Figure 3.13, bar buckling, as a local phenomenon, is barely observable from strain histories of gages located far from the buckling zone. Therefore, the location of the buckled sections (i.e. sections with a maximum lateral deformation) along the bar were determined after each test and the strain gages right above and right below the buckled sections were identified. While a sudden strain variation could be recognized from these strain gages, investigation of the other strain gages revealed that regions of the bar away from the buckling section could still be in their elastic range of constitutive behavior. Thus, readings from the two strain gages located immediately above and below the buckled section of the bars were utilized to determine the drift at the onset of buckling.

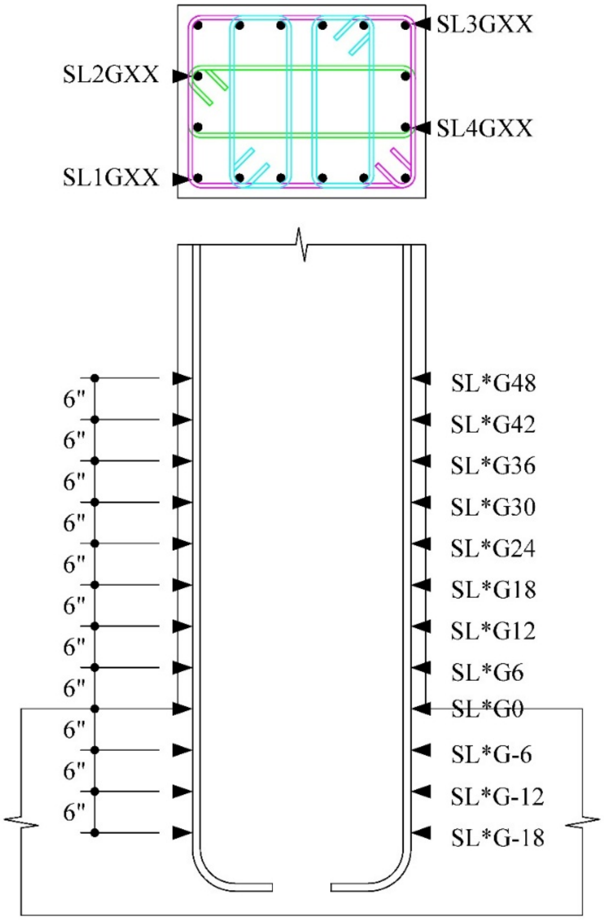

Figure 3.12. Location of Strain Gages for Cross Sections of MAST Test Specimens

Measured strain for a gage in specimen SP2 located at the proximity of a buckled bar is illustrated in Figure 3.14. The circles and squares denote the largest strains in compression and tension, respectively, in the preceding cycle after which a reduction in the measured compressive strain is observed. These points coincide with drift ratios of 1.87% for specimen SP2 in the compression and tension directions of the bar, respectively (Figure 3.14(b)). The circle corresponds to a cycle where the buckling is believed to start

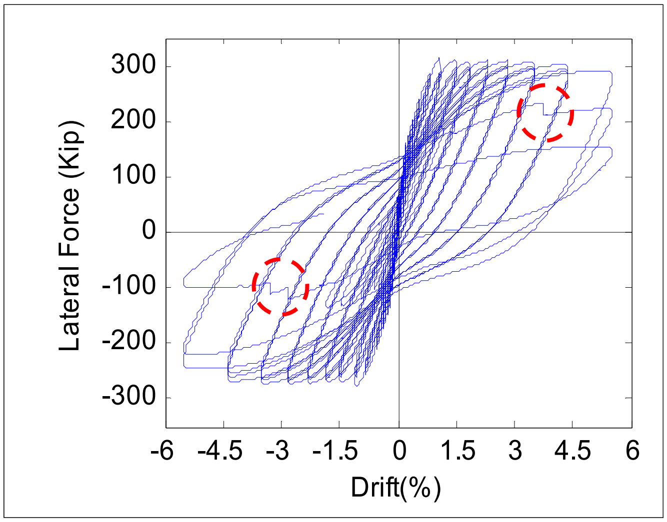

Figure 3.13. Sudden Drops in Load Carrying Capacity due to Bar Fractures

as the compressive strain decreases in the following cycles. This definition of the onset of buckling is consistent with the one by Bournas and Triantafillou (2010) in terms of a reduction in the compressive strain in the loading cycles that follow bar buckling. It has also been stated by other researchers that a reduction of the compressive strength due to bar buckling is preceded by a large pre-strain (i.e., a large excursion in yield strain) in tension (Brown et al., 2008; Massone, Polanco, & Herrera, 2014). This point is indicated by a square in Figure 3.14. The horizontal span with low strain variations, between steps 20,000 and 25,000, in Figure 3.14(a) refers to a pause in testing before application of the next level of displacement cycles. The next level of applied displacements was accompanied by a sudden drop in the tensile strain as shown by a triangle, which can be due to kinking of the bar following buckling and after which the measured strain data are not reliable.

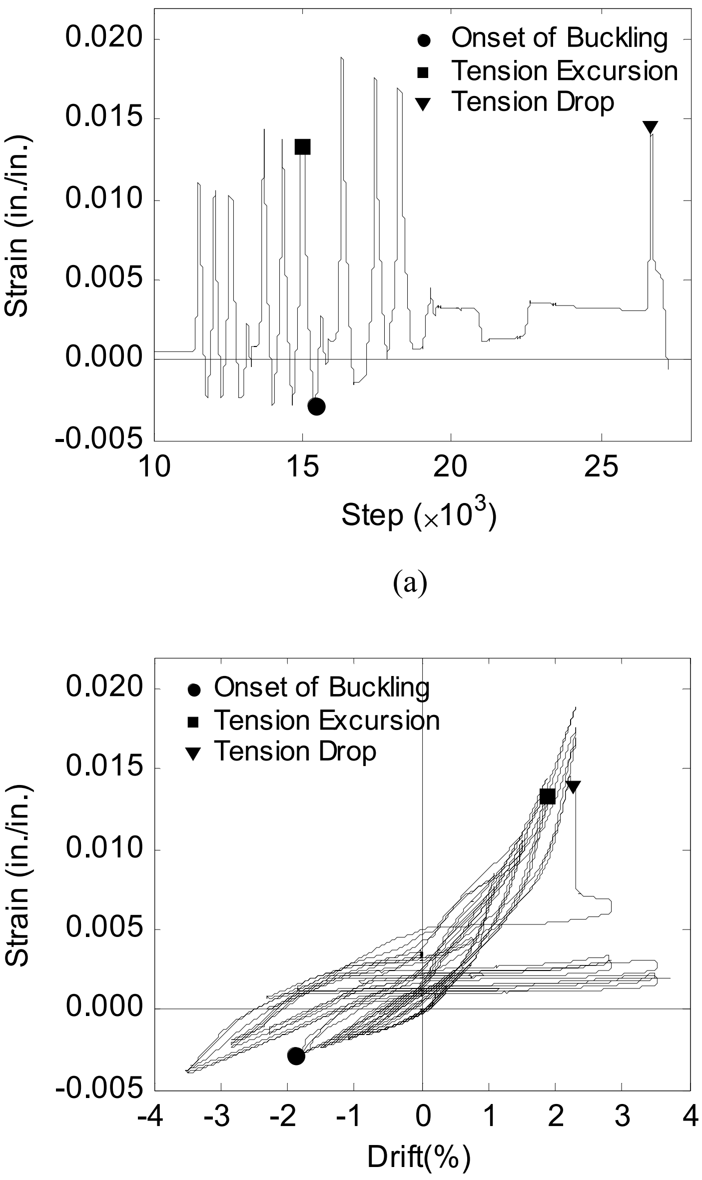

(a)

(b)

Figure 3.14. **Characterization of the Onset of Bar Buckling**

A criterion for determination of the approximate strain value to cause buckling can be taken from the equation proposed by Pantazapoulou (1998) which relates the strain at the onset of buckling to the bar diameter and its unsupported length, and it results in a strain of 0.010 and 0.011 for No.8 and No.9 bars, respectively. However, validity of the estimated strains based on Pantazapoulou's equation depends significantly on the strain compatibility condition in the specimens which can be violated in many cases due to cracking of the specimens during construction, shipping, installation, or small pretest cycles. Therefore, Pantazapoulou's equation was not considered as a criterion to define the onset of bar buckling, rather it was used as an approximate initial estimate of expected bar strains at buckling.

For each column specimen, the drift ratios at the initiation of buckling for the two strain gages closest to the buckled region on each reinforcing bar were determined using the approach described above. The average of the drift ratios at buckling for all four instrumented bars in the compression face of each column specimen was assumed to represent the drift ratio at the onset of buckling (δ_b) as indicated in Table 3.3. Most of the bars developed a kinked region at buckling which eventually fractured during subsequent loading cycles due to low-cycle fatigue. Table 3.3 indicates that the drift ratios at bar fracture (δ_F) can be significantly larger than the drift ratios at the onset of bar buckling depending on the loading conditions. Berry and Eberhard (2005) proposed an equation to estimate the drift ratio at the onset of bar buckling based on a statistical study of a dataset of columns. However, the data used to calibrate their equation was based on visual inspection of the specimens at or near the end of the tests to determine buckling of the bars.

As a consequence, their equation tends to overestimate the drift ratios at the onset of bar buckling for column specimens that experienced many displacement cycles before fracture of the bars (SP2, SP3, SP5, and SP7) as shown in Table 3.3. In fact, for these columns, the estimated drift ratios according to their proposed equation ($\delta_{calc.}$) are closer to actual drift ratios at fracture of the bars than the onset of buckling. Additionally, for column specimens that experienced fewer loading cycles (SP1 and SP6 in Table 3.3), their proposed equation tends to underestimate the drift ratio at the onset of buckling. The bar splices were located away from the column-footing interface in these columns. Having mechanical bar splices at or near the column base may result in a change in the drift ratio at the onset of buckling. However, these splices are typically not recommended to be placed at the yielding zone (i.e., near the column base) of RC columns in special moment resisting frames of Seismic Design Categories C, D, E and F according to seismic provisions in chapter 21 of the ACI 318-11 (2011).

Table 3.3. Drift Ratios at the Onset of Bar Buckling and Fracture

Specimen	δ_b (%)	δ_f (%)	$\delta_{calc.}$(%)
SP1	8.56	11.60	4.77
SP2	1.96	5.27	4.67
SP3	2.05	4.64	4.66
SP4	2.21	10.23	4.66
SP5	2.14	4.17	4.17
SP6	6.56	10.10	4.71
SP7	1.80	4.24	4.63

3.8.2. Influence of Column Section Size

Unlike flexural moment capacity, drift capacity, and ductility, observations from the tests carried out at the MAST lab suggest that longitudinal bar buckling can be affected in a significant way by the cross-sectional size of the columns. It is well accepted from previous tests that confinement provided by transverse ties is required to prevent or postpone bar buckling in rectangular RC columns. However, the MAST tests indicate that larger reinforcing bars (No. 8 and No. 9) in columns made with normal strength concrete can buckle in an in-plane mode (i.e. parallel to the face of the column) instead of outward because the concrete cannot provide sufficient support to the bars parallel to the ties. In-plane buckling in these bars occurred about the strong axis of the bars, which is contrary to the common assumption that bars will only buckle about their weak axis.

Larger columns typically support a larger amount of axial load that requires larger bar sizes. Compared to smaller columns, cover concrete is less effective in restraining larger bars from buckling in bigger columns since it will crack at earlier stages of loading due to the larger tensile forces carried by the longitudinal bars. This phenomenon makes columns with larger cross-sectional dimensions more prone to bar buckling. Additionally, the concrete surrounding the longitudinal bars is more susceptible to cracking and crushing in bigger columns because it restrains larger longitudinal bars, which require much larger restraint stresses to avoid buckling. Therefore, even if the bars are well restrained from buckling outward by transverse ties, they are still prone to buckle sideways, and this buckling mode can significantly reduce their load carrying capacity in the post-peak region of the buckled bars. In-plane buckling of bars, as shown in Figure 3.15, was observed in all tested specimens and it affected 36% of the buckled bars excluding those located at the corners. The corner bars were excluded as their final buckled configuration was typically a combination of outward and in-plane buckling. In many cases, no tie fracture or tie opening was observed. However, after crushing of the concrete core, the bars were observed to have clearly buckled parallel to the face of the column, and the buckling usually occurred over a distance equal to two times the tie spacing with the middle tie offering no restraint to the buckled bar.

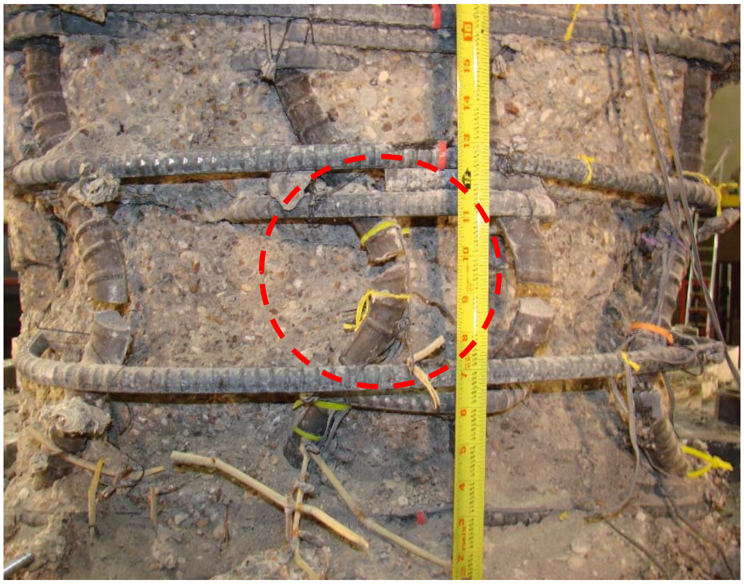

Figure 3.15. **In-Plane bar buckling and Fracture in MAST Column Tests**

3.9. CONCLUSIONS

In this study, results from recent tests conducted at the MAST lab on full-scale RC columns were combined with available dataset of RC columns to assess the effect of cross-sectional size of columns on their seismic performance. A study on the parameters representing seismic performance of RC columns confirms that effective stiffness, drift capacity, and displacement ductility of RC columns can be significantly affected by axial load and aspect ratios. In the case of drift capacity, the effect of axial load for stocky columns with aspect ratio smaller than 2 is minor. However, for columns with larger aspect ratios, the axial load ratio has an adverse effect on the drift capacity. This analysis also confirms the sensitivity of the drift capacity and displacement ductility to loading history. Test data analysis reveals that flexural moment capacity, drift capacity, and displacement ductility of RC columns constructed with normal to moderately high strength concrete (2.5 ksi (17.24 MPA) $\leq f'_c \leq$ 10 ksi (68.94 MPA)) are not generally affected by the dimension of their cross-sectional depths. However, observations from MAST tests imply that bar buckling as an important seismic damage state can start at earlier drift ratios in larger columns. These observations also suggests that despite bar fracture, which is typically followed by a marked reduction in lateral load capacity, realization of the drift at the onset of buckling requires proper sensor installation in the proximity of buckling zone. The MAST tests revealed a mode of bar buckling seldom seen and never considered in structural engineering of RC columns, the in-plane buckling mode in which the bars buckle parallel to the face of the column rather than in the outward direction. In the observed cases of in-plane bar buckling during the MAST tests, the bars deformed over a height equal to two times the tie spacing (i.e. skipping the middle tie) and deflected sideways into the cover on either side. This mode of buckling typically occurred about the strong axis of the bars while the common assumption is that longitudinal bars buckle only about their weak axis. From the MAST test observations, it is suggested that in-plane buckling initiates when the cover concrete crushes and there is compression damage (softening) to the portion of the core on either side of the buckled bars.

CHAPTER 4

IN-PLANE BUCKLING OF LONGITUDINAL BARS IN REINFORCED CONCRETE COLUMNS UNDER EXTREME EARTHQUAKE LOADING[3]

4.1. SUMMARY

Seven full-scale reinforced concrete (RC) columns were tested at the Multi-Axial Subassemblage Testing (MAST) Laboratory of the University of Minnesota to investigate their performance under extreme seismic events. The specimens were designed according to seismic provisions of ACI 318-11 (ACI Committee 318, 2011) and incorporated closely-spaced transverse hoops at their base. However, at large drift ratios during these tests, longitudinal bars were observed to buckle parallel to the face of the columns with transverse ties having little effect. This previously unobserved bar buckling phenomenon is investigated numerically to gain a better understanding of the column characteristics that affect it. First, a bar-spring mechanical model is used to understand the conditions needed to prevent buckling of longitudinal bars by means of restraints with finite stiffness. Second,

---

[3] Under review by Engineering Structures Journal.

a three-dimensional (3D) nonlinear finite element analysis of the lower portion of the specimen subjected to monotonic loading was formulated in ABAQUS and validated with test data. The analysis reveals that columns featuring larger cross-sectional dimensions and longitudinal bar sizes and lower strength concrete are more prone to in-plane bar buckling.

Keywords: reinforced concrete; column, bar buckling, in-plane buckling, finite element modeling

4.2. INTRODUCTION

Reinforcing bar buckling is a complex phenomenon that can reduce ductility of RC columns and lead to significant stiffness reduction and strength loss. The complexity of this phenomenon is attributed to the fact that the reinforcing bar buckling in RC columns involves both material and geometric nonlinearities and depends on several parameters including tie spacing and effectiveness, spalling of cover concrete, expansion of concrete core, and loading history. Due to the complexity of the problem, many prior experimental and analytical studies were carried out on isolated bars under compression to investigate bar buckling behavior. Experimental investigations showed that the behavior of bars in compression is generally different from that in tension (Dhakal & Maekawa, 2002; Bae, Mieses, & Bayrak, 2005) and hence analytical formulations were proposed to capture the constitutive relations of compression bars including buckling (Monti & Nuti, 1992; Gomes & Appleton, 1997; Rodriguez et al., 1999). Additionally, the investigations revealed that the post-yield behavior of reinforcing bars under compression is generally controlled by the ratio of their unsupported length to bar diameter (s/d_b) as well as their eccentricity to bar diameter ratio (e/d_b) (Bayrak & Sheikh, 2001; Bae et al., 2005). Considering the major role of transverse ties in controlling the bar buckling, some research studies idealized the bar buckling problem as a system of bar and springs with the springs representing the axial stiffness introduced by transverse ties (Dhakal & Maekawa, 2002; Papia et al., 1988).

In all the former studies of bar buckling in RC columns, it is assumed that the bars will buckle outward, that is perpendicular to the nearest column face, and the transverse ties are essential in restraining them from buckling. However, recent tests carried out at the MAST Lab in the Department of Civil, Environmental and Geo- Engineering of the University of Minnesota on full scale RC columns subjected to extreme loading conditions similar to what the columns experience during extreme seismic events revealed another buckling mode in which the bars buckled parallel to the compression face of the columns (in-plane bar buckling). In several instances, the ties were observed to still be effective in restraining the bars from outward buckling. However, after extensive damage to the concrete surrounding the bars, the reinforcing bars buckled over a height equal to twice the tie spacing and exhibited large lateral deformations parallel to compression face of the columns.

The main restraint against in-plane buckling is the concrete surrounding the bars, especially the concrete residing between adjacent bars (i.e. the concrete "teeth"). This concrete, while being within the column core, tends to be the portion of the core that gets damaged earlier and to a greater extent during a load test. Extensive damage to the concrete surrounding the bars would typically happen under large seismic loading conditions during which concrete exhibits severe inelastic behavior. The unique control and loading capabilities of the MAST Lab provided the opportunity to continue loading of the specimens far beyond the extent of loading in previous tests on RC columns. During these tests, the loading continued until the specimens lost more than 80% of their lateral load capacity whereas in almost all previous tests, loading was terminated after a 20% strength loss. In the authors' opinion, such an extended loading regime provided the chance to observe a failure mechanism in RC columns that was not addressed in previous tests.

In this study, first the required lateral restraint to prevent bar buckling is investigated numerically using finite element (FE) modeling of isolated bars. In practice, the lateral restraint can be provided by transverse ties in the case of outward deformation, or by concrete surrounding the bars (i.e. the "teeth") in the case of in-plane deflection. Results from analysis of the isolated bars are then utilized in a nonlinear finite element model in ABAQUS/Explicit to investigate the observed failure mechanism in the longitudinal bars of tested column specimens. The model was validated with experimental data and employed to explore the influence of several parameters that can affect in-plane buckling of the bars.

4.3. EXPERIMENTAL PROGRAM

The columns tested at the MAST Lab represent the lower portion of typical columns on the ground floor of a moment resisting frame in a high-rise building. The column specimens were designed according to seismic provisions of ACI 318-11 (2011) and featured two distinct cross-sectional dimensions: 36×28 in. and 28×28 in. (914×711 mm.

and 711×711 mm.). The specimens were built using normal-strength, normal-weight concrete with 28-day nominal compressive capacity *(f'_c)* of 5000 psi (34.47 MPa), ASTM A706 (2003) Grade-60 No. 8 and No. 9 steel reinforcing bars confined by ASTM A615 (2003) Grade-60 No. 5 steel hoops. Transverse hoops were placed at close spacing in the base of the columns to prevent outward bar buckling and ensure ductile behavior (Figure 4.1).

At the beginning of each test, a constant axial load was applied on top of the specimens (Figure 4.1) and kept constant during the tests. To simulate behavior at near-collapse conditions during extreme seismic excitation, the column specimens were then subjected to either a monotonic or one of several progressively increasing displacement reversals until they lost more than 80% of their lateral loading capacity. Further details regarding these tests can be found elsewhere (Nojavan et al., 2015).

4.4. TEST OBSERVATIONS

When the lateral loading was applied to the column specimens, flexural cracks formed on tensile face of the columns (Figure 4.1). Flexural cracking initiated at approximately 0.2% drift level, which was equal to 6 mm of the crosshead displacement. Additionally, flexure-shear cracks formed in the lower portion of the other two faces of the columns and longitudinal cracks were observed along the corners on the compression sides. Following concrete cracking, the longitudinal bars started to yield at approximately 0.5% drift ratio (15 mm of crosshead displacement). However, the columns exhibited further lateral load

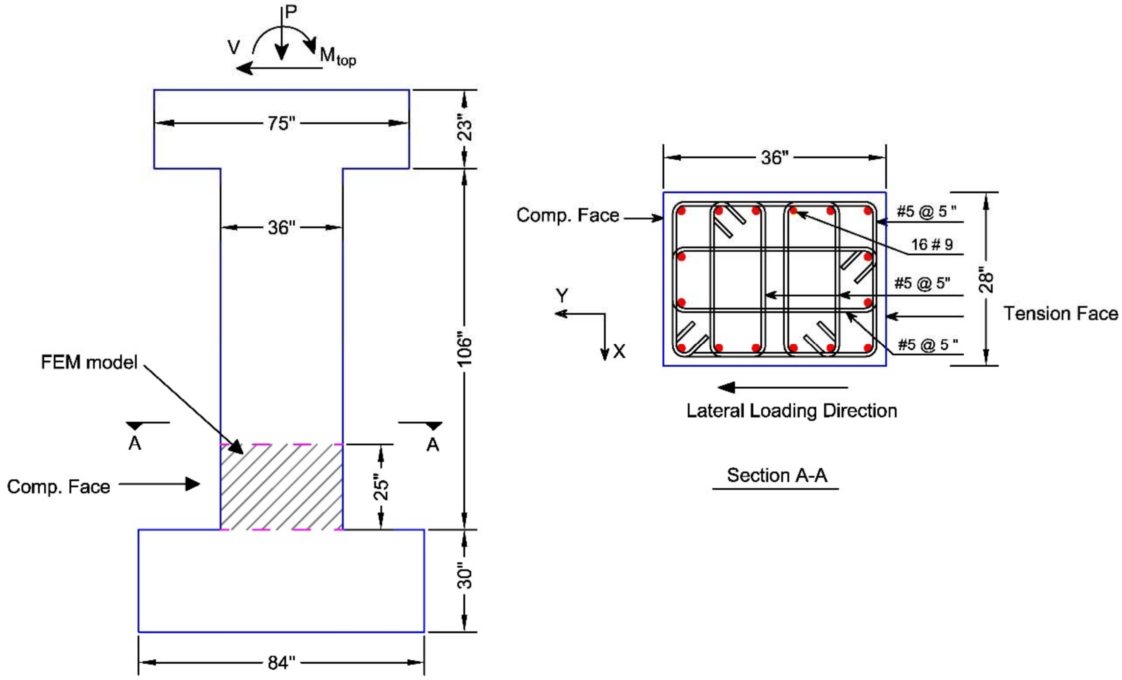

Figure 4.1. Specimen Geometry and Detailing

capacity due to confining pressure from the transverse reinforcement and strain hardening of longitudinal reinforcement. An increase in lateral load was accompanied by more crack developments and propagations. Finally, the specimens started to lose flexural strength due to crushing of the cover concrete and buckling of the longitudinal bars. The columns exhibited severe strength loss by the end of the test (more than 80% of their peak lateral load capacity) following the fracture of the buckled bars and extensive damage to the concrete around the perimeter.

While it is commonly assumed that longitudinal bars in an RC column would buckle in the outward direction (i.e. perpendicular to the compression face of the column), investigation of the buckled bars at the end of the tests conducted at the MAST lab indicated that this assumption is not necessarily true in all cases. Instead, it was observed in all tested specimens that some of the bars buckled parallel to the compression face of the columns (Figure 4.2). More specifically, when only the two middle bars on compression faces of the columns in monotonic and cyclic uniaxial tests at the MAST Lab are considered, 10 out of 24 bars (i.e., 42% of the total observed buckling cases) revealed either a complete or a dominant in-plane buckling mode. A buckling mode is considered to be completely in-plane when no out of plane translation is observed in the buckled region whereas if a small outward translation is present in conjunction with large in-plane translation, it is considered a dominant in-plane buckling mode.

Another observation is related to the axis of bending in the buckled bars. Since reinforcing bars incorporate ribs along their length, they have strong and weak axes of bending. In practice, longitudinal bars are typically oriented in a way that their outward deformation (i.e. deflection perpendicular to the column face) mobilizes flexural rigidity corresponding to the weak axis while their in-plane deflection (i.e., deflection parallel to the column face) occurs about their strong axis of bending. In many of the observed cases of buckled bars in-plane buckling occurred about the strong axis of bending of the bars, which is contrary to the common assumption, that is supported by experimental results from isolated bars, that the bars would only buckle about their weak axis.

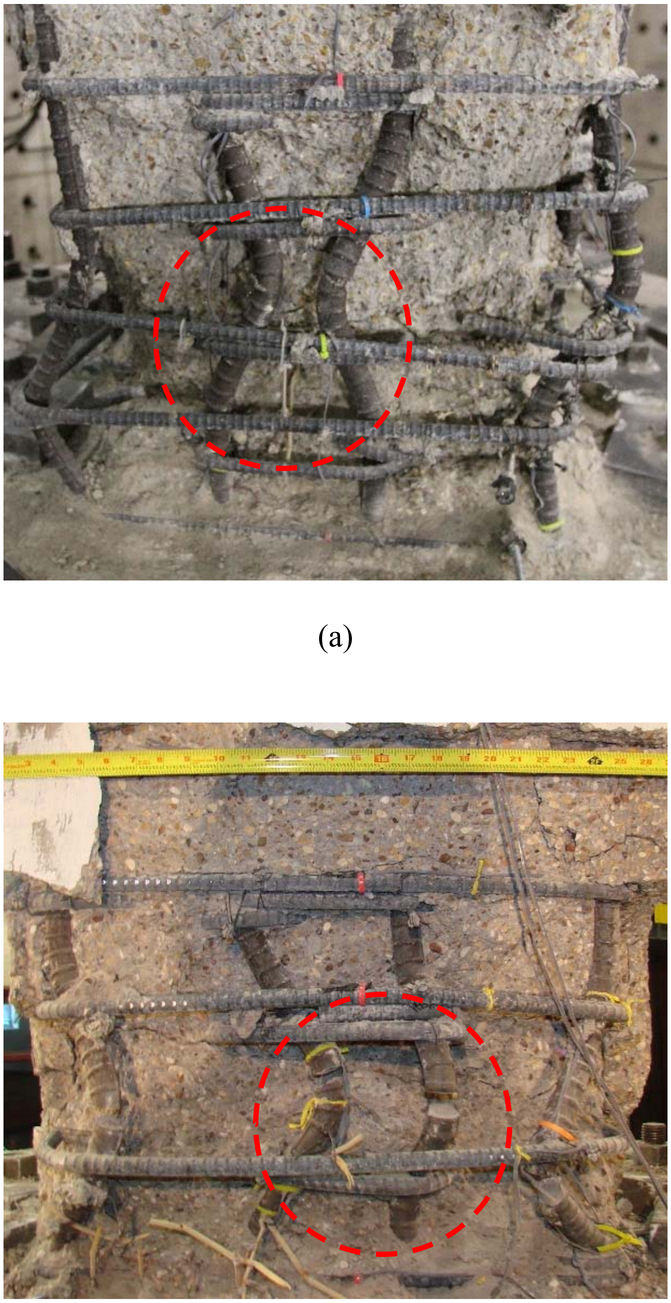

Figure 4.2. In-Plane Bar Buckling During Tests at the MAST Lab: (a) Column Specimen under Monotonic Loading, (b) Column Specimen Subjected to Cyclic Loading

4.5. ANALYTICAL INVESTIGATION USING BAR-SPRING MODEL

A bar and spring model is used to investigate the demands on lateral restraints that have finite stiffness to prevent buckling of longitudinal reinforcing bars. For outward (i.e., out-of-plane) buckling, these restraints are the hoops or ties that are also used as shear reinforcement and reinforcement for confinement. For in-plane buckling, the restraints are provided by the concrete that bears against the longitudinal reinforcement.

4.5.1. General Description of the Bar-Spring System

The buckling behavior of bars can be simply modeled with a bar-spring system as illustrated in Figure 4.3 where springs represent the axial stiffness of the ties preventing the bars from buckling. Dhakal and Maekawa (2002) employed such model to estimate the required tie stiffness for a stable buckling mode and to estimate the buckling length of the bars. Based on their investigation, Dhakal and Maekawa (2002) proposed Eq. 4.1 to estimate the required stiffness (K_n) for the n^{th} stable buckling mode as:

$$K_n = \alpha_n \frac{\pi^4 EI}{s^3} \tag{4.1}$$

Where according to their definition, n = the number of tie spacings within the buckled zone, s = tie spacing, EI = reduced flexural rigidity of the bars that depends on their yield strength (f_y), and α_n= a constant that depends on the stable buckling mode. For the case shown in Figure 4.3, in which the buckled length equals two tie spacings, the required tie stiffness to prevent the bars from buckling is calculated as 33.1, 166.1, and 408.3 kip/in. (5.8, 29.1, and 71.5 KN/mm) for No. 6, No. 9, and No. 11 bars, respectively, with α_n given as 0.1649 and assuming a yield strength (f_y) of 74 ksi (510.2 MPa) for longitudinal bars of the test specimens.

To further investigate the behavior of the buckled bars in the bar-spring system, a 3D finite element model of the system represented in Figure 4.3 was built in ABAQUS using 2-node shear flexible beam-in-space (B31) elements representing the longitudinal bar and a linear spring at its mid-height whose stiffness corresponds to the axial stiffness of the tie leg. The length of the bar (l) was selected equal to two times the tie spacing that was used in tested RC columns (i.e. s=5 in. (127 mm) and $l=10$ in. (254 mm.)). Behavior of the steel bar was modeled using a trilinear curve fitting the stress-strain curve of longitudinal bars in tested specimens with yield and ultimate strengths of 74 ksi and 112 ksi (510.2 MPa, and 772.2 MPa), respectively (Figure 4.4) while the elastic stiffness of spring was taken as constant during each analysis. A number of analyses with different bar sizes and values for spring stiffness were conducted.

An initial imperfection was introduced to perturb the bar geometry and mobilize buckling. In practice, this imperfection can be caused by misalignment or initial crookedness of the bars. To minimize the effect of the initial imperfection on the buckling load, a separate series of analyses were performed and the imperfection magnitude was selected sufficiently small such that estimated critical loads had a maximum error of 1% compared to the exact analytical solutions in the case of elastic bar. To simulate fixed

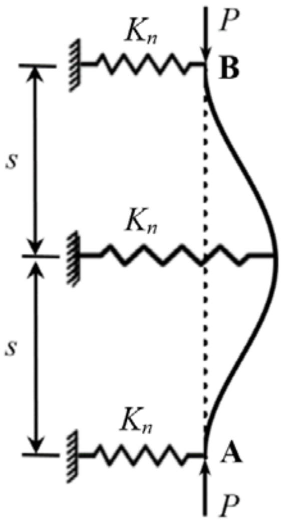

Figure 4.3. Bar-Spring System to Simulate Bar Buckling Behavior

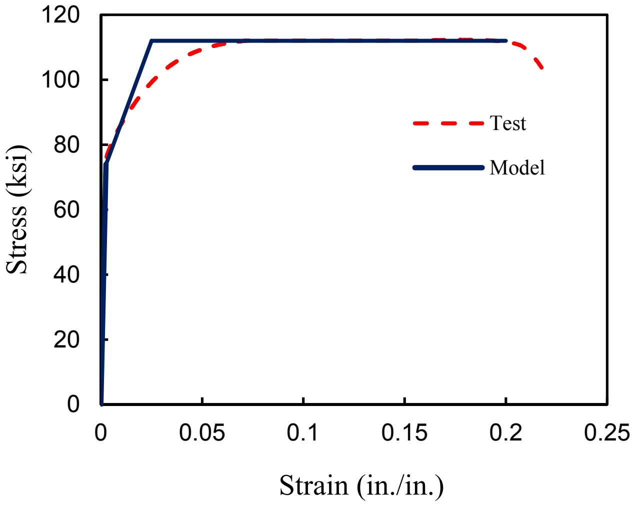

Figure 4.4. Stress-Strain Behavior of Longitudinal Bars

boundary conditions as assumed by Dhakal and Maekawa (2002), all degrees of freedoms (DOFs) at the top and bottom of the bar (Points A and B in Figure 4.3) were fixed except the vertical translation on the top (Point B). During each analysis, the vertical load on top of the bar increased gradually using Modified Riks (arc-length) method (Crisfield, 1981; Ramm, 1981; Powell & Simons, 1981) until the bar buckled.

4.5.2. Static Analysis Using Modified Riks (Arc-Length) Method

The modified Riks method was used to obtain static equilibrium solutions for this geometrically and materially nonlinear problem with emphasis on the effect of buckling on the descending branch of the force-displacement. The loading on the system is governed by a single scalar parameter, namely the load proportionality factor (λ), an arc-length and an iterative procedure that was used to determine a set of load and displacement at each increment that satisfies static equilibrium. The method is neither displacement nor load control, and the arc length includes components of both. The magnitude of loading at a specified increment is defined as follows:

$$P_{total} = P_o + \lambda \, (P_{ref} - P_o) \tag{4.2}$$

where P_o = the dead load (i.e., any load applied to the structure prior to the Static Riks step), λ = the load proportionality factor that changes in each load increment, and P_{ref} = the reference load (i.e., the load that is applied during Static Riks step). A unit load was applied to the bar during the Static Riks step (P_{ref}=1). Since, there are no other loads prior to the applied unit load, P_0 was equal to zero, hence the magnitude of the load proportionality factor, λ, represents the evolution of loading (P_{total}) during analysis.

4.5.3. *Results from Bar-Spring Analysis*

For each bar size in the study, a series of analyses were carried out with spring stiffness as the variable parameter. The applied axial loads for such analyses on No. 9 bars and various spring stiffness coefficients is represented in Figure 4.5, which indicates that the magnitude of critical load increases with a rise in the spring stiffness. However, beyond a stiffness of 50 kip/in (8.8 KN/mm.) the rate of increase in critical load with addition of stiffness drops significantly such that a spring that is 10 times stiffer would only slightly increase the critical load (i.e. less than 3%). Adding more stiffness will eventually activate higher buckling modes. A comparison of the estimated critical loads associated with different spring stiffness with those having stiffness as proposed by Dhakal and Maekawa (2002) reveals that their proposed equation overestimates the required spring stiffness to

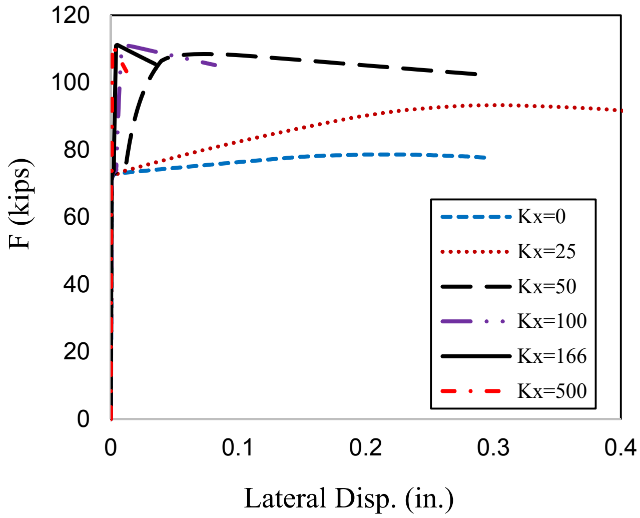

Figure 4.5. FE Analysis Results for a No. 9 Bar

prevent bar buckling (Table 4.1). Specifically, this analysis shows that a spring stiffness of 100 kip/in (17.5 KN/mm.) for No. 11 and 50 kip/in (8.8 KN/mm.) for No.9 bars would suffice to deliver the axial load capacity within 1% and 2.5% of those obtained from their proposed spring stiffness (i.e. 408 and 166 kip/in., respectively). In other words, providing 25% and 30% stiffness as of those estimated by Eq. 4.1 for No. 11 and No. 9 bars, respectively, can prevent the first mode of bar buckling with only a small reduction in the magnitude of the critical load (i.e., less than 3%).

The bar-spring system analogy can also be applied to the case of in-plane buckling of the bars. While longitudinal bars in RC columns are restrained by transverse hoops to prevent outward buckling, it is only the concrete surrounding the bars, as well as the friction between the bars and transverse hoops, that prevent them from buckling sideways (i.e., parallel to the compression face of the column). In this case, the spring stiffness would represent an initial stiffness provided by the surrounding concrete to restrain the bars from buckling. The demand on concrete stiffness would increase with an increase in bar size (Table 4.1). Assuming that the preventive effect of concrete on the in-plane bar buckling can be idealized by a system of discrete springs, Table 4.1 implies that when concrete with the same properties are used (i.e. similar spring stiffness) columns incorporating larger bar sizes are more vulnerable to in-plane buckling as their reinforcing bars require stiffer surrounding concrete (i.e. stiffer spring) to restrain the occurrence of in-plane buckling.

Table 4.1. Critical Loads from FE Analysis of Bar-Spring System

K_x *(kip/in.)*	*Bar Size*		
	No. 6	No. 9	No. 11
0	31.85	78.65	138.55
5	32.14	81.24	140.91
25	45.39	93.36	148.99
33	47.66*	99.00	152.80
50	48.79	108.52	165.79
100	49.23	110.96	173.76
166		111.16*	174.56
300		111.24	174.76
408		111.27	174.80*
500		111.28	174.81
800			174.84

* Represents buckling load calculated based on Eq. 4.1

4.6. FINITE ELEMENT MODELING OF RC COLUMN SPECIMENS

A three-dimensional, nonlinear finite element model is described here and used to simulate the observed in-plane buckling of the longitudinal reinforcement in the RC column specimens tested in the MAST Lab. The model focuses on the portion of the column adjacent to the base of the member, and it offers a more realistic representation of this portion of the columns than does the bar-spring model in the preceding section. The goal of the FE analysis is to simulate the phenomenon of in-plane buckling by means of a qualitative assessment, and to give an indication of the variables that may affect it.

4.6.1. General Description of the FE Model

A 3D finite element model representing the test columns was built in ABAQUS to investigate qualitatively the in-plane buckling of reinforcing bars in the tested specimens. Since the in-plane bar buckling was observed during test of the first specimen (SP1) under monotonic loading, SP1 was considered for model calibration of in-plane buckling behavior. Also, to reduce analysis cost, only the lower portion of column specimen SP1 (25 in. above the column base) was modeled because in-plane buckling was observed in this region (Figure 4.1).

The FE model was 25 in. (635 mm) tall and featured cross-sectional dimension of 36×28 in. (914×711 mm.) (depth × width) (Figure 4.6). Fixed boundary conditions were applied to the nodes at the column base whereas all translational and rotational Degrees of Freedom (DOFs) of the nodes on top of the column were constrained to a reference point at the centroid of the cross section. Constraining the nodes to the reference point eliminates singularity issues in the problem, while the loads are applied to the reference point. Concrete was modeled using 8-node brick elements with reduced integration and hourglass control (C3D8R). The maximum and minimum mesh size for concrete elements were 2.64 and 2.125 in. (67 and 54 mm.). Longitudinal bars were modeled with 2-node shear flexible beam-in-space (B31) elements. The bars, except those on the compression face, were defined within the concrete solid using embedment technique. In this approach, a perfect bond between embedded elements (reinforcing bars) and the host element (surrounding concrete) is assumed. The interaction between cracked concrete and longitudinal bars (i.e.,

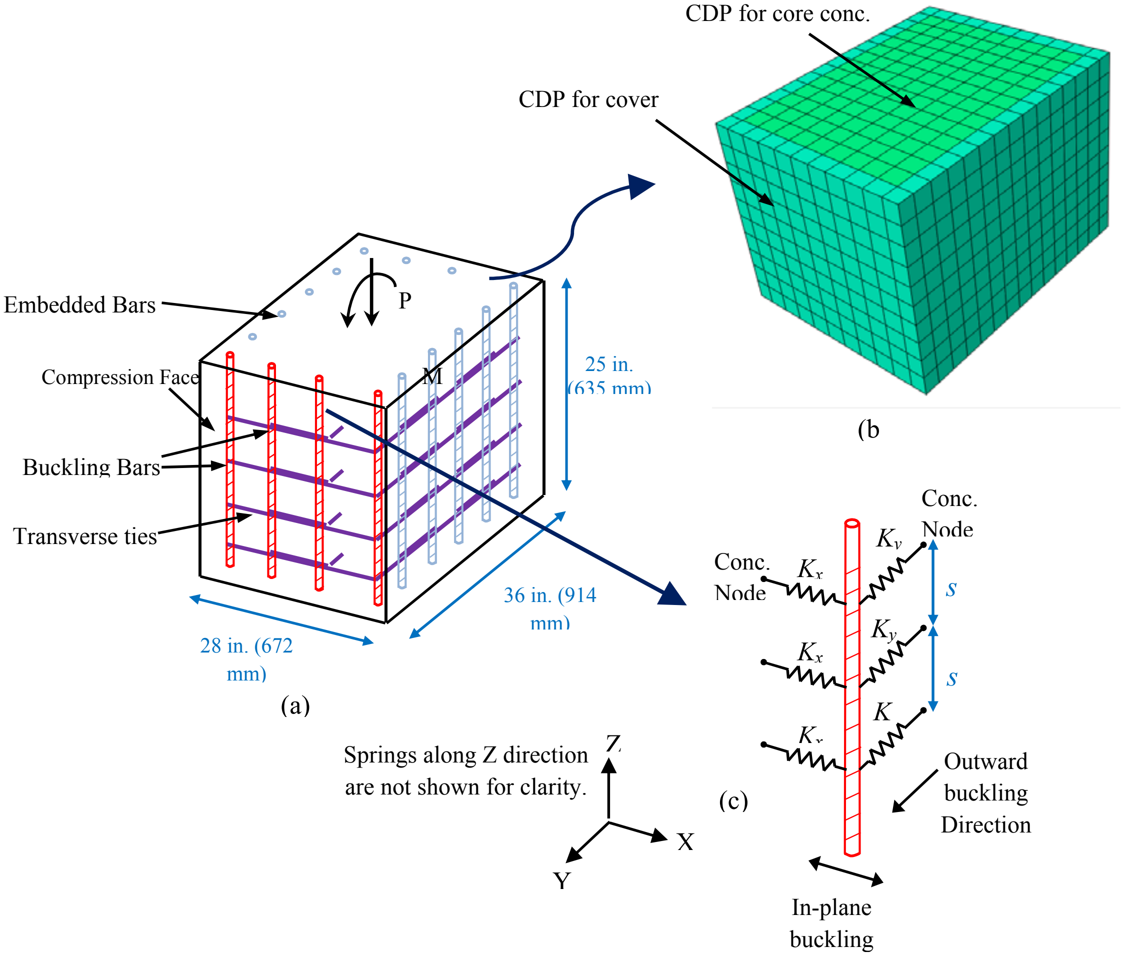

Figure 4.6. General Description of FE Model: (a) Modeled Section (b) Mesh of Concrete Material (c) Modeling of Buckling Bars within Concrete Elements

bond-slip) is defined by adjusting the strain softening behavior of concrete in tension (i.e., tension stiffening). When embedded, all translational DOFs at the nodes of embedded reinforcing bar elements are eliminated and these nodes are constrained to the interpolated values of corresponding DOFs at adjacent nodes of the host (concrete) element. As a result, bar buckling cannot be captured when the embedment technique is used since buckling involves a sudden lateral deformation of the bars free from the surrounding concrete. Thus, on the compression face where bar buckling is likely to occur, the bars were modeled as independent B31 elements. These independent elements were connected to the reference point on top of the specimen to move in accordance with the translation and rotation of the specimen top. On the other hand, restraining effects of the ties and surrounding concrete on the buckling bars were modeled using linear spring elements.

4.6.2. Estimation of Spring Stiffness

Given the proximity of most longitudinal bars to 90° bends in the ties, the spring stiffness associated with ties were defined on the basis of the axial stiffness of tie legs as follows:

$$K_{tie} = \frac{E_t A_t}{L_t} \times \frac{n_l}{n_b} \tag{4.3}$$

where E_t, A_t, and L_t are elastic modulus (200000 MPa), cross-sectional area and length of the tie leg, respectively. Also, n_l and n_b represent the number of tie legs in the direction of restraint and the number of bars that are restrained, respectively.

In the case of in-plane buckling, the restraining effect depends on the performance of the concrete surrounding the bars. An analogy of the preventive concrete pressure on the rebar to the force created in a discrete system of springs can be made in order to relate spring stiffness to the characteristics of the physical problem. For the concrete to act as an axial element, it is assumed that the concrete between adjacent longitudinal bars has begun to crack off from the rest of the core (i.e., micro-crack generation reducing stress transfer with the rest of the core) **(**Figure 4.7**)**. In that case, the secant stiffness can be idealized as follows:

$$K_s = \frac{P_{eff}}{\Delta_{eff}} = \frac{\sigma_{eff} A_{eff}}{\Delta_{eff}} \tag{4.4}$$

where Δ_{eff} = the maximum lateral displacement of the bar when it buckles, σ_{eff} = the concrete strength when the buckling starts, and A_{eff} = the effective contact area between bars and surrounding concrete which prevents the bars from in-plane buckling.

The maximum lateral displacement at the onset of in-plane buckling (Δ_{eff}) depends on many parameters (e.g. characteristic properties of the concrete surrounding the bars and its performance as well as that of the longitudinal bars, loading history, core concrete expansion and friction between ties and longitudinal bars) and its accurate measurement requires a careful instrumentation and monitoring of the longitudinal bars during the test. The bars which buckled in the in-plane mode during the MAST tests were observed to have a maximum lateral displacement between d_b and $3d_b$ by the end of the tests. Therefore, for the purpose of this study and because the onset of buckling is considered here, Δ_{eff} was assumed to be equal to d_b. It is further assumed that the effective strength of concrete at buckling (σ_{eff}) would be only a fraction of the compressive strength of core concrete since the concrete surrounding the bars will soften as the specimen is loaded in compression and flexure. The state of strain at the onset of in-plane buckling is unknown, thus the stress level is indeterminate. A lower bound estimate for the stress level is approximated

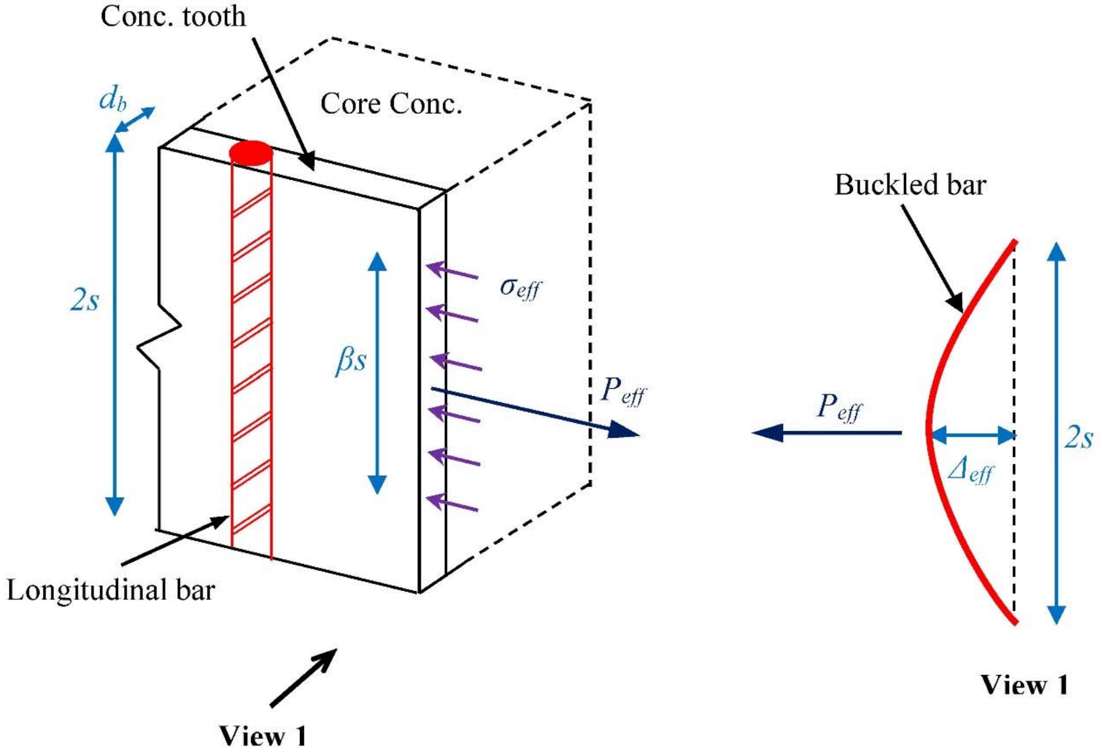

Figure 4.7. Preventive Effect of Surrounding Concrete from In-Plane Buckling after Cover Spalling

assuming that the concrete is deformed well into the post-peak range of compression behavior and its strength has degraded to the "residual strength" level that the Kent-Park concrete model (Kent & Park, 1971) quantifies as $0.2\lambda f'_c$, where λ is the factor that represents the strength enhancement due to confining reinforcement. Thus, Eq. 4.4 can be rewritten as follows:

$$K_s \cong \frac{(0.2\lambda f_c')[(\beta s)d_b]}{d_b} = 0.2\lambda f_c'\beta s \tag{4.5}$$

where *βs* = the dimension along the length of the bar in which the concrete is effective in restraining the buckling bar and *λ* is suggested by Kent and Park as follows:

$$\lambda = 1 + \frac{\rho_s f_{yh}}{f_c'} \tag{4.6}$$

where ρ_s = volumetric ratio of the hoops and f_{yh} = yield strength of the hoops. From experimental observations, the in-plane buckling length was typically equal to two times the tie spacing (2*s*). Therefore, assuming a half-sinusoidal shape over the observed buckling length, the deflected shape of the bar (before buckling) is given by

$$\frac{\Delta(x)}{\Delta_{max}} = \sin\left(\frac{\pi}{2}\frac{x}{s}\right) \qquad \text{for } 0 \le x \le 2s \text{ and } \Delta = \Delta_{\max} \text{ at } x = s \tag{4.7}$$

The concrete is assumed to provide restraint over the portion of the buckled bar with a lateral deflection $\Delta \geq 0.5\Delta_{\max}$, and at the location x_o, $\Delta = 0.5\Delta_{\max}$ which can be determined as follows:

$$\frac{\Delta(x)}{\Delta_{max}} = 0.5 = \sin\left(\frac{\pi}{2}\frac{x_o}{s}\right) \quad \text{or} \quad \frac{x_o}{s} = \frac{2}{\pi}\sin^{-1}(0.5) \approx 1/3 \tag{4.8}$$

The resulting effective length factor is

$$\beta = (2s - 2x_0)/(2s) = 2(1 - 1/3) = 4/3 \tag{4.9}$$

when substituted in Eq. 4.5, the effective (axial) stiffness of concrete springs is as follows:

$$K_s = \frac{4}{15}\lambda f'_c s \tag{4.10}$$

In the case of *SP1* with f'_c = 4.86 ksi (33.5 MPa), f_{yh}=60 ksi (413.7 MPa), s = 5 in. (127 mm), and ρ_s = 0.0148, λ would be 1.18 from Eq. 4.6 and the stiffness K_s will be equal to 7.65 kip/in. (1.35 KN/mm).

The behavior of the springs representing the axial stiffness of ties and restraining effect of concrete, was modeled differently in tension and compression. In the inward direction (i.e., -Y direction in Figure 4.6(c)), the concrete is assumed incompressible and hence the bars cannot bend inward whereas the tie stiffness will be activated when the bars deflect in the outward direction (i.e., +Y direction). In the case of lateral deformation (i.e., parallel to the column face), the behavior would depend on the geometry of the bar and transverse hoops. For the bar shown in Figure 4.6(c), it is only the concrete stiffness that restrains the bar from deflection in the -X direction (K_{x1}) whereas the tie legs would limit its deformation in the +X direction (K_{x2}). Distinct spring stiffness corresponding to the deflection of this bar in the +X and –X directions is represented in Figure 4.8. Additionally, the four bars on the compression face (i.e., buckling bars) were connected to their adjacent concrete elements using stiff linear springs along Z direction to simulate strong bond conditions as was assumed for the embedded bars.

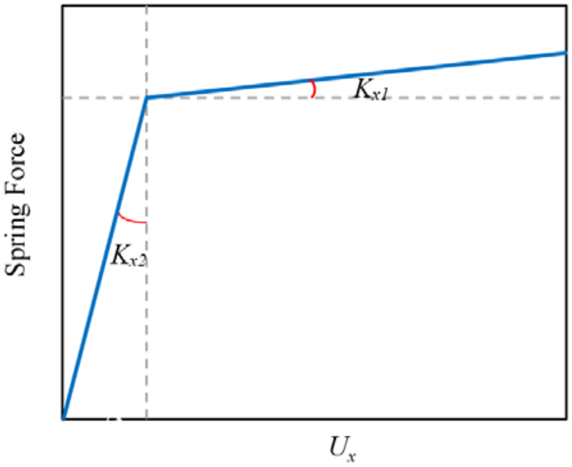

Figure 4.8. Spring Stiffness Parallel to the Column Face

4.6.3. *Modeling of Concrete Behavior*

Concrete behavior is modeled using Concrete Damage-Plasticity (CDP) implemented in ABAQUS/Explicit. The CDP model assumes two main limit states for concrete as cracking in tension and crushing in compression when concrete behaves in a brittle manner (i.e., under low confining pressure). Damage associated with these two failure mechanisms represents an isotropic stiffness degradation and is characterized independently in tension and compression by a single scalar parameter. Damage parameters in tension (d_t) and compression (d_c) are functions of hardening variables (also known as equivalent plastic strains, $\tilde{\varepsilon}_t^{pl}$ and $\tilde{\varepsilon}_c^{pl}$). Hardening parameters represent the evolution of the yield surface and stiffness reduction and are automatically calculated by ABAQUS from inelastic strains (i.e., total strain minus the elastic strain corresponding to undamaged material state). The CDP model uses the yield function proposed by Lubliner et al. (1989) with modifications proposed by Lee and Fenves (1998) to capture behavior in tension and compression. The potential plastic flow is based on the Drucker-Prager hyperbolic function and the flow rule is non-associated.

For the RC columns modeled herein, the elastic modulus of concrete was estimated as 3,974 ksi (27400 MPa) for a concrete with compressive strength of 4.86 ksi (33.5 MPa) according to Sec 8.5.1 of ACI 318-11 (2011). Except the dilation angle which was assumed as 30°, the default values were used for the other parameters in the CDP model. These default values are 1.16 for the ratio of the initial equibiaxial compressive yield stress to initial uniaxial compressive yield stress, 2/3 for the ratio of the second stress invariant on the tensile meridian to that on the compressive meridian, 0.1 for eccentricity and 0 for viscosity.

The stress-strain behavior of concrete in compression was assumed linear up to $0.45f'_c$ and defined according to the model proposed by Kent and Park thereafter. A different stress-strain behavior was considered for core concrete as compared to the one for cover concrete as illustrated in Figure 4.9 to account for the confining effect of rectangular hoops. The uniaxial tensile behavior of concrete was assumed linear up to a tensile yield stress (f_{t0}) of 0.522 ksi (3.6 MPa) calculated according to Sec 9.5.2.3 of ACI 318-11(2011). The post-peak behavior of concrete in tension (tension stiffening) was defined by specifying the fracture energy (G_f, the energy required to form a unit area of crack) as a material property. This model assumes a linear softening behavior after cracking in tension until a complete loss of tensile strength at a cracking displacement equal to $u_{t0} = 2G_f/f_{t0}$. Although suggested values for fracture energy of plain concrete are typically low, low values of this parameter often lead to numerical issues. Moreover, fracture energy is much larger in reinforced concrete due to the presence of distributed reinforcing bars (Mercan, Schultz, & Stolarski, 2010). In this study, a value for fracture energy equal to 0.001 kip/in. (1.76×10^{-4} KN/mm) was used for the concrete. Also, since calibration was done using only the RC column specimen under monotonic loading, damage parameters were not needed.

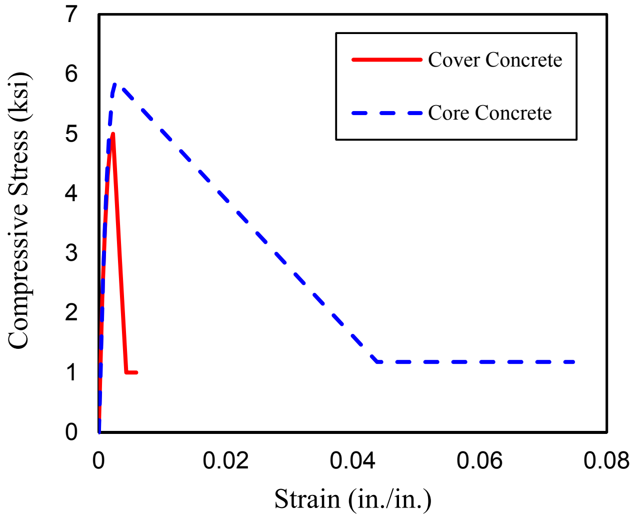

Figure 4.9. Stress-Strain Relationship of Concrete

4.6.4. Explicit Dynamic Analysis of the Model

The FE model of the bottom of RC column specimen SP1 was analyzed using the Explicit Dynamic procedure in ABAQUS, which is an efficient way of solving dynamic problems. This procedure is explicit in the sense that equilibrium equations at time $t+\Delta t$ are solved based entirely on solutions in time t using a central difference operator. Static problems can be treated quite well using Explicit Dynamic analysis provided that the inertia effects are low. Minimizing inertia effects can be achieved by either decreasing the mass density of concrete or increasing the time over which the load is applied. Unlike Static Riks (Arc-Length) method that is sensitive to parameters that define behavior of concrete and encounters convergence issues, Explicit Dynamic analysis is more robust, due to smoothing of the solutions by inertia effects, and can handle problems for which the former method fails to converge. However, the central difference operator used in Explicit Dynamic analysis is only conditionally stable. The stable time limit (Δt) for this operator is related to the time required for a dilatational wave to pass through the smallest element dimension in the model mesh. Thus, the stability limit is inversely proportional to the highest eigenvalue in the system. By default, estimation of a stable time limit and time incrementation scheme are automatically carried out in ABAQUS. The total number of increments can be estimated as $n=T/\Delta t$ where T represents total analysis time. While the number of increments is typically much larger than that needed for the Static Riks analysis, each increment is fairly inexpensive because it does not require solving a system of nonlinear equations. However, computational cost of the analysis can significantly increase by mesh refinement.

To minimize inertia effects during Explicit Dynamic analysis of the model, the loading was applied smoothly. When the analysis time is low or the time increments are large, oscillation will typically appear in the results due to inertia effects. To eliminate inertia effects, it is usually enough to set the loading time 10 to 50 times larger than the fundamental period of system (i.e. period associated with the lowest natural frequency of the system) (Mercan et al., 2010). In this analysis, the lowest frequency was estimated as 19.41 Hz resulting in a natural period of 0.052 sec. Therefore, the total analysis time was set to 2 sec. and subdivided into two equally spaced windows. During the first window, the axial load was applied and increased as a ramp function to its final value of 756 kips (3362.9 KN) at the end of the first loading window (i.e. 1 sec. from start point). The magnitude of the axial load was kept constant during the rest of the analysis. Following the first loading window, a top rotation was applied to the column whose magnitude increased as a ramp function to a final rotation of 0.05 radian at the end of the step time (i.e. 2 sec). The loading time during each window was equal to 1 sec., which is approximately 20 times the fundamental period of the system. To estimate inertia effects and evaluate accuracy of the analysis, total strain energy (E_I) and total kinetic energy (E_K) of the system were calculated. Using the above loading rate, the ratio of the kinetic energy to total strain energy (E_K / E_I) remained small (less than 0.1%) indicating that inertia effects are negligible.

4.6.5. Model Validation

The 3D model described in the previous section was analyzed using Explicit Dynamic analysis and its results were compared against test observations. The FE model could capture the incidence of in-plane buckling in the bars located on the compression face of the column (Figure 4.10). The two middle bars represent in-plane buckling towards the centerline of the column that resembles to what was observed during test of specimen SP1. These middle bars were located at the corners of the middle hoop that restrained them from in-plane buckling in the opposite direction as shown in Figure 4.2.

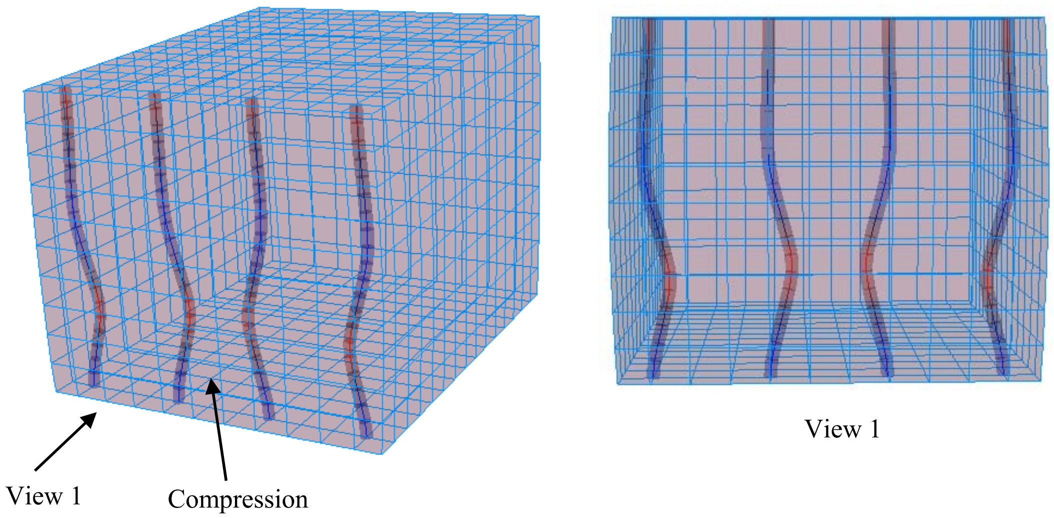

Figure 4.10. In-Plane Buckling of Bars in the FE Model

Variation of the base moment with rotation at a section located 25 in. (635 mm.) above the column base during the test is represented in Figure 4.11 and compared to the top moment in the FE model. To obtain the rotation at this section during the test, the curvature profile of the lower portion of the column was estimated based on displacement readings with the LVDTs located on the SE and NW faces of the column and at a distance equal to 12, 24, and 36 in. (305, 610, and 914 mm.) above the column base. The estimated curvature profile was integrated to get rotations at 24 and 36 in. (610 and 914 mm.), which were then interpolated to obtain the rotation at a distance of 25 in. (635 mm.) from the column base. The test specimen exhibited larger rotations at the column base due to deflection at the column-footing interface generated by bar slip of the bars within the footing, and this behavior is not captured in the FE model because it does not include representation of the

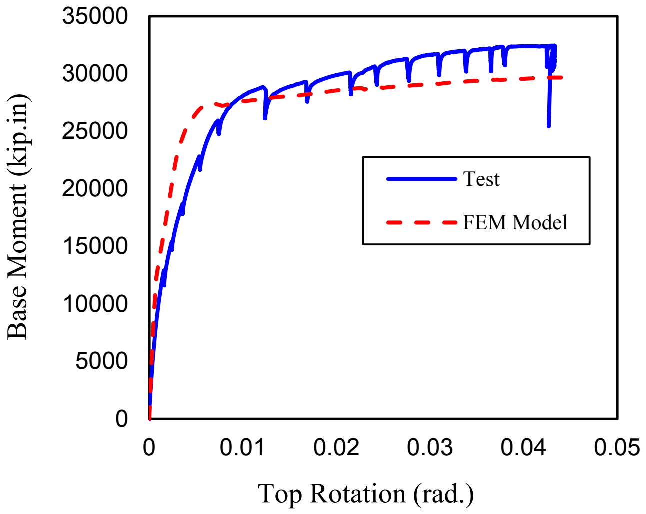

Figure 4.11. Moment-Rotation Behavior of Tested and Modeled Specimens

footing. Additionally, the model underestimates the peak strength and strain-hardening behavior of the tested specimen due to the idealization regarding spring stiffness representing the restraining effect of the concrete. In other words, the spring stiffness due to the effect of concrete surrounding the bars is estimated based on the assumption that concrete has reached its residual capacity. This limit state has been chosen to ensure that conditions for bar buckling are present during the FE analysis. The spring stiffness and thus, the amount of restraint on the bars located on the compression face of the column, is much larger at initial stages of the test and its magnitude deteriorates during loading of the specimen. An underestimation of the initial restraining effect of the concrete on reinforcing bars can lead to differences in strength and post-yield stiffness as observed in Figure 4.11. However, for the purpose of a “qualitative” study of buckling behavior of the bars located on the compression face, these differences are considered acceptable.

4.6.6. *Parametric Study*

The FE model discussed in previous section (benchmark model) was employed in a parametric study to investigate the influence of several parameters on the in-plane buckling of middle and corner bars. The parameters include concrete compressive strength, longitudinal bar size and spacing, tie spacing, and cross-sectional dimensions. A list of the models is given in Table 4.2. Maximum in-plane deformation of middle and corner bars of the benchmark model were compared to corresponding values of the other models to estimate the influence of the parameters under study.

Table 4.2. Parametric Study Matrix

Model	Parameter	b×h (in^2)	Bar Size			Tie Spacing (in.)			f'_c (ksi)			Bar Spacing (in.)		
			6	9	11	4	5	6	3.5	5	8	5.9	7.9	11.9
1	Base Model	36×28		▨			▨			▨			▨	
2	Concrete Strength			▨			▨		▨				▨	
3				▨			▨				▨		▨	
4	Bar Size				▨		▨			▨			▨	
5			▨				▨			▨			▨	
6	Bar Spacing			▨			▨			▨		▨		
7				▨			▨			▨				▨
8	Tie Spacing			▨		▨				▨			▨	
9				▨				▨		▨			▨	
10	Column Size	42×32			▨		▨			▨		9 1/4		
11		20×16	▨				▨			▨		3 15/16		

4.7. RESULTS AND OBSERVATIONS

The FE models listed in Table 4.2 were subjected to an axial load and top rotation similar to those applied to the benchmark model. For each parameter, results from three models (including the benchmark model) were compared.

4.7.1. Effect of Concrete Compressive Strength (f'_c)

Models 2 and 3 in Table 4.2 were defined with properties similar to the benchmark model except that they feature concrete compressive strengths (f'_c) of 3.5 and 8 ksi (24.1 and 55.2 MPa), respectively. The spring stiffness associated with concrete surrounding the bars (K_s) in Models 2 and 3 were calculated from Eq. 4.10 as 5.85 and 11.85 kip/in. (1.02 and 2.07 KN/mm), respectively. In-plane buckling was observed at the lower portions of middle and corner bars in both models. The maximum in-plane displacement for corner and middle bars of these two models are compared to those from the benchmark model in Figures 4.12(a) and 4.12(b). As the concrete compressive strength (f'_c) decreases, these figures reveal that initiation of in-plane buckling occurs earlier and the bars end up with larger lateral deformations. In other words, in-plane bar buckling is expected to start earlier in RC columns that are built with normal or low strength concrete due to the reduced effective stiffness associated with lower concrete strength. Moreover, an RC column with a lower f'_c is likely to undergo earlier cracking and crushing under the effect of axial and flexural loads. Therefore, assuming that the outward buckling is completely prevented by transverse hoops, the support from concrete to prevent in-plane deformation of the bars would vanish faster in these columns, which reduces the resistance to in-plane buckling of the longitudinal bars. Additionally, in-plane buckling would result in a larger deformation of longitudinal bars embedded in concrete with lower f'_c. Thus, the sudden reduction of strength due to bar fracture (from kinking of the buckled region) can occur earlier in these columns. As shown in Figure 4.13, the embedded bars in Model 3 that incorporates concrete with f'_c of 8 ksi (55.2 MPa), started to lose axial load capacity at a larger top rotation than did bars in models with f'_c of 3.5 and 5 ksi (24.1 and 34.5 MPa) (i.e., Model 2 and benchmark model, respectively).

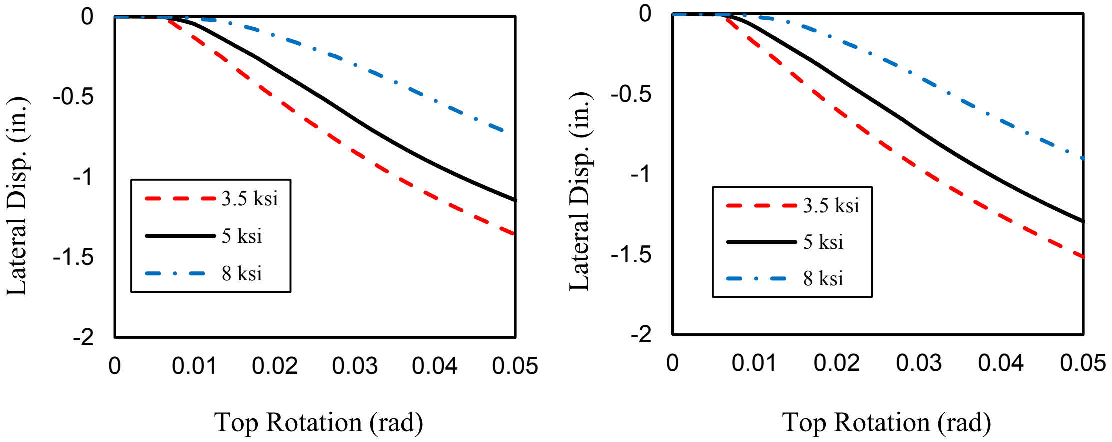

(a) (b)

Figure 4.12. Effect of Concrete Compressive Strength on Buckling Displacement in: (a) Corner Bars, (b) Middle Bars

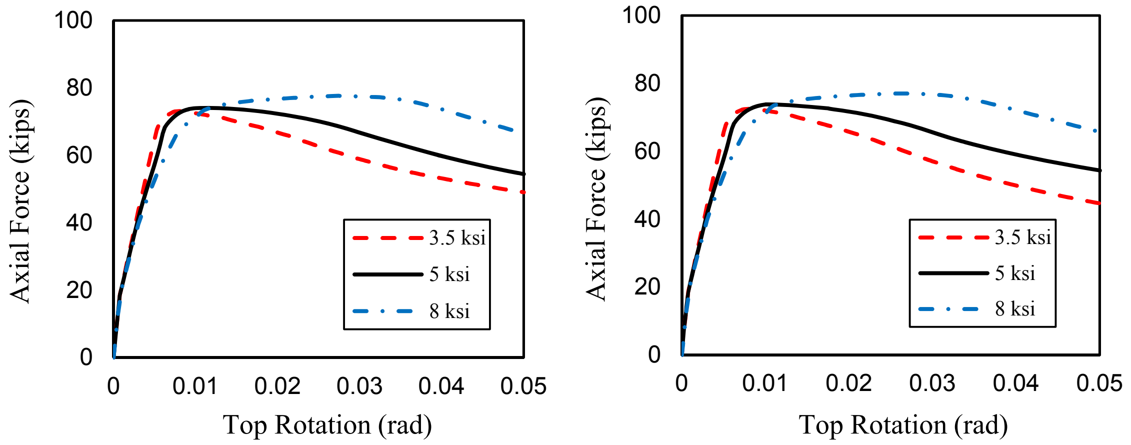

(a) (b)

Figure 4.13. Variation of Axial Loads of the Reinforcing Bars During FE Analysis in: (a) Corner Bars, (b) Middle Bars

4.7.2. Effect of Longitudinal Bar Size and Spacing

As suggested by FE analysis of simple bar-spring models, larger bar sizes require more restraining force from the surrounding concrete to resist buckling. However, as the specimen is subjected to axial and flexural loads, longitudinal bars exhibit lateral deformations leading to in-plane buckling when the concrete softens. Results from FE analysis of models with different bar sizes (Models 4 and 5) are compared with the benchmark model in Figures 4.14 and 4.15 for corner and middle bars in the compressive face. As noted in these figures, larger bar sizes (i.e. No. 11 and No. 9) experience larger final deformations in the buckling zone. Final lateral in-plane deformation for a No. 11 bar is approximately 50% larger than that for a No. 6. However, all bar sizes start to lose their axial strengths and buckle at approximately similar top rotations. Unlike bar size, the effect of longitudinal bar spacing seems to be insignificant on the in-plane buckling of the bars.

A comparison of the results from Models 6, 1 and 7 with No. 9 longitudinal bars that were spaced at 5.9, 7.9, and 11.9 in. (150, 201 and 302 mm), respectively, shows that in-plane buckling initiates at similar loading level and leads to approximately the same lateral deformations in these models. It should be noted that longitudinal bar spacing may have a role in the extent of damage and stiffness deterioration in the concrete surrounding the bars during the test. However, at a specified concrete damage state implemented in these FE models where concrete reaches its residual compressive strength, bar spacing is shown to be insignificant for in-plane buckling of the bars.

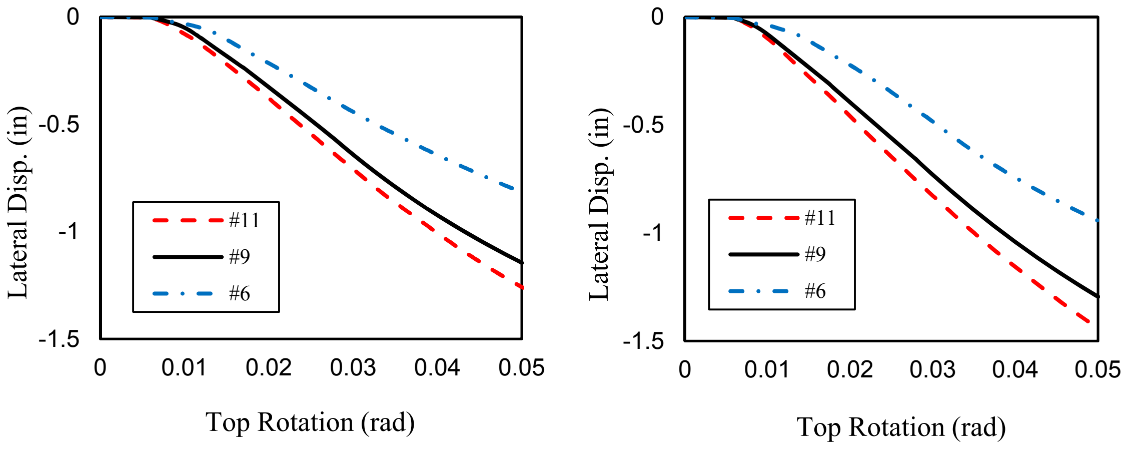

(a) (b)

Figure 4.14. Effect of Bar Size on Buckling Displacement in: (a) Corner Bars, (b) Middle Bars

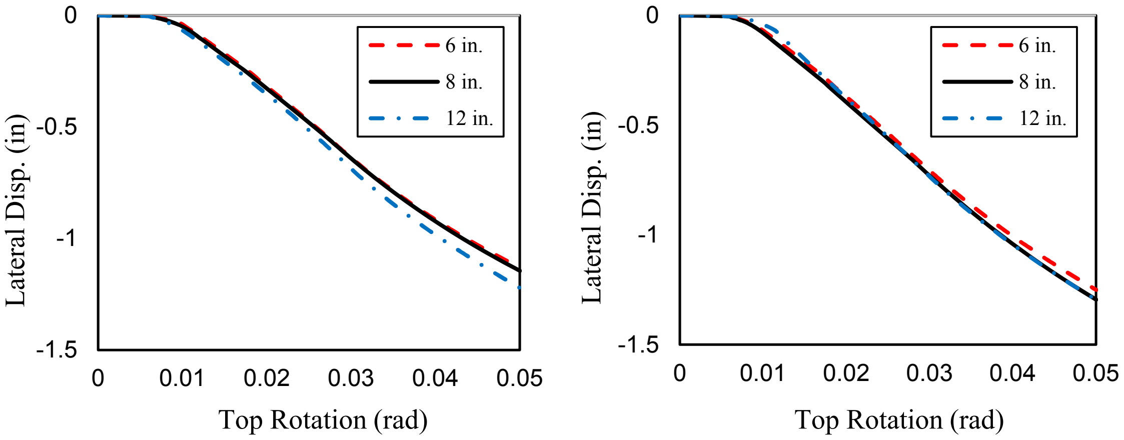

(a) (b)

Figure 4.15. Effect of Bar Spacing on Buckling Displacement in: (a) Corner Bars, (b) Middle Bars

4.7.3. Effect of Tie Spacing

While transverse ties are effective in preventing outward buckling of bars, they may also help the bars to resist in-plane buckling by enhancing concrete properties through confinement. Closely spaced transverse hoops will reduce softening rate of concrete and postpone its stiffness deterioration. Therefore, longitudinal bars in columns with closely spaced ties can resist in-plane buckling longer as the surrounding concrete that is effective in restraining them from in-plane buckling will degrade at a slower rate. However, the beneficial effect of lateral ties in limiting the in-plane buckling will disappear once the concrete crushes and loses significant amounts of strength. Three columns with transverse ties spaced at 4, 5 and 6 in. (102, 127, and 152 mm.) (Models 8, 1 and 9) which were designed in accordance with seismic provisions in ACI 318-11 (2011), are compared in Figure 4.16. As the spacing of transverse ties increase, these columns lose their axial capacity faster and undergo larger lateral deformations under the applied loads (Figure 4.16). However, these variations are minor since the concrete is considered to have degraded to its residual capacity in these FE models.

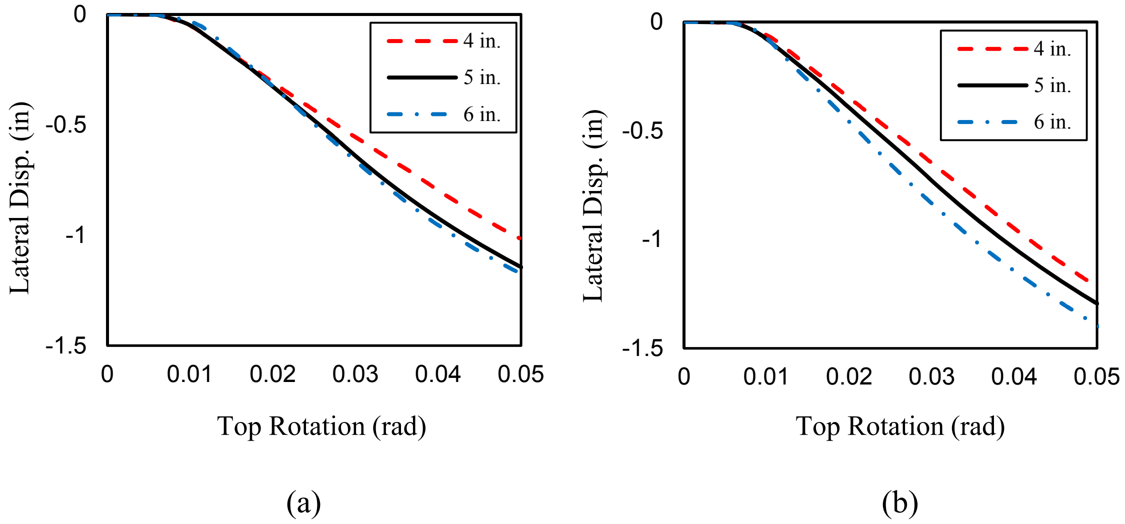

Figure 4.16. Effect of Tie Spacing on Buckling Displacement in: (a) Corner Bars, (b) Middle Bars

4.7.4. Effect of Column Cross-Sectional Size

Models 10 and 11 in Table 4.2 represent typical perimeter moment frame columns in multi-story buildings that satisfy ACI 318-11 (2011) seismic provisions. Model 10 is a column featuring a 42×32 in. (1067×813 mm) cross-sectional dimension that is built with 4 No. 11 bars spaced at 9 ¼ in. (235 mm) on the compression face (i.e., 16 No. 11 bars within the whole cross section) whereas Model 11 represents a column that is 20×16 in. (508×406 mm) in cross section and includes 4 No. 6 bars spaced at 3 $^{15}/_{16}$ in. (100 mm) on the compression side. Both columns incorporate No. 5 transverse hoops located at 5 in.

(127 mm) spacing along the columns and concrete with f'_c of 5 ksi (34.5 MPa). The axial load on the models prior to the application of top rotation was 1008, and 240 kips (4483.8 and 1067.6 KN) for models 10 and 11, respectively, which is equivalent to an axial load ratio (P/f'_cA_g) of 15%. FE analysis of these models reveals that in-plane buckling of longitudinal bars in Model 10 with larger bars embedded in a bigger cross section is more critical than in Models 1 and 11. In-plane buckling of bars in the column with a bigger cross section (i.e. Model 10) initiates earlier and these bars lose their axial load capacity faster (Figure 4.17). Therefore, larger columns incorporating larger bar sizes appear to have higher propensity to in-plane buckling than smaller columns that are constructed with similar concrete properties but which incorporate smaller bar sizes.

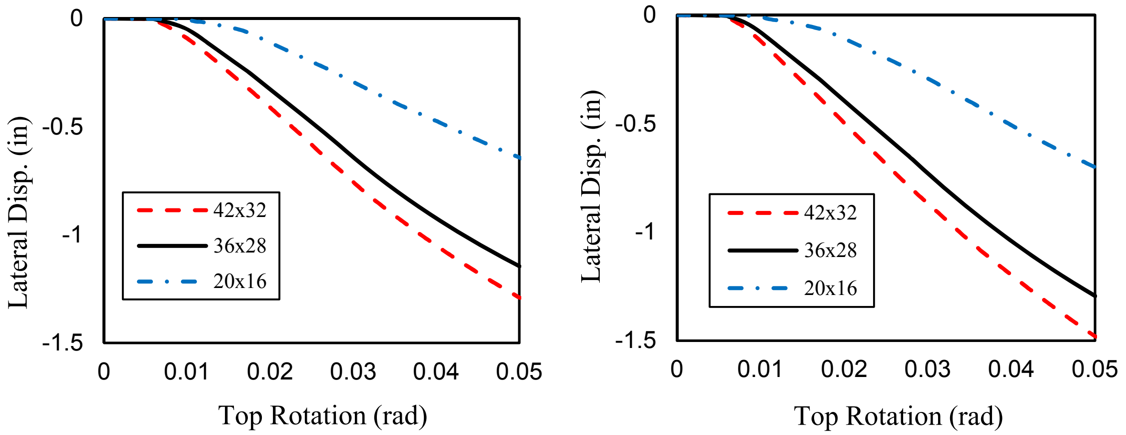

(a) (b)

Figure 4.17. Effect of Cross-Sectional Size on Buckling Displacement in: (a) Corner Bars, (b) Middle Bars

4.8. CONCLUSIONS

This paper presents results from a computational study of a failure mechanism observed during tests of seven full scale RC columns at the MAST lab subjected to a constant axial load and various lateral loading protocols. During failure, longitudinal bars were observed to buckle parallel to the face of the columns with their surrounding concrete completely crushed at the end of the tests. The loading capabilities at the MAST Lab enabled testing of full scale column specimens at larger drift ratios than those applied during previous tests under which the column specimens exhibited an unobserved mode of failure due to in-plane buckling of reinforcing bars. Since concrete is believed to be the main restraint for in-plane bar buckling, an analogy was made between the behaviors of these bars to a system of bar-spring. Analysis of the bars with linear springs at their mid-height using finite element techniques identified an upper-bound for elastic stiffness of the springs to prevent bar buckling. It was observed that the required stiffness to prevent buckling of the bars increases with bar size. Since the restraining effect of concrete degrades during the tests, elastic stiffness of springs were estimated at a stage where concrete has lost most of its compressive strength and thus the bars are prone to in-plane buckling. On the other hand, large reinforcing bars can also exert greater force on their surrounding concrete and accelerate its rate of damage. A 3D finite element model of the lower portion of the specimen subjected to monotonic loading was developed in ABAQUS/Explicit and its behavior was validated using test data. The model was then utilized to study the influence of several parameters that can affect in-plane buckling of the bars including concrete compressive strength, longitudinal bar size and spacing, tie spacing, and cross-sectional dimensions of the columns. Results from these analyses reveal that concrete with a larger f'_c helps to postpone this mode of buckling and reduces rate of axial strength loss in the bars. Additionally, larger bar sizes are recognized to be more likely to experience in-plane buckling as their restraint demands are higher. However, the effect of longitudinal bar spacing is insignificant in the stage where concrete has reached its residual capacity. At this stage, reduction of tie spacing is found to have minor beneficial effect on in-plane buckling of the bars. Finally, the specimens featuring larger cross-sectional dimensions that incorporate larger bar sizes are shown to be more critical to in-plane bar buckling. This final conclusion can be regarded as a reason for not reporting the in-plane buckling in previous tests as the columns tested at the MAST Lab were larger than almost all RC columns designed according to ACI 318 provisions.

CHAPTER 5

EFFECT OF LOADING PROTOCOLS AND ESTIMATION OF DAMAGE INDICES IN REINFORCED CONCRETE COLUMNS

5.1. SUMMARY

Seven full-scale reinforced concrete (RC) columns were tested at the Multi-Axial Subassemblage Testing (MAST) Laboratory of the University of Minnesota under distinct lateral loading protocols to large deformation demands. The loading protocols included a single cycle monotonic, uniaxial and biaxial symmetric cyclic, and a near-collapse protocols. To investigate the post-peak behavior of the specimens, loading on the specimens was continued beyond the stopping point used in most of the previous tests (i.e., 20% strength loss) until the specimens exhibited severe strength loss (i.e., approximately 80% reduction in the peak lateral load capacity) and stiffness degradation. The extent of damage during each test was estimated by nine noncumulative and cumulative damage index models. Additionally, the observed damage to the specimens during the tests was utilized to define five visual damage categories. Calculated and observed damage along with cyclic force-deformation response, energy dissipation, and stiffness reduction of the

specimens were considered to investigate the effect of the applied loading protocols. Results of the study suggest that the biaxial loading can lead to a larger extent of damage than similar protocols applied in one direction only. Also, a higher level of axial load will cause a more severe damage state under similar lateral loading protocols. Finally, when axial load ratio is similar during uniaxial tests, a combination of symmetric displacement cycles followed by a monotonic push can lead to a more detrimental damage state than purely symmetric cyclic, monotonic, or the near-collapse loading protocols.

5.2. INTRODUCTION

Structural performance of building and bridge elements can deteriorate when they are subjected to seismic events. Large cyclic load reversals during an earthquake can result in a reduction of the load-carrying capacity and stiffness of structural elements and cause varying levels of damage. The extent of damage is related to structural properties and to the characteristics of the loading history during an earthquake. In the case of an RC column, damage can be in the form of minor tension cracks, cover spalling, yielding of reinforcing bars or transverse hoops, bar buckling and fracture, and cracking and disintegration of the core concrete.

Unlike traditional design approaches, recent performance-based design philosophy anticipates the structure to dissipate energy during an earthquake and accepts certain levels of damage in structures depending on the expected risk of occurrence of earthquakes during their lifetime, and importance of the structure. Moreover, the ultimate capacity is associated with the structure reaching a near-collapse limit state. A regular building structure may be designed to experience little or no damage during minor earthquakes that occur frequently during its lifetime (i.e., immediate occupancy limit state) while certain levels of structural and nonstructural damage may be acceptable during less frequent medium earthquakes (i.e. life safety limit state). For the design earthquake or a very severe earthquake with a large return interval, even a non-repairable damage might be acceptable provided that the life-safety is not compromised (i.e., the structure does not approach the near-collapse limit state). On the other hand, accepted levels of damage during an earthquake or the design objectives often lead to larger structural demands in more important structures (e.g. hospitals, and bridges).

Structural design objectives in the performance-oriented seismic design philosophy are defined based on accepted levels of damage (i.e., limit states) under distinct levels of earthquake loads that are expected during lifetime of the structure. Estimated structural demands (e.g. required strength, or stiffness) to meet certain structural objectives are then compared against capacity of the structure (e.g. available strength, stiffness, or deformation capacity). Evaluation of structural capacity, on the other hand, relies primarily on numerical modeling tools that are calibrated against test results. In the case of RC columns, these test results are used to estimate their lateral load and deformation capacity under simulated seismic loadings.

While several tests have been conducted on RC columns, their performance, specifically in the post-peak region is not completely understood. This lack of knowledge in the softening regime of response for columns is mainly due to the fact that almost all of the previous tests were terminated once specimens lost no more than approximately 20% of their lateral load capacity. While an arbitrary definition of structural failure can be tied to the aforementioned condition, RC columns can still survive collapse when loaded well beyond this arbitrary point of failure. Therefore, a series of tests is needed to enhance knowledge on softening behavior of RC columns when they lose most of their lateral load capacity. Such an understanding is essential, especially for defining seismic collapse safety limit states of RC columns in performance-based design.

Unlike RC bridge columns, there are limited previous experimental efforts that have focused primarily on the effects of applied loading protocols on RC building columns and during which similar test specimens were subjected to monotonic and cyclic loading protocols. Considering the uncertainty in the amplitude and number of cycles that RC columns in a building structure may sustain during an earthquake, their performance under distinct simulated loading protocols will be beneficial in the estimation of their force-deformation backbone capacity curves and characterization of damage during various stages of loading.

Damage characterization is also an essential element for designing new structures based on performance-oriented design as well as for initial assessment and retrofit decision making after seismic events. The extent of expected damage is used to define different limit states in performance-based design and to set structural objectives accordingly. These limit states for building structures can be defined as experiencing minor or cosmetic damage during frequent earthquakes or just remaining stable during catastrophic seismic actions.

In both cases, the limit states are related to the level of anticipated damage. Once a structure experiences a seismic event, identification of the extent of observed damage will be essential in the estimation of repairability of the structure and in preparation of retrofit plans.

The state of damage in structures is often quantified by damage indices that are usually scaled to be zero in the case of an undamaged structure, and unity in the case of collapse. The incidence of collapse in structural elements is usually defined arbitrarily as a state of loading under which the structural element loses a certain amount of its load carrying capacity, typically 20% of the peak capacity. Several damage indices have been proposed to quantify the extent of physical deterioration in structures and their residual capacity. Most of the existing damage measures are described in terms of lateral deformation (i.e. displacement, rotation, or curvature), stiffness, hysteretic energy, fatigue or a combination of these parameters. However, application of different measures often leads to differing results which makes recognition of the actual state of structural damage challenging.

In this paper, the effect of distinct loading protocols including monotonic, uniaxial and biaxial symmetric cyclic, and a near-collapse protocol developed for this experimental program on the performance of full scale RC columns is investigated. During these tests, the column specimens were loaded beyond the common stopping point in previous tests until they significantly lost their lateral load capacity and exhibited severe deterioration. Observed damage during tests of the specimens is used to define damage categories and to assess various damage index models. Observed and calculated damage values are then used to study the effects of different lateral loading protocols.

5.3. PREVIOUS WORK ON DAMAGE INDICES

Several damage index models have been proposed to quantify the state of physical deterioration and strength loss in structures under various loading conditions. Damage indices are usually described locally, in the element level or globally, for the entire structure. Member deformation (e.g. lateral displacement, rotation, or curvature), stiffness, hysteretic dissipated energy, fatigue behavior, or a combination of these parameters are typically used in expressing local measures of damage whereas global indices are often calculated by weighted summation of damage in their components. Given that the specimens in this experimental program represented the lower portion of the first-story columns in a prototype RC moment frame, only local measures of damage are considered here. The state of damage during loading depends on both the amplitude of the applied load and the number of cycles. While noncumulative damage indices ignore the effect of cycling, cumulative damage indices take the effect of both magnitude and number of cycles into account usually by summation over all preceding cycles during a loading history. A summary of the well-known damage index models is presented in the following section. A comprehensive description of local and global damage indices is also presented by Chung et al. (1987) and Williams and Sexsmith (1995).

5.3.1. *Noncumulative damage indices*

Perhaps the simplest measure to quantify damage in RC members are the ones described in terms of ductility. Damage indices in terms of rotation and curvature ductility were proposed by Banon et al. (Banon, Irvine, & Biggs, 1981):

$$\mu_\theta = \frac{\theta_{\max}}{\theta_y} = 1 + \frac{\theta_{\max} - \theta_y}{\theta_y} \tag{5.1}$$

$$\mu_\phi = \frac{\phi_{\max}}{\phi_y} = 1 + \frac{\phi_{\max} - \phi_y}{\phi_y} \tag{5.2}$$

where θ_{max} and θ_y represent maximum and yield rotations, respectively and ϕ_{max} and ϕ_y are the corresponding curvatures. Banon (1980) also proposed a ductility definition based on plastic rotation (θ_p), however he noted that θ_p may not increase as rapidly as the progression of damage in the structural member, thus he suggested using the ductility based measures in Eqs. 5.1 and 5.2. A similar equation can be expressed for lateral displacement ductility as follows:

$$\mu_\Delta = \frac{\Delta_{\max}}{\Delta_y} = 1 + \frac{\Delta_{\max} - \Delta_y}{\Delta_y} \tag{5.3}$$

where Δ_{max} and Δ_{y} correspond to the peak displacement and displacement at yield, respectively. While its simplicity is appealing, damage indices based on ductility introduce some disadvantages. Calculated ductility terms based on Eqs. 5.1 and 5.2 are not scaled to be zero for the undamaged members and one at their collapse state. Also, these damage indices are affected by the magnitude of the yield deformation in the RC member which can be defined based on the measured first yield in the system, an assumed equivalent elastoplastic behavior or an elastoplastic energy absorption for the member, or a reduced (secant) stiffness on an equivalent elastoplastic member response (R. Park, 1989). Considering that rotations can occur due to shear deformation and bar slip, Banon et al. (1981) indicated that an analytical estimation of the yield rotation assuming antisymmetric bending and elastic stiffness tends to underestimate the true yield rotation and results in rotation ductilities that are larger than experimental ones. Even if the yield deformations are calculated correctly, two specimens with identical lateral force and deformation capacity but different stiffness will exhibit significant differences in the calculated displacement ductilities (μ_{Δ}).

Lybas and Sozen (1977) proposed a damage index based on the ratio of the initial tangent stiffness (K_o) to the reduced (secant) stiffness at maximum displacement of the current cycle (K_m):

$$DR = \frac{K_o}{K_m} \tag{5.4}$$

The advantage of the above equation as compared to the ductility expressions is its lack of dependency on yield displacement. However, analytical estimation of initial tangent stiffness (K_o) may be difficult due to the presence of the shear deformation and bar slip. Therefore, Banon et al. (1981) proposed replacing K_o with calculated stiffness of the cracked member (K_{cr}) and modified Eq. 5.4 to obtain the flexural damage ratio (FDR) as follows:

$$FDR = \frac{K_{cr}}{K_m} \tag{5.5}$$

where $K_{cr} = 24EI/L^3$ in the case of antisymmetric bending, in which E = elastic modulus of elasticity, I = moment of inertia, and L = member length. FDR seems to be a better indicator of damage in the specimen compared to ductility terms as it takes the effects of strength reduction and stiffness deterioration into account and is not sensitive to the displacement at yield. However, $24EI/L^3$ does not represent a valid estimation for K_{cr} of a first-story column since the top of the column is likely to rotate even if the rotation at the column base is very small due to a very stiff foundation (which is not always the case).

Roufaiel and Meyer (1987) included secant stiffness corresponding to the failure (K_f) and modified the flexural damage ratio as follows:

$$FDR^+ = \frac{K_m^+ - K_o^+}{K_f^+ - K_o^+} \tag{5.6}$$

where the positive signs (+) denote the loading direction. A similar equation is expressed for loading in the opposite direction and the flexural damage ratio is taken as the maximum of the calculated values in positive and negative directions. Assuming a bilinear moment-curvature response for the member, K_o will be equivalent to the secant stiffness at yielding.

5.3.2. Cumulative damage indices

The state of damage in RC members depends not only on the magnitude of the applied loads, but also on the number of cycles they sustain. Repeated loading at large deformations will result in the accumulation of plastic damage in the RC member and expedites strength loss and stiffness deterioration due to the phenomenon known as low cycle fatigue. Therefore, cumulative damage indices that include the effect of damage accumulation in the preceding cycles have been proposed. Cumulative damage indices are typically expressed in terms of accumulation of plastic deformation or strain in a form of low cycle fatigue formulation, reduction of stiffness, normalized dissipated energy, or a combination of these parameters.

5.3.2.1. Deformation- and Strain-based cumulative damage indices

To take the effect of cycling into account, Banon et al. (1981) attempted to extend his proposed equation for rotation ductility (Eq. 5.1) and introduced normalized cumulative rotation term:

$$NCR = \frac{\sum \left| \theta_{\max} - \theta_y \right|}{\theta_y} \tag{5.7}$$

A similar form can be expressed in terms of cumulative displacement:

$$NCD = \frac{\sum \left| \Delta_{\max} - \Delta_y \right|}{\Delta_y} \tag{5.8}$$

While NCR can represent damage due to cumulative fatigue-type loading, Banon et al. (1981) observed a large scatter in the results at the state of specimen failure.

Stephens and Yao (1987) modified the equation which was previously proposed by Yao & Munse (1962) for steel structures and expressed a damage index that accounts for the accumulation of plastic deformations due to cyclic loading on RC structural elements:

$$D = \sum_{i=1}^{n} D_i \tag{5.9}$$

where D is the damage due to n cycles and:

$$D_i = \left(\frac{\Delta\delta_{pi}^{+}}{\Delta\delta_{f}} \right)^{1-br} \tag{5.10}$$

where D_i = damage associated with the i^{th} cycle, $\Delta\delta_{pi}^{+}$ = incremental positive plastic deformation of the i^{th} cycle (Figure 5.1), $\Delta\delta_f$ = the value of $\Delta\delta_{pi}^{+}$ single cycle test resulting in the specimen failure, b is recommended as 0.77, and r is ratio of the plastic deformation in the positive direction ($\Delta\delta_{pi}^{+}$) to that in the negative direction ($\Delta\delta_{pi}^{-}$) during i^{th} cycle described as:

$$r = \frac{\Delta\delta_{pi}^{+}}{\Delta\delta_{pi}^{-}} \tag{5.11}$$

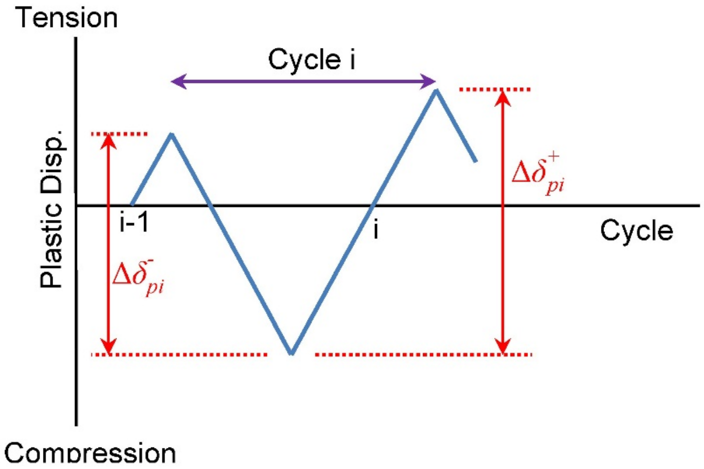

Figure 5.1. Definition of Plastic Deformations in Stephens-Yao Model

While the damage index based on Stephens's model includes the effect of loading reversals, it ignores the effect of sequence of cycles that can affect the extent of damage. Additionally, when results from monotonic tests are not available, an estimation of $\Delta\delta_f$ depends on the selection of the drift ratio at which failure is expected to occur.

Wang and Shah (1987) developed a cumulative displacement based damage model in an exponential form assuming that the rate of damage accumulation is proportional to the existing state of damage in the structure:

$$D = \frac{e^{sD_i} - 1}{e^{s} - 1} \tag{5.12}$$

where

$$D_i = c\sum_i \frac{\Delta_i}{\Delta_f} \tag{5.13}$$

where Δ_i = maximum imposed displacement in the i^{th} cycle, and Δ_f = displacement capacity under monotonic loading. A value of 0.1 was recommended by Wang and Shah (1987) for c while they suggested taking s equal to 1.0 for a well reinforced beam-column joint and -1.0 for a poorly reinforced joint that is prone to shear failure.

RC members are likely to sustain large displacement reversals during an earthquake that causes large plastic strains to be accumulated over cycles and eventually result in the member failure. Jeong and Iwan (1988) assumed a prescribed relationship for a member that fails due to application of N_f cycles of loading at a given displacement ductility, μ:

$$N_f \mu^s = C \tag{5.14}$$

where s and C are positive empirical constants and are suggested to be taken as 6 and 416, respectively. Their proposed equation is similar to the classical Coffin (1954)-Manson (1953) relationship for low-cycle fatigue failure in which the number of cycles leading to collapse is related to the accumulated plastic strains. Assuming that damage accumulation is a linear function of the number of cycles with a constant amplitude (n_i) and using the simple rule proposed by Palmgren (1924) and Miner (1945), Jeong and Iwan (1988) expressed the damage index as:

$$D = \sum_i \frac{n_i}{N_{fi}} = \frac{1}{C} \sum_i n_i \mu_i^s \tag{5.15}$$

where n_i = number of cycles at the i^{th} cycle, N_{fi} = number of cycles that cause collapse at the i^{th} cycle, and μ_i = displacement ductility corresponding to the i^{th} cycle. A damage index of 1 corresponds to failure. Their proposed damage index does not account for the effect of loading sequence, however considering its simplicity, it can provide a qualitative estimate of damage in an RC member.

More sophisticated fatigue-based damage indices have also been proposed in which the number of cycles that cause collapse is related to the plastic or total strains in the reinforcing bars. By conducting tests on reinforcing bars, Mander et al. (1994) related the fatigue life of reinforcing bars to their plastic strains as a classical form of Coffin (1954)-Manson (1953)relationship:

$$\varepsilon_p = 0.08(2N_f)^{-0.5} \tag{5.16}$$

where ϵ_p = plastic strain in the reinforcing bars, and N_f = number of cycles causing collapse. Since estimation of plastic strains can be difficult due to the Bauschinger's effect, a similar form of this equation was also proposed based on the total strain (Mander & Cheng, 1995):

$$\varepsilon_t = 0.08(2N_f)^{-0.333} \tag{5.17}$$

The damage index is calculated using Miner's rule (1945):

$$DI = \sum_i \frac{1}{2N_{fi}} \tag{5.18}$$

where N_{fi} = number of cycles causing collapse at the i^{th} cycle.

Kunnath et al. (1997) correlated Eqs. 5.16 and 5.17 to the results from their tests on bridge piers under constant-amplitude loading:

$$\varepsilon_p = 0.065(N_{2f})^{-0.436} \tag{5.19}$$

$$\varepsilon_t = 0.06(N_{2f})^{-0.360} \tag{5.20}$$

where N_{2f}=number of cycles to failure. Kunnath et al. (1997) indicated that their proposed modified equations are more suitable than those derived by Mander an Cheng (1995) for RC sections as they consider the actual fatigue behavior of reinforcing bars in a RC section and include damage due to shear and axial stresses as well as loss of confinement. However, their model could not predict failure in two out of five specimens under cyclic displacement reversals and in any of the six column specimens under random earthquake excitations. During their tests, Kunnath et al. (1997) also observed that under low amplitude displacement cycles, failure is generally controlled by loss of lateral support than low cycle fatigue of reinforcing bars. Therefore, they suggested that a model that includes damage corresponding to confinement deterioration as well as low cycle fatigue would be better suited for RC columns.

To include the effect of lateral restraint provided by cover concrete on the performance of longitudinal bars, Lehman and Moehle (2000) developed a two-phase damage model based on the Coffin (1954)-Manson (1953). The first phase in their proposed model considers the damage in the cover concrete whereas the second phase includes low cycle fatigue failure in reinforcing bars. The damage index in each phase is defined based on

Miner's rule. Before cover spalling, the damage index is only related to the state of strain in cover concrete. Once, the cover concrete is completely failed (i.e., $D_c=1$), damage index will be represented by fatigue of longitudinal bars.

$$(N_f)_c = 33(\frac{\varepsilon_c}{\varepsilon_{csp}})^{-5} \tag{5.21}$$

$$(N_f)_s = 0.08(\frac{\varepsilon_s}{\varepsilon_{su}})^{-5.5} + 0.92 \tag{5.22}$$

$$D_c = \sum_i \frac{1}{(N_f)_{ci}} \qquad \text{for } D_c \le 1 \tag{5.23}$$

$$D_s = \sum_i \frac{1}{(N_f)_{si}} \qquad \text{for } D_c = 1 \tag{5.24}$$

where

$(N_f)_c$ = number of cycles to degrade cover concrete

$(N_f)_s$ = number of cycles to failure after cover spalling

ϵ_c = compressive strain in the extreme fiber of core concrete

ϵ_{csp} = compressive strain at cover spalling

ϵ_s = tensile strain of the longitudinal bar

ϵ_{su} = ultimate tensile strain in the extreme longitudinal bar

D_c = damage corresponding to cover spalling

D_s = damage corresponding to low cycle fatigue in the reinforcing bars after cover spalling

ϵ_{csp} and ϵ_{su} were estimated based on experimental results whereas ϵ_c and ϵ_s were predicted analytically. The two-phase damage index could predict failure in 5 out of 6 column specimens tested by the authors and all of the columns tested by Kunnath et al. (1997).

Through finite element (FE) analysis of RC columns, Erduran and Yakut (2004) introduced three categories of damage based on the maximum crack width that is caused by loading of the specimens. The crack width was calculated based on measured tensile strains of longitudinal reinforcing bars according to the equation proposed by Frosch (1999). The maximum calculated crack widths of 0.2, 1, and 2 mm (0.008, 0.039, 0.079 in.) were selected to define three states of damage as negligible, light, and moderate and were assigned damage scores of 0.5%, 7.5%, and 30%. The fourth (i.e., heavy) damage state was related to the ultimate ductility capacity and was assigned a damage score of 90%. The ultimate ductility capacity of columns were calculated based on a normalized parameter $\rho_s / (P/P_o)$ in which ρ_s represents the volumetric ratio of transverse reinforcement and P/P_o denotes the ratio of the applied axial load to the axial load capacity (P/P_o). The authors had shown formerly that the normalized parameter $\rho_s / (P/P_o)$ significantly affects the ductility of RC columns.

Based on the observed relationship between the drift ratio and damage scores in each ductility category, Erduran (Erduran & Yakut, 2004) proposed an equation for the damage state at a target drift ratio (δ):

$$D(\delta) = f(\delta)g(\delta) \tag{5.25}$$

where $f(\delta)$ and $g(\delta)$are defined as:

$$f(\delta) = 1 - \frac{1}{\exp(\frac{\delta}{aC_s C_{fy}})^b} \tag{5.26}$$

$$g(\delta) = 0.5\left[1 - \cos(\frac{\pi\delta}{cC_s C_{fy}})\right] \qquad \text{if} \qquad \frac{\delta}{C_s C_{fy}} \le c \tag{5.27}$$

$$g(\delta) = 1 \qquad \text{if} \qquad \frac{\delta}{C_s C_{fy}} > c \tag{5.28}$$

where a,b ,and c are constants that depend on the ductility levels (i.e. magnitude of $\rho_s /(P/P_o)$) and C_s and C_{fy} are correction factors for yield strength of longitudinal bars and slenderness, respectively.

While their proposed damage index showed high correlation with damage curves in ATC-40 (1996), it involves several arbitrary constant values and damage scores. Also, three out of four of the defined damage categories (i.e., negligible, low, and moderate) rely only on crack widths and hence invalid once cover spalling occurs. Their proposed equation for determination of the fourth (i.e., heavy) damage state which is based entirely on the calculation of the ultimate ductility is noncumulative and ignores the effects of low cycle fatigue and loading history. Therefore, while their proposed equation might be useful for design practices, its ability to provide an estimation of the damage state in RC columns under large cyclic load reversals is questionable.

5.3.2.2. Energy-based cumulative damage indices

Dissipated energy during loading has also been used as a measure for state of damage in RC members by researchers. Gosain et al. (1977) proposed a work index (I_w) to estimate damage in RC beams and columns with dominant failure mode in shear:

$$I_w = \sum_{i=1}^{n} \frac{p_i \Delta_i}{p_y \Delta_y} \tag{5.29}$$

where

n=number of cycles in which $p/p_y \geq 0.75$

p_i, Δ_i= lateral load at peak displacement and corresponding peak displacement during the i^{th} cycle

p_y, Δ_y= lateral load and corresponding displacement at yielding of reinforcing bars

Only cycles satisfying lateral load ratios with $p/p_y \geq 0.75$ were considered. As the upper bound p/p_y was estimated as 1.25, the authors also suggested simplification of the work index as the summation of normalized deflections (i.e., Δ_i/Δ_y). As also indicated by the authors, the proposed work index for a specimen that is loaded two times to a normalized deflection of 10 would be equal to that for a specimen that is loaded four times to a normalized deflection of 5 while the former would likely experience more damage. Thus, the damage index as proposed in Eq. 5.29 did not correlate well with the experimental database that the authors used. Therefore, they proposed modifications to account for the effect of shear span and axial load.

A more sophisticated cumulative energy index was developed by Kratzig and Meskouris (1987). In their proposed method, dissipated energy terms were calculated separately for the primary half-cycles (PHCs) and follower half-cycles (FHCs) in the positive and negative directions (Figure 5.2). A PHC was defined as the half cycle with a displacement larger than that in the previous cycles whereas a FHC was considered as any following half cycles of equal or smaller deformation amplitudes. For the positive deformation of the specimen, the accumulated damage is defined as:

$$D^{+} = \frac{\sum E_{pi}^{+} + \sum E_{i}^{+}}{E_{f}^{+} + \sum E_{i}^{+}} \tag{5.30}$$

where

E_{pi}^{+} = energy in a PHC with a positive deformation amplitude

E_{i}^{+} = energy in a FHC with a positive deformation amplitude

E_{f}^{+} = energy in a monotonic test to failure for loading in the positive direction

Accumulated damage during negative deformation part is calculated in a similar approach and yields the overall damage as:

$$D = D^{+} + D^{-} - D^{+}D^{-} \tag{5.31}$$

Their proposed model includes both the damage due to large displacement excursions as well as the fatigue-type damage due to repeated loading at smaller displacement amplitudes. Calculated damage indices could properly predict failure for nine beams in their study.

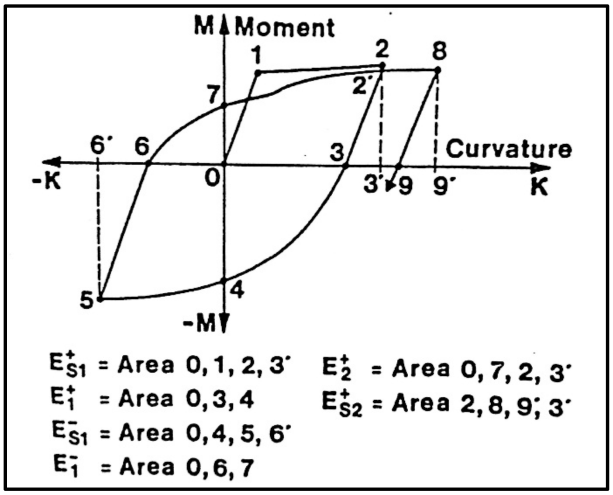

Figure 5.2. Definition of Primary and Follower Half Cycles (Kratzig & Meskouris, 1987)

5.3.2.3. Combined cumulative damage indices

A popular damage index was developed by Park and Ang (1985) assuming a linear combination of normalized displacement to characterize noncumulative effects and normalized dissipated energy to characterize cyclic loading effects:

$$D = \frac{\Delta_m}{\Delta_u} + \beta \frac{\int dE}{F_y \Delta_u} \tag{5.32}$$

where

Δ_m = maximum displacement

Δ_u = ultimate displacement capacity under monotonic loading

F_y = yield strength

dE= dissipated energy increment

β = strength deterioration factor due to cyclic loading

By regression analysis of 261 tests on RC beams and columns, Park and Ang (1985) proposed an equation to estimate β :

$$\beta = (-0.447 + 0.073\frac{l}{d} + 0.24\frac{P}{f_c'bd} + 0.31\rho_l)0.7^{\rho_s} \tag{5.33}$$

where

l = length of specimen

d = distance from extreme compression fiber to the centroid of the longitudinal tension reinforcement

l/d = shear span ratio, replaced by 1.7 if $l/d < 1.7$

$P/f'_c bd$ = normalized axial stress, replaced by 0.2 if $P/f'_c bd < 0.2$

ρ_l = longitudinal reinforcement ratio (%), replaced by 0.75 if $\rho_l < 0.75$

ρ_s = confinement reinforcement ratio (%).

The authors subsequently proposed a damage classification based on observed data as represented in Table 5.1 (Park, Ang, & Wen, 1987). Williams and Sexsmith (1995) indicated difficulties in the estimation of ultimate displacement capacity (Δ_u) and strength deterioration factor (β). They also criticized the damage scale for being nonlinear with the severe damage state corresponding to the calculated damage index of magnitudes beyond 0.4.

Kunnath et al. (1992) proposed an alternative form of Park-Ang (1985) damage index based on moment and curvature instead of load and displacement which was later used by Stone and Taylor (1993) for investigation of the damage state in circular bridge piers. However, Stone and Taylor (1993) indicated that for the case of simple structures such as cantilever bridge piers, the results using moments and curvature were similar to those obtained by using the force and displacement in the original Park-Ang (1985) equation.

Assuming a damage index equal to unity at ultimate displacement capacity, Eq. 5.32 can be written as:

$$1 = \frac{\Delta_m}{\Delta_u} + \beta \frac{E_h}{F_y \Delta_u} \tag{5.34}$$

where E_h= dissipated energy during loading. Under collapse condition due to monotonic loading (i.e., when $\Delta_m = \Delta_u$), Eq. 5.34 results in the total dissipated energy to be zero. However, during monotonic loading to failure, the specimen will exhibit inelastic behavior and dissipate energy. To correct the issue, Chai et al. (1995) suggested removing the plastic strain energy due to monotonic loading.

Table 5.1. Damage Classification for Park-Ang Model

Index Value (D)	Damage Category	Description of the Observed Damage
$D < 0.1$	Slight	localized cracking
$0.1 \leq D < 0.25$	Minor	minor cracking throughout, partial crushing of concrete in columns
$0.25 \leq D < 0.4$	Moderate	extensive cracking, localized spalling
$0.4 \leq D < 1$	Severe	extensive crushing of concrete, disclosure of reinforcing bars
$D \geq 1$	Collapse	Collapse

5.4. EXPERIMENTAL PROGRAM

Seven full-scale RC columns were tested as part of this research. All specimens except SP5 featured a 36×28 in. cross section with 16 No. 9 longitudinal bars and transverse hoops made of No. 5 bars and spaced at 5 in. along the height of the specimens. Specimen SP5 featured a smaller cross section (28×28 in) and incorporated 12 No.8 reinforcing bars which were confined by transverse hoops at 5 in. spacing. The columns were subjected to distinct lateral loading protocols as summarized in Table 5.2.

Each test started by application of an axial load. The magnitude of the applied axial loads was set to 756 and 1176 kips, equivalent to an axial load ratio (P/f'_cA_g) of 0.15 and 0.3 for larger (i.e. 36×28 in.) and smaller (i.e. 28×28 in.) columns, respectively. While keeping the axial load level constant, the specimens were subjected to lateral loading protocols in the form of displacement excursions as represented in Figures 5.3 to 5.9.

Application of the lateral loadings on specimens continued until either the actuators reached their stroke capacity or the specimens lost more than 80% of their peak lateral load capacity in either direction.

The first specimen was subjected to a monotonic displacement until the stroke capacity of the actuators exhausted at 15.61 in. of the crosshead displacement. To estimate the reserve capacity of the specimen, the monotonic loading in the positive direction was then followed by loading in the opposite direction and formed a single cycle (Figure 5.3). The specimen response during the first test was utilized to estimate the peak deformation capacity of the columns and to calibrate controllers of the loading crosshead at the MAST Lab.

The loading protocol on specimens SP2 and SP5 were designed following the procedures in the ACI 374-05 (2005). These loading protocols incorporated a series of progressively increasing displacement cycles. The magnitudes of displacement cycles were gradually increased with an approximate growth of 25% to 50 % in the drift ratio (Figures 5.4 and 5.7). Three cycles were applied in each drift level and were followed by a small cycle at a magnitude equal to one third of that in the preceding cycle group. Initial cycles were set to drift ratios within the linear elastic behavior of the specimens. Cyclic displacement reversals on specimens SP2 and SP5 followed the aforementioned pattern until these specimens significantly lost their peak lateral load capacity. These tests stopped after 56 and 52 cycles and following the application of cycles at 8.91% and 7.13% drift ratios for specimens SP2 and SP5, respectively.

Table 5.2. Applied Lateral Loading to the Specimens

Specimen	Description of Loading Protocol	Loading Direction	δ_y (%)	δ_{Fmax} (%)	δ_{ult} (%)	F_y (kips)	F_{max} (kips)	F_{ult} (kips)	F_{ult} / F_{max}
SP1	Monotonic	Pos	0.80	3.10	12.09	238	290	212	0.73
		Neg		-4.00	-11.43		-239	-172	0.72
SP2	Symmetric cyclic (ACI 374)	Pos	0.65	1.07	6.91	258	314	58	0.19
		Neg	-0.70	-1.09	-6.91	-235	-278	-53	0.19
SP3	Symmetric cyclic (ACI 374)+monotonic push	Pos	0.76	2.29	11.63	246	297	222	0.75
		Neg	-0.74	-3.51	-10.84	-235	-278	-64	0.23
SP4	Symmetric cyclic (ACI 374)+monotonic push	Pos	0.75	4.74	11.63	257	310	61	0.20
		Neg	-0.76	-1.51	-10.85	-241	-288	-21	0.07
SP5	Symmetric cyclic (ACI 374)	Pos	0.52	1.51	5.53	155	192	53	0.27
		Neg	-0.60	-1.08	-5.53	-137	-168	1	-0.01
SP6	Near-collapse	Pos	0.90	3.44	10.43	232	280	52	0.19
		Neg	-0.71	-1.09	-11.62	-214	-257	-198	0.77
SP7	Biaxial	Pos	0.91	3.52	5.53	227	279	57	0.21
		Neg	-0.98	-3.52	-5.53	-218	-268	-33	0.12

Specimens SP3 and SP4 initially sustained displacement cycles that were designed according to the same pattern as of those described for specimens SP2 and SP5. However, these cycles were followed by monotonic push in positive and negative displacement directions after applications of 5.67% and 3.66% drift cycles for specimens SP3 and SP4, respectively (Figures 5.5 and 5.6). Unlike all other specimens, the loading protocol on specimen SP6, the near-collapse protocol, incorporated symmetric and asymmetric cycles followed by a final monotonic displacement push (Figure 5.8). The near-collapse loading protocol was developed from time history analysis on low- and high-rise buildings subjected to far-field earthquake motions.

The biaxial loading protocol on specimen SP7 was designed based primarily on the same pattern as of that for SP2, but along both X and Y directions. Each full cycle in this loading protocol can be represented by load paths A and B as noted in Figure 5.9(a) and Figure 5.9(b) to form a full cycle at a target drift level (Figure 5.9(c)). The lateral loading on the specimen started by application of a displacement along the positive Y direction similar to that initially applied to specimen SP2. The specimen was then subjected to the target displacement along X direction while it was unloaded along Y direction. The resulted applied displacements along negative X and Y directions completed a full cycle at a desired drift level. The aforementioned pattern continued to create gradually increasing displacements along both directions. Loading of the specimen terminated after 52 full cycles and following the application of 7.13% drift cycles (Figure 5.9(d)).

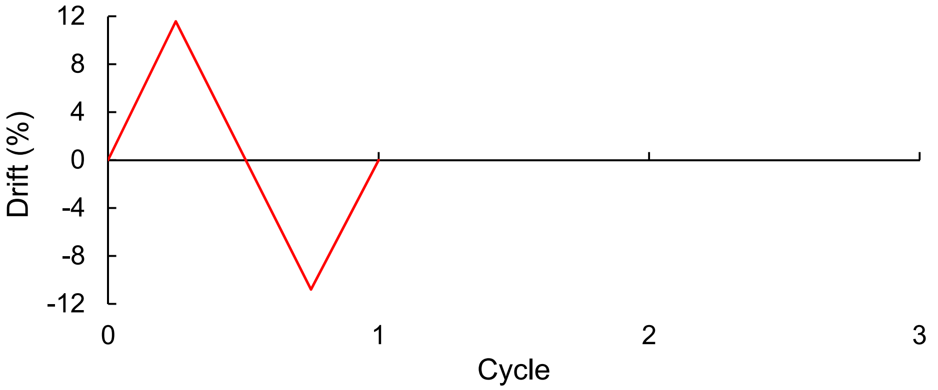

Figure 5.3. Applied Loading Protocol to Specimen SP1

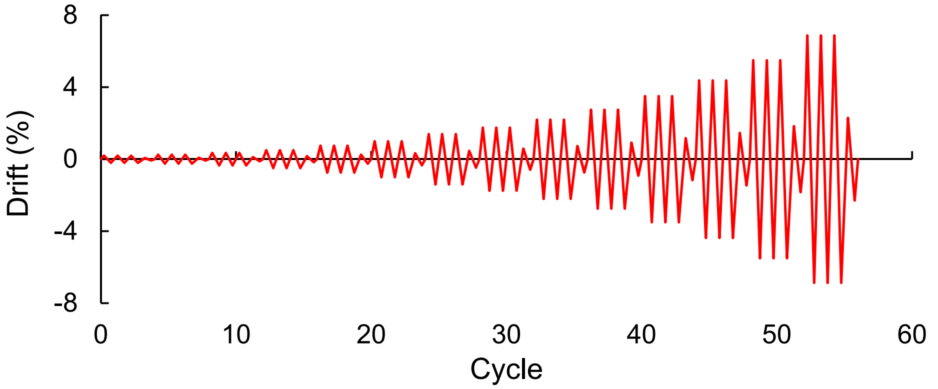

Figure 5.4. Applied Loading Protocol to Specimen SP2

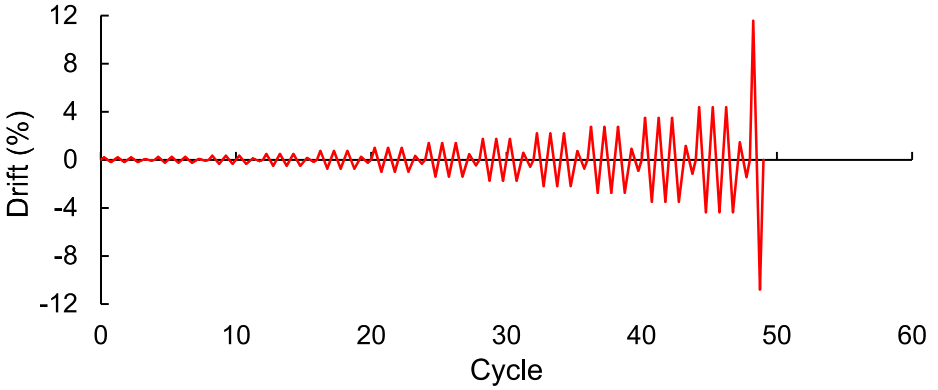

Figure 5.5. Applied Loading Protocol to Specimen SP3

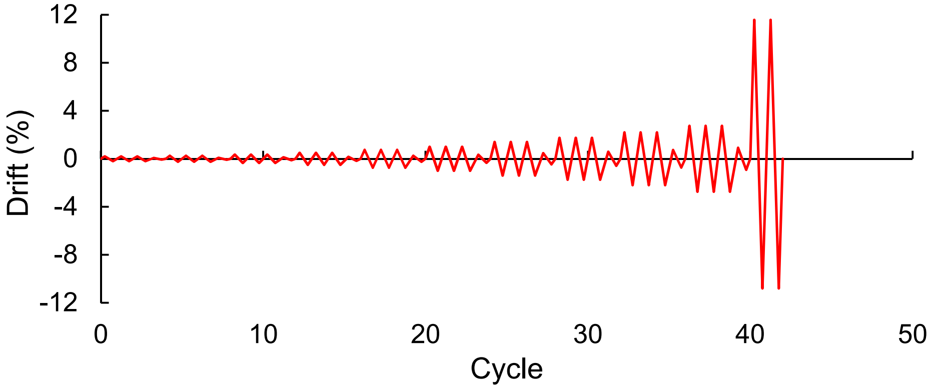

Figure 5.6. Applied Loading Protocol to Specimen SP4

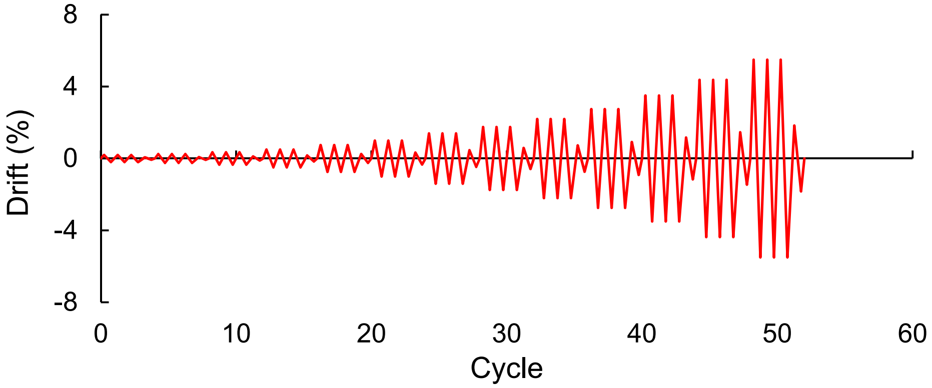

Figure 5.7. Applied Loading Protocol to Specimen SP5

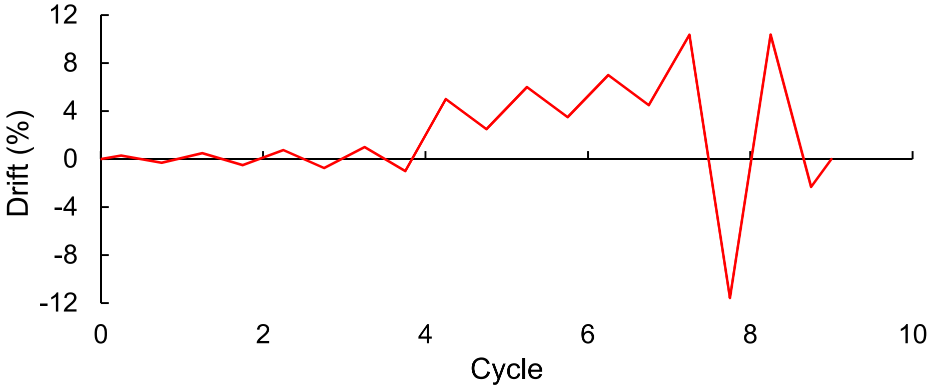

Figure 5.8. Applied Loading Protocol to Specimen SP6

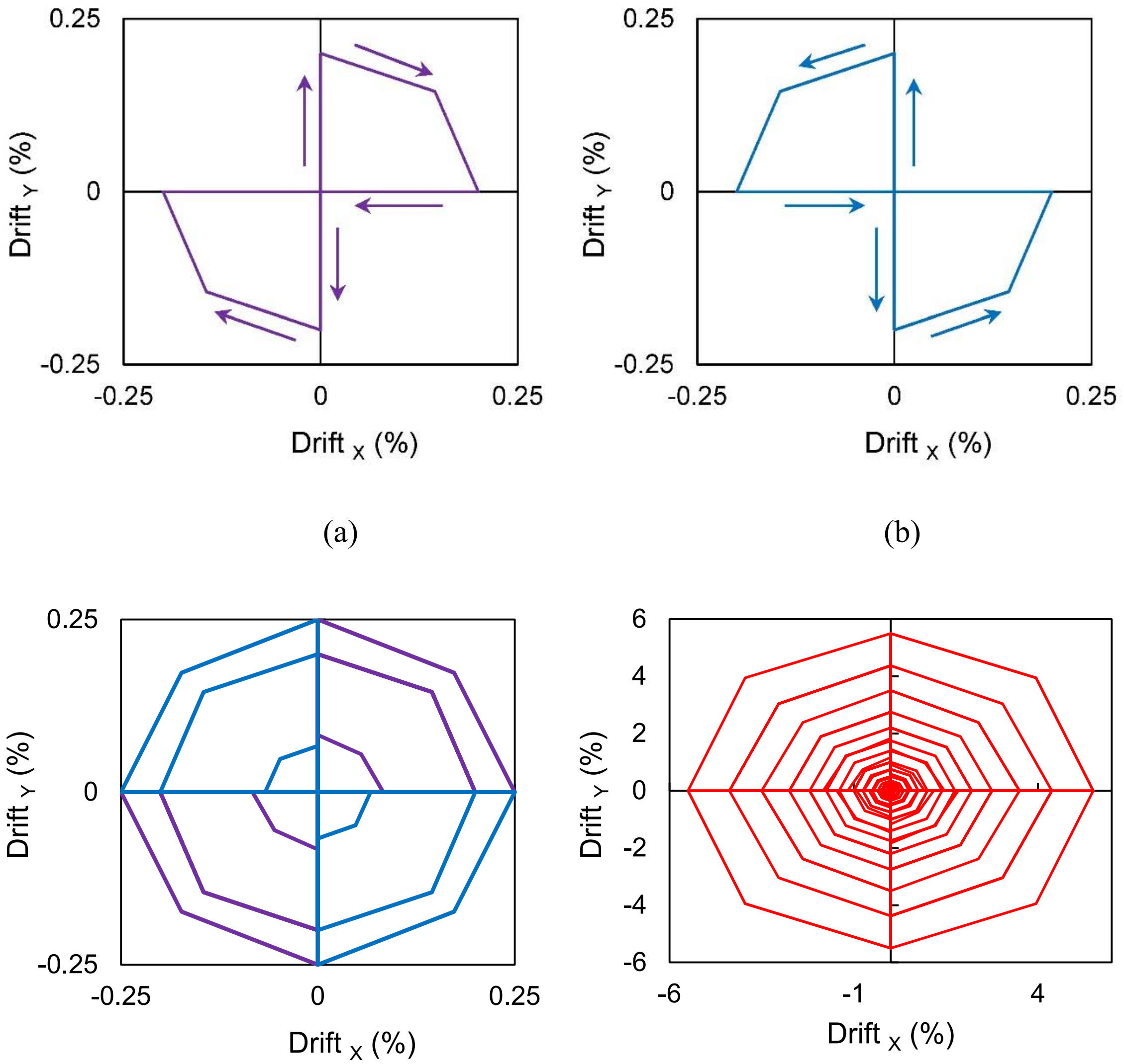

(a) (b)

(c) (d)

Figure 5.9. Applied Loading Protocol to Specimen SP7

5.5. MEASURED RESPONSE OF COLUMN SPECIMENS

Application of the lateral loads to the specimens were followed by initiation of flexural cracking on the tension face of the columns at approximately 0.25% drift ratios. Once the loading continued (in the case of SP1) or the loading direction was reversed (in the case of cyclic tests), flexural cracks were formed on the other face as well. Flexural cracking was accompanied by formation of flexure-shear cracks on the other two faces of the columns that were parallel to the loading direction. Longitudinal bars started to yield at approximately 0.5% drift ratios. Due to cracking of the cover concrete and yielding of the reinforcing bars, the initial stiffness of the columns degraded and they exhibited inelastic behavior. Progression of damage was accompanied by further stiffness degradation in the specimens. However, the specimens could still sustain larger magnitudes of lateral load due to the confining pressure of the hoops and strain hardening of the longitudinal bars. After reaching the peak lateral load capacity, further loading of the specimens was followed by progression of damage to the core concrete, yielding of transverse ties and buckling and fracture of longitudinal bars that caused the specimens to lose strength and stiffness.

Lateral displacement at the top of the specimens (i.e., interface of the top block and loading crosshead) and the applied lateral loads to the specimens were recorded during each test. The force-drift ratio and force-deformation response of the specimens is illustrated in Figures 5.10 to 5.17 . To estimate the yield displacement and corresponding yield force for each specimen, a secant line was extended from the origin to a point on the force-displacement cyclic envelope corresponding to a lateral load of 70% of the peak capacity ($0.7F_{max}$). The secant line was further extended to intersect with the horizontal line at F_{max} (Point A in Figure 5.18). The yield displacement (Δ_y) is defined as the horizontal ordinate of point A, and the corresponding yield force (F_y) is determined by extending a vertical line down from Point A until it intersects the force-deformation cyclic envelope at Point B. This method has been previously applied by other researchers (Bae & Bayrak, 2008; Sivaramakrishnan, 2010) to estimate the yield displacement and yield force. Magnitudes of yield displacement and yield force of each specimen along with those at peak strength and ultimate loading stage of each specimen are represented in Table 5.2.

Except for the test of SP1 which was terminated after exhausting the full stroke capacity of the actuators of the loading crosshead at an ultimate drift ratio (δ_{ult}) equal to 12.1%, the rest of the specimens exhibited significant strength loss by the end of the tests (Figures 5.11 to 5.17). A residual strength ratio (F_{ult}/F_{max}) of 73%, 19%, 23%, 7%, 0%, 19%, and 12% was measured at the end of the tests for specimens SP1 to SP7, respectively (Table 5.2). Severe strength loss in the specimens was accompanied by extensive damage to the reinforcing bars and the core concrete.

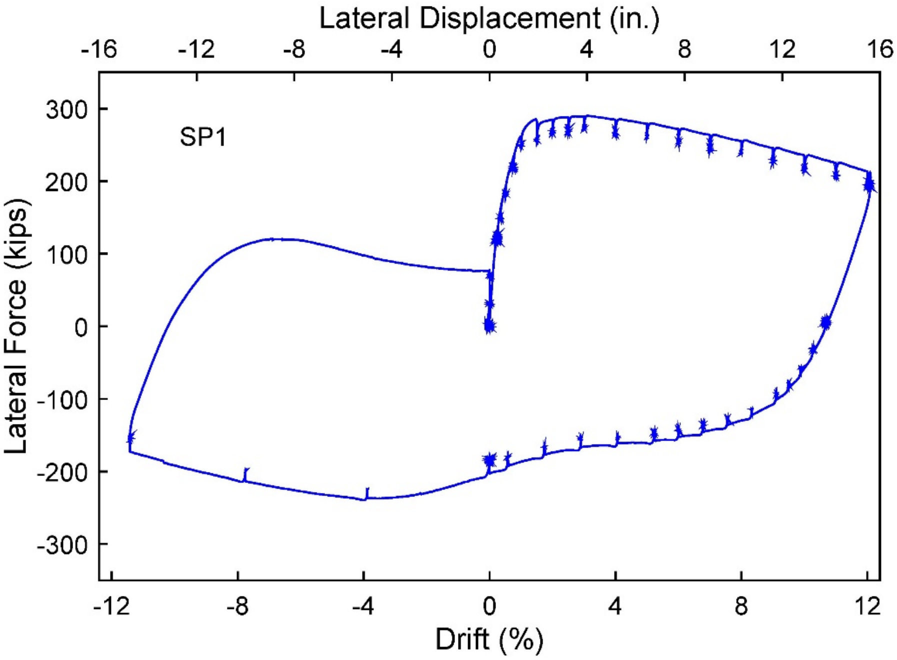

Figure 5.10. Force-Deformation Behavior of Specimen SP1

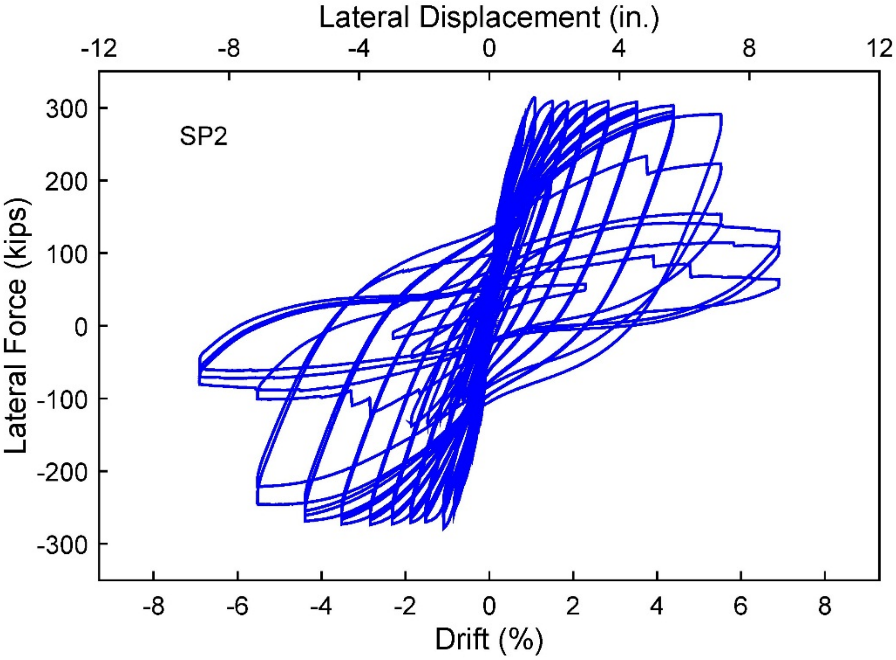

Figure 5.11. Force-Deformation Behavior of Specimen SP2

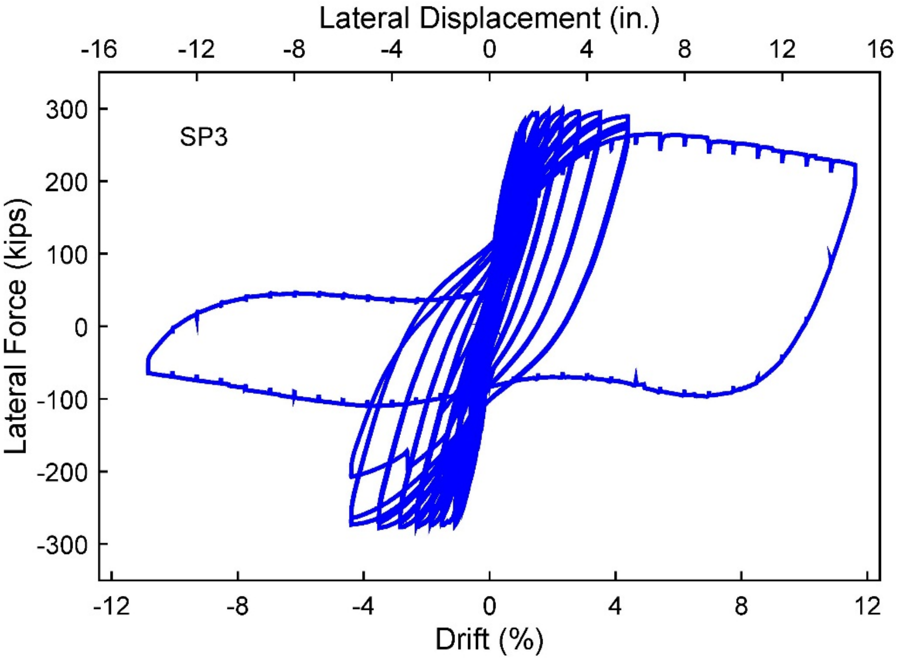

Figure 5.12. Force-Deformation Behavior of Specimen SP3

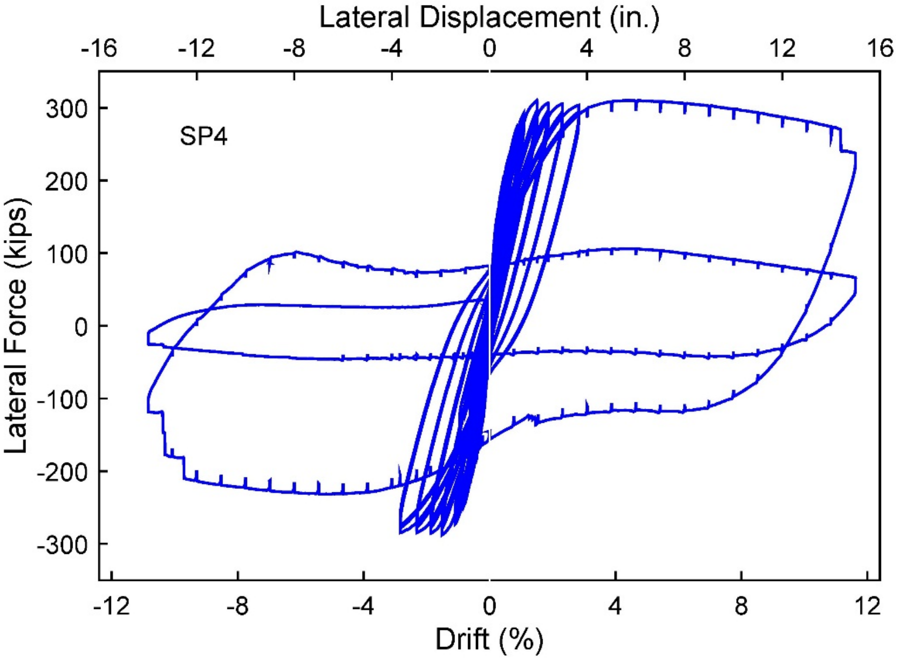

Figure 5.13. Force-Deformation Behavior of Specimen SP4

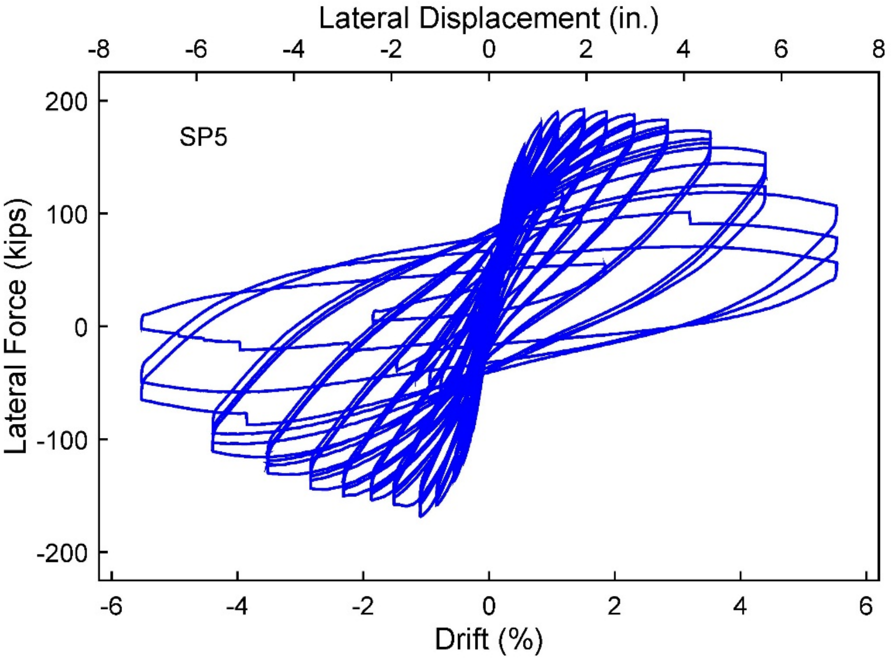

Figure 5.14. Force-Deformation Behavior of Specimen SP5

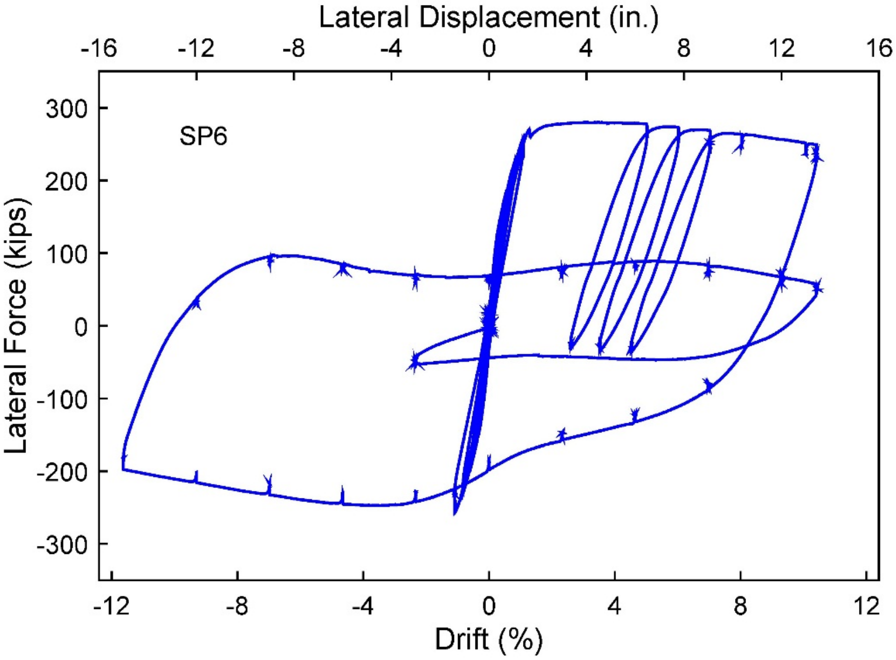

Figure 5.15. Force-Deformation Behavior of Specimen SP6

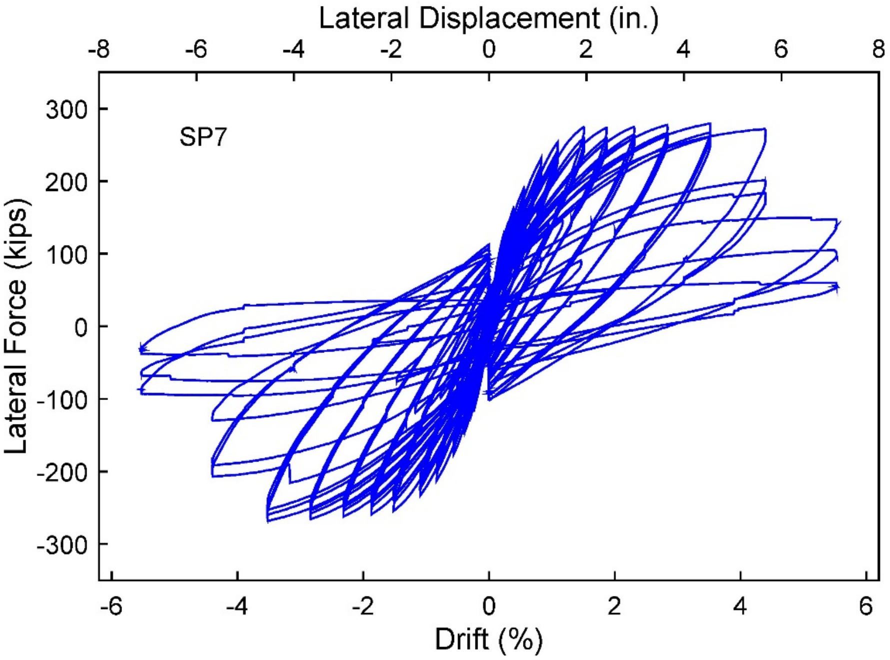

Figure 5.16. Force-Deformation Behavior of Specimen SP7 along Y Direction

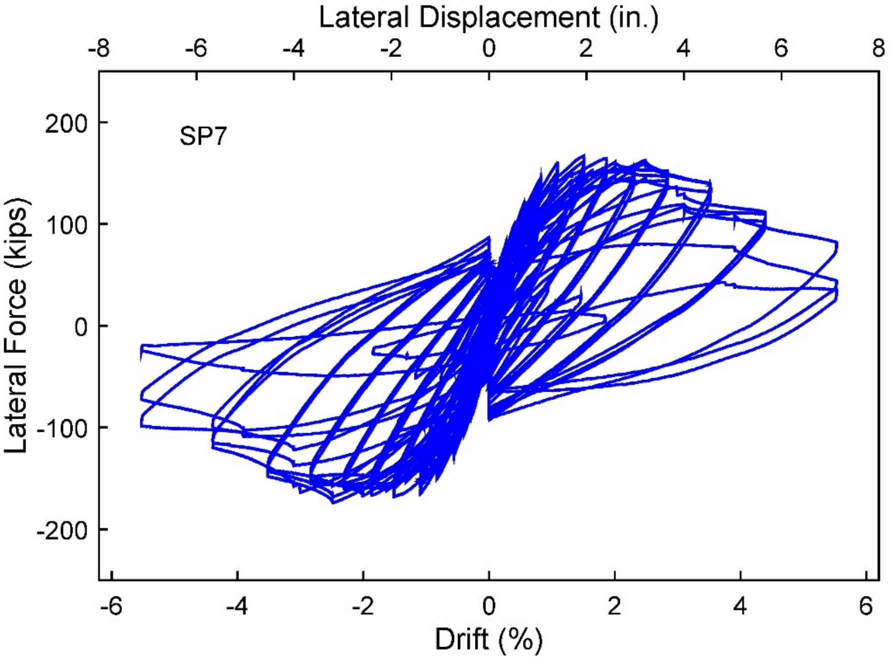

Figure 5.17. Force-Deformation Behavior of Specimen SP7 along X Direction

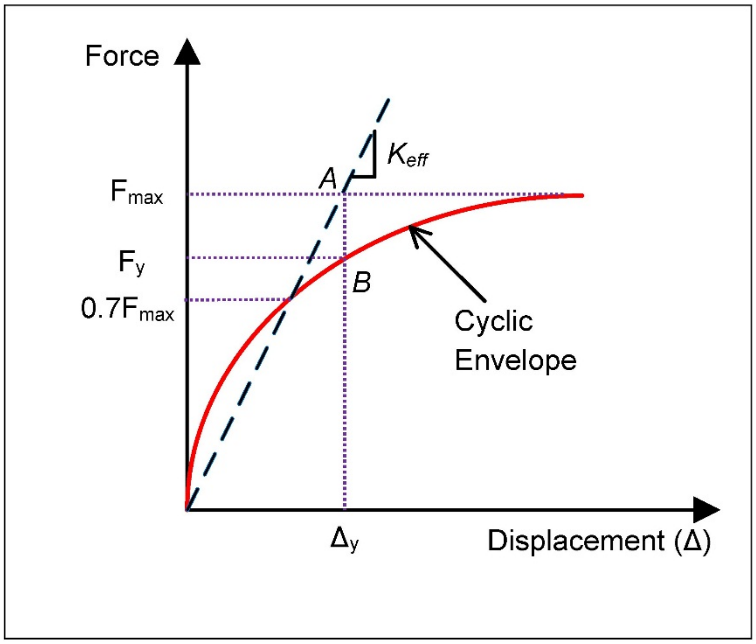

Figure 5.18. Estimation of the Yield Displacement and Yield Force

5.6. DAMAGE ANALYSIS OF TESTED SPECIMENS

The state of damage during loading of the specimens was estimated using three non-cumulative and five cumulative damage indices. The noncumulative damage indices include displacement ductility, and the models proposed by Lybas (Lybas & Sozen, 1977), and Roufaiel (Roufaiel & Meyer, 1987) which are expressed by Eqs. 5.3, 5.4, and 5.6, respectively. The cumulative damage indices that were used in this study include models proposed by Banon (Banon et al., 1981), Stephens (Stephens & Yao, 1987), Wang (Wang & Shah, 1987), Kratzig (Kratzig & Meskouris, 1987), and Park (Park and & Ang, 1985), and these indices are quantified using Eqs. 5.8, 5.11, 5.12, 5.30 and 5.32. Among these indices, displacement ductility and estimated damage indices based on Lybas and Banon models are not scaled. Thus, their results, which will be presented in the next section, are not directly comparable to the rest of the models.

Estimated damage values for each specimen at the end of the tests are included in Table 5.3. The column specimens under the loading protocols exhibited various strength loss at the end of the tests (Table 5.2) so that calculated damage values for various specimens were not comparable. Therefore, to study the effects of applied loading protocols, final damage values should be calculated at a similar state (e.g. 20% or 50%) of strength loss. The computed damage to specimen SP2 based on five damage models is represented in Figure 5.19. The vertical dashed line in this figure corresponds to the state of 20% strength loss in the specimen. At this state, RC columns often require repair to re-establish their capacity and hence this state is commonly considered as the failure of specimens in terms of their useful limit. In this study, the state of 20% strength loss is referred to as the Limit of Useful Capacity at 80% strength (LUC80). In the case of specimen SP2, a strength reduction of 9% and 31% was recorded following the application of peak positive displacements during the 49th and 50th cycles, respectively. Therefore, LUC80 was estimated to occur between these successive cycles.

Among all calculated damage indices for specimen SP2 in Figure 5.19, the one proposed by Wang shows a slow progression until its final magnitude of 1.01 at the end of the test. However, the corresponding damage index at LUC80 (i.e. intersection of the damage line with vertical dashed line related to LUC80), is estimated as 0.6 representing a damage state which is far below failure. Models by Roufaiel and Kratzig suggest a rapid progression of damage at early stages of loading while their estimated damage values remain approximately constant towards the end of the test. The two models estimate a damage index of 0.93 at LUC80. The models by Stephens, and Park suggest a medium rate of damage progression until the 40th cycle. These models suggest a rapid increase in

Table 5.3. Estimated Damage Values at the End of Each Test

Damage Index Model	Column Test Specimen						
	SP1	SP2	SP3	SP4	SP5	SP6	SP7
Stepehens-Yao	0.465	1.679	0.823	0.826	1.688	0.491	1.106
Wang-Shah	0.041	0.466	0.317	0.246	0.455	0.082	0.342
Roufaiel-Meyer	0.975	1.000	1.007	1.019	1.036	1.012	1.008
Kratzig-Emskouris	0.973	0.892	0.934	0.940	0.915	0.852	0.812
Park-Ang	1.010	1.453	1.475	1.309	1.220	0.957	1.459
Banon et al.	15.148	141.377	87.523	72.364	139.687	24.496	76.136
Lybas-Sozen	17.035	46.779	17.480	64.799	31.012	51.817	24.062
Ductility	15.148	10.586	15.324	15.434	10.535	11.645	6.086

damage progression towards the end of the tests which is reasonable because the damage is most likely to occur at an accelerating rate with drift as verified during the tests at the MAST Lab. Stephens and Park models estimate failure after 42 cycles, which over-predicts the failure of the specimens defined on the basis of 20% strength loss.

Since the loading protocols for most of the tested column specimens at the MAST Lab were continued until they exhibited severe strength loss, failure of the specimens was defined based on 50% strength loss (i.e., LUC50) to better estimate the state of damage at later stages of loading. For specimen SP2, LUC50 is located between cycles 50 and 51 (Figure 5.20). As represented in Figure 5.20 shows that while the Wang model still underestimates the extent of damage, the Stephens model correctly predicts failure of SP2. The Roufaiel model also suggests a damage value of 0.96 at LUC50, thus it properly represents a stage that is quite close to failure. The Roufaiel model also shows that it is more deeply affected by accumulation of plastic deformations due to an increase in the magnitude of applied displacements than by cycling at a constant displacement, and the estimated damage index values are closer to the ones by the Kratzig model than the rest of the models. However, Kratzig model suggests a smoother evolution of damage through the entire loading protocol. The model by Park still over-predicts damage to specimen SP2. Defining failure based on LUC50 results in an overall reduction in the calculated damage values by Park model and thus a lower rate of over-prediction of damage. The model by Park shows to increase in accuracy as the degree of damage increases.

Calculated damage indices for specimens SP3 and SP4 are shown in Figures 5.21 and 5.22. The progression of damage for specimens SP3 and SP4 was similar to that of SP2 until application of the final monotonic push (i.e., the last cycle for SP3 and the last two cycles for SP4). Large monotonic displacements that were applied to specimens SP3 and SP4 at the end of their loading protocols resulted in a sudden increase in the magnitudes of estimated damage indices based on the Park model. The final monotonic push also resulted in a large increase in the damage indices calculated by the Stephens, Roufaiel, and Kratzig models for specimen SP4 which had exhibited less strength loss during preceding cyclic loading excursions compared to SP3. The ultimate strength loss for the positive loading direction of SP3 was less than 50% (Table 5.2), and hence the ultimate damage indices were extrapolated to obtain the estimated values at 50% strength loss. At the intersection with LUC50 line, calculated damage values by the Stephens and Kratzig models in the case of SP3, and the Roufaiel and Kratzig models for SP4, were closer to the unit value ($DI = 1$) than those calculated based on the rest of the models. Estimated damage indices by Park are highly affected by the final large displacement cycles. Considering the load-deformation response of specimens SP3 and SP4 (Figures 5.12 and 5.13) confirms that these specimens lost most of their strengths during the last cycles that carry, by far, the majority of the damage. Therefore, calculated damage indices by Park model seems to be closer to the actual performance of column specimens than those calculated by other models. The model by Wang, on the other hand, was not sensitive to the final displacement excursions.

The evolution of damage indices in specimen SP5 were approximately similar to that in specimen SP2 since both specimens were subjected to progressively increasing displacement cycles until failure. As the monotonic test on specimen SP1 was only representative of specimens incorporating larger cross-sectional dimensions (i.e., 36×28 in.), the displacement corresponding to monotonic failure of specimen SP5 that featured a smaller cross-sectional dimensions (i.e., 28×28 in.) was estimated by comparison of the ultimate drift ratios of specimens SP2 and SP5. In specimen SP5, the state of 50% strength loss (i.e., LUC50) was estimated to occur between cycles 49 and 50 (Figure 5.23). Calculated damage indices from the Roufaiel, Kratzig, and Park models suggest a better estimate of failure in specimen SP5 with corresponding damage values of 0.99, 0.91, and 1.11 at LUC50. On the other hand, estimated damage values by the Stephens and Wang models were over- and under-predictive, respectively.

Except the Wang model, calculated damage indices by the rest of the models for specimen SP6 are significantly affected by the applied monotonic push (Figure 5.24). The results from the Roufaiel, Park, and Kratzig models were better in terms of failure prediction than those based on Stephens and Wang models, which were under-predictive. Finally, the evolution of damage indices is specimen SP7 followed an approximately similar pattern as of that in specimen SP2 (Figure 5.25). Among all calculated damage values for specimen SP7, those by the Roufaiel model indicated a better estimation of failure at LUC50. Results from the Stephens and Kratzig models seem to underestimate damage to specimen SP7. However, results from Park model are more realistic as the dissipated energy term in this model were calculated based on total energy that was dissipated during loading of the specimen along X and Y directions while the other models ignore the damage caused by loading along X direction. For these models to be realistic indicators of damage in specimen SP7, calculated damage values in both directions should be combined. Qiu et al. (Qiu, Li, Pan, & Qian, 2002) proposed four methods to include the effect of biaxial loading in the estimation of damage values by Park model. One of their proposed method was to include the total dissipated energy along both loading directions which was used to estimate damage values in specimen SP7. For seven column specimens under biaxial loading in their study, the authors showed that results of all four proposed methods were very close.

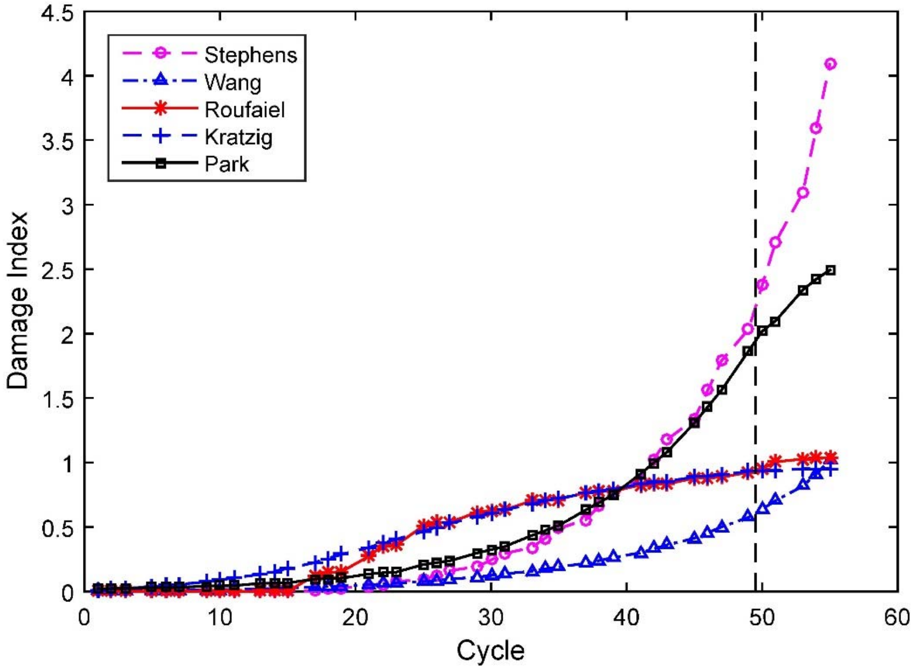

Figure 5.19. Calculated Damage Indices for Specimen SP2 Based on LUC80

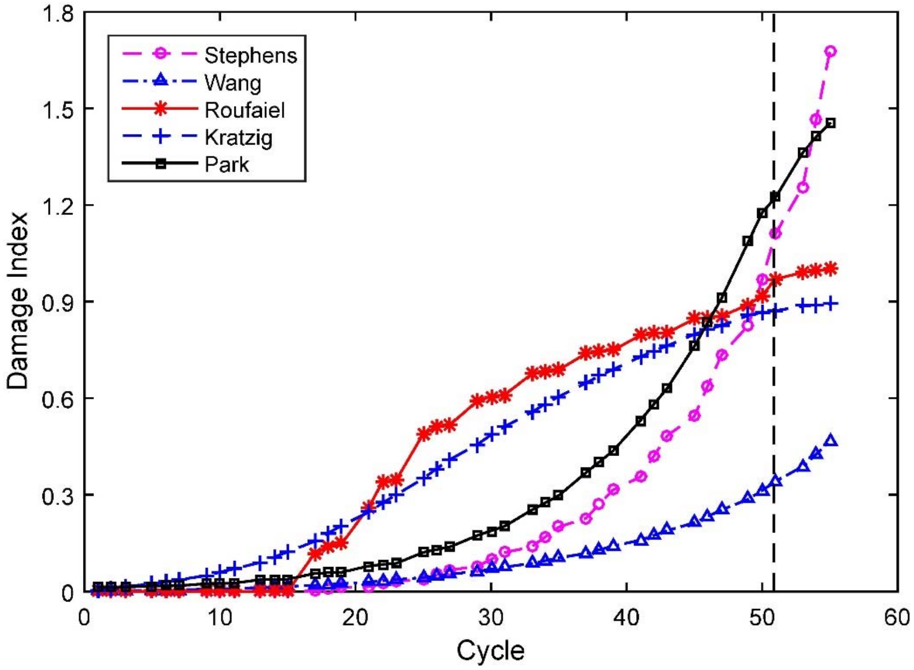

Figure 5.20. Calculated Damage Indices for Specimen SP2 Based on LUC50

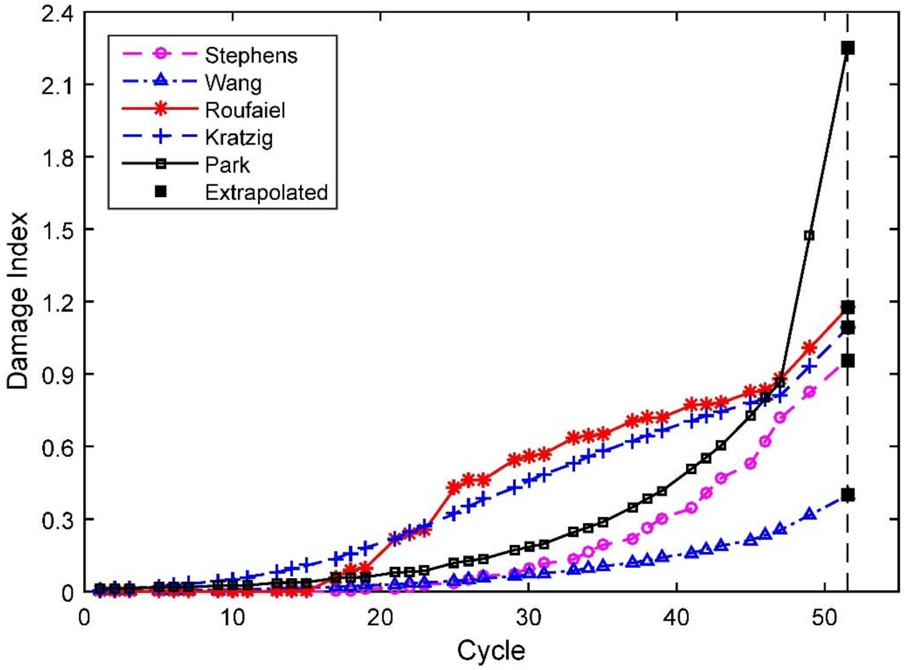

Figure 5.21. Calculated Damage Indices for Specimen SP3 Based on LUC50

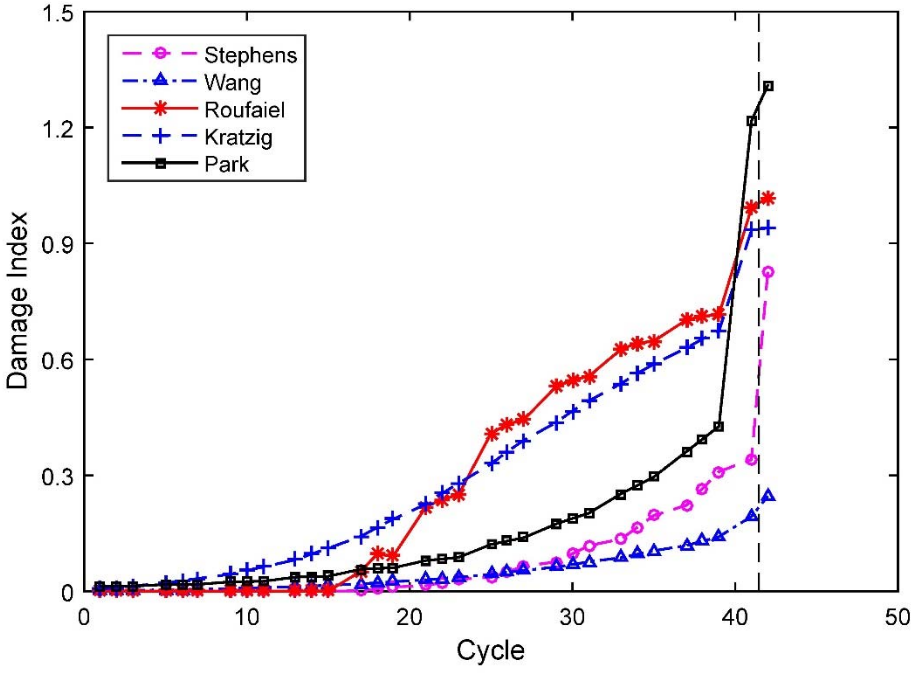

Figure 5.22. Calculated Damage Indices for Specimen SP4 Based on LUC50

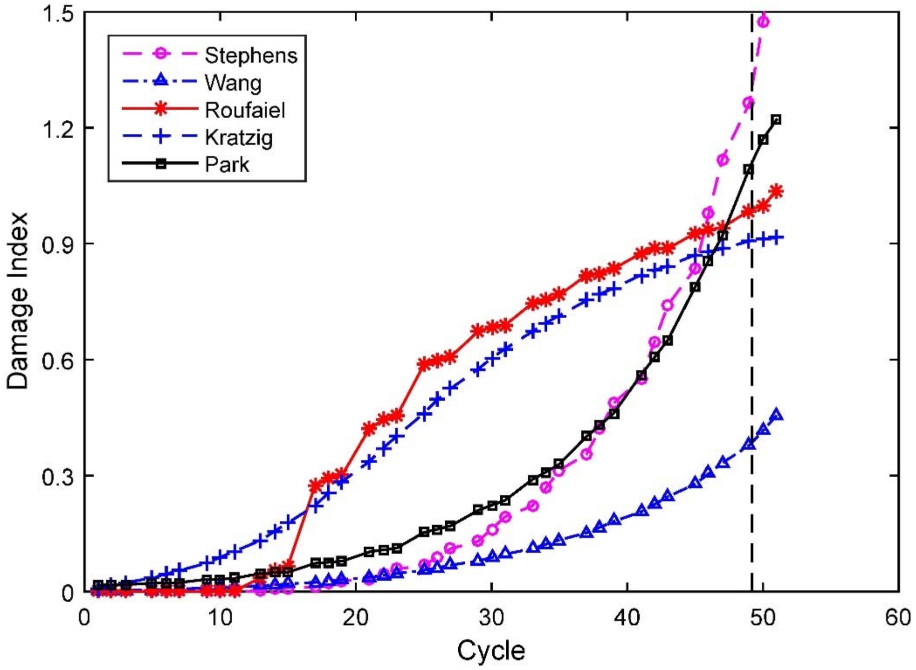

Figure 5.23. Calculated Damage Indices for Specimen SP5 Based on LUC50

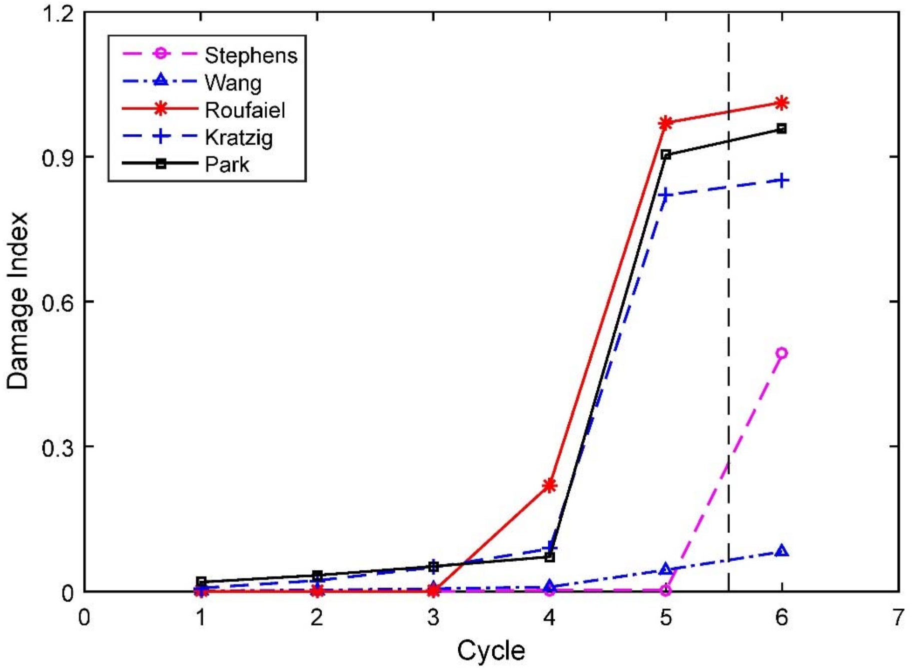

Figure 5.24. Calculated Damage Indices for Specimen SP6 Based on LUC50

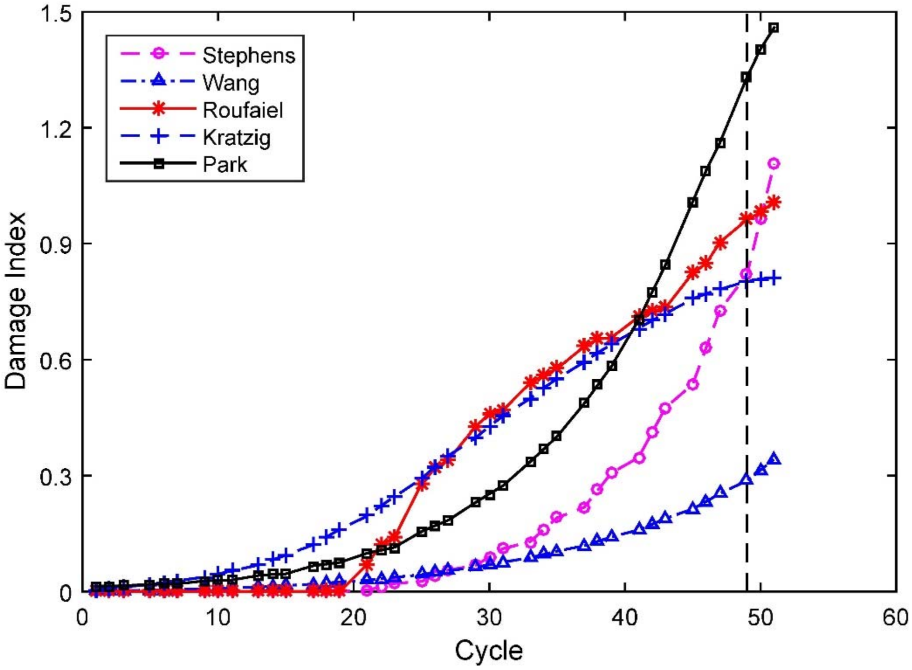

Figure 5.25. Calculated Damage Indices for Specimen SP7 Based on LUC50

5.7. CORRELATION OF CALCULATED AND OBSERVED DAMAGE

It is essential for damage models to be calibrated against damage observed in structures so that they can provide a measure of structural integrity after seismic events and be used for retrofit decision making and seismic loss estimation. The results of such calibrations are typically provided in tables that relate levels of observed damage to the corresponding estimated damage values. Such calibration was carried out by Park and Ang (1985) against a large number of experimental data. The Applied Technology Council (ATC-40, 1996) also defines damage states based on visual observations after earthquakes to help conduct seismic evaluations and preparing retrofit plans.

To better identify the correlation of estimated damage values for the different models with observed damage to the specimens tested at the MAST Lab, the state of damage in the test columns were categorized based on visual observation. Five visual damage categories were defined by considering the extent of required repair and close to what were proposed by Park et al. (1987) and Williams et al. (1997). At peak displacements corresponding to the first and third cycles at a given drift level for each column specimen, eight still images were captured at two elevations. These pictures were analyzed to define the five visual damage categories that are summarized in Table 5.4. Also, images representative of the beginning of visual damage categories II, “Light”, III, “Moderate”, IV, “Severe”, and V, “Failure”, for specimen SP2 are shown in Figures 5.26 to 5.29. The start of visual damage category I, “Negligible”, corresponds to the undamaged state of the specimens and is not shown in these Figures. The measured responses of the specimens during the tests indicate that the first three visual damage categories (“Negligible”, “Light”, “Moderate”) were accompanied by little or no strength loss, the column specimens exhibited noticeable reductions in lateral load capacities at the onset of the “Severe” (IV) and “Failure” (V) visual damage categories (Table 5.5).

Corresponding damage index values at the beginning of visual damage categories II-V were calculated using the damage models discussed in the previous section (Figures 5.30 to 5.34). Additionally, damage values based on the Lybas model (Lybas & Sozen, 1977), Banon’s normalized cumulative displacement model (Banon et al., 1981), and displacement ductility are also computed (Figures 5.35 to 5.37). The corresponding damage values are also included in Table 5.6. Among these models, calculated damage values by the Stephens, Wang, and Park models are clearly distinct for each damage

Table 5.4. Visual Damage Categories Based on Test Observations

Category	Damage State	Description of the Observed Damage
I	Negligible	None or minor hairline flexural or flexural-shear cracks
II	Light	Widespread cracking throughout and initiation of cover spalling
III	Moderate	Widespread cracks > 1/8 in. wide and cover spalling around the corners
IV	Severe	Extensive wide cracking and cover spalling throughout the column and/or single bar exposure
V	Failure	Extensive cover spalling and bar exposure, buckling/fracture of longitudinal bars

category. However, the Wang model suggests damage values that are barely larger than 0.32 at failure. On the other hand, estimated damage values by the Park model corresponding to the start of visual category V for “Failure” are greater than unity in four out of seven specimens. The Roufaiel and Kratzig models estimate damage values that are able to capture failure while their results seem to over-predict early damage in the specimens due to cycling. The model proposed by Lybas results in damage values that are not well distributed for different damage categories. Estimated damage values based on the Lybas model also seem to be significantly affected by large displacements that were applied during monotonic test (i.e., test of specimen SP1) and the last cycles of loading on specimens SP3, SP4, and SP6 while insensitive to accumulated damage over cycles. Calculated displacement ductilities and normalized cumulative displacements (i.e., damage index values computed using the Banon model) are also separated over different visual damage categories with the latter more evenly distributed. However, both of these measures are not scaled which makes interpretation of their estimated values difficult.

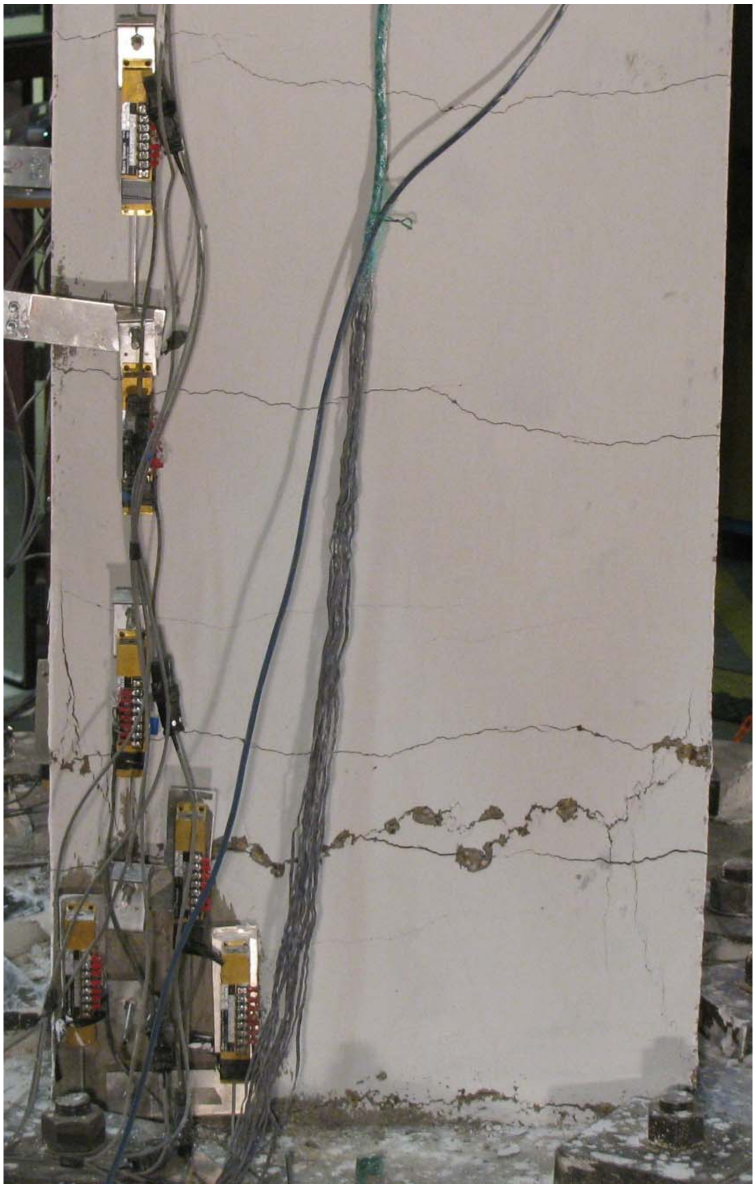

Figure 5.26. Observed Damage at the Beginning of "Light" Damage Category

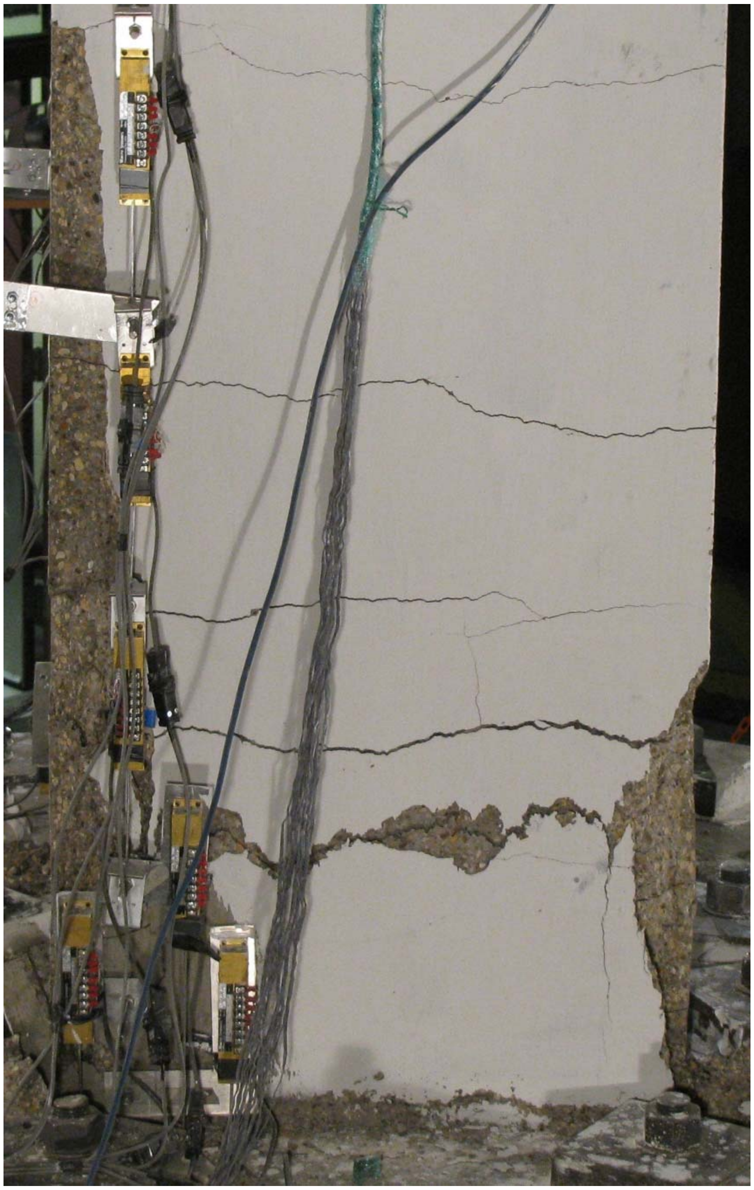

Figure 5.27. Observed Damage at the Beginning of "Moderate" Damage Category

Figure 5.28. Observed Damage at the Beginning of "Severe" Damage Category

Figure 5.29. Observed Damage at the Beginning of "Failure" Damage Category

Table 5.5. Measured Strength Loss at the Onset of Visual Damage Categories

Specimen	Damage Category			
	Light	Moderate	Severe	Failure
SP1	0	0	3.1	*
SP2	1.5	1.6	3.4	7.3
SP3	0.0	0.3	2.5	27.4
SP4	0.0	0.0	5.2	80.3
SP5	1.0	4.8	9.8	24.0
SP6	0.0	0.0	13.5	81.4
SP7	0.0	0.0	0.0	35.9

*Test was terminated prior to achieving this damage category

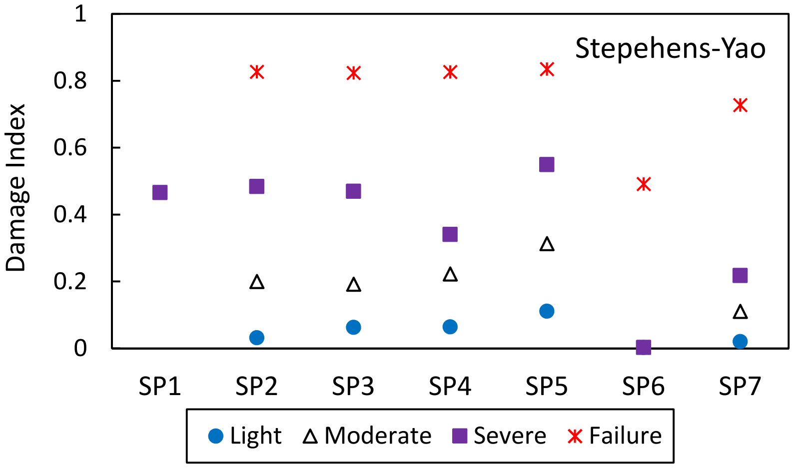

Figure 5.30. Estimated Damage Index Values Corresponding to Different Visual Damage Categories Based on Stephens Model

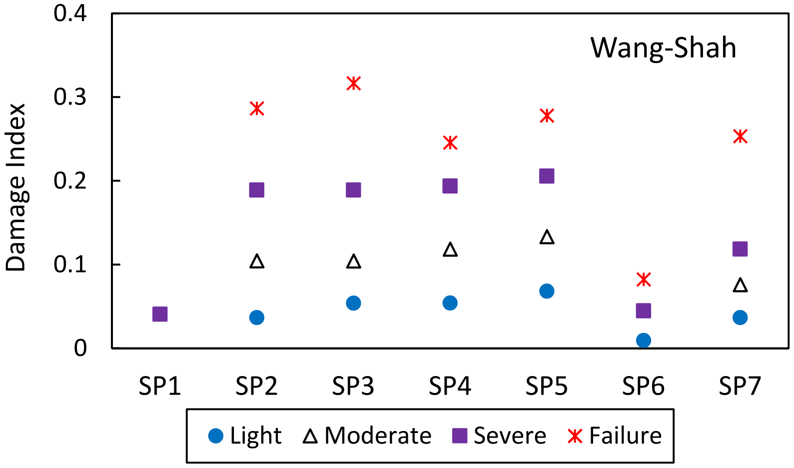

Figure 5.31. Estimated Damage Index Values Corresponding to Different Visual Damage Categories Based on Wang Model

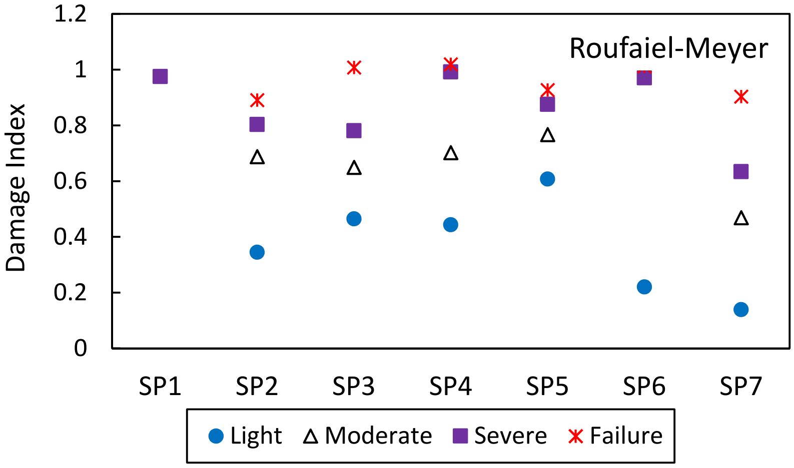

Figure 5.32. Estimated Damage Index Values Corresponding to Different Visual Damage Categories Based on Roufaiel Model

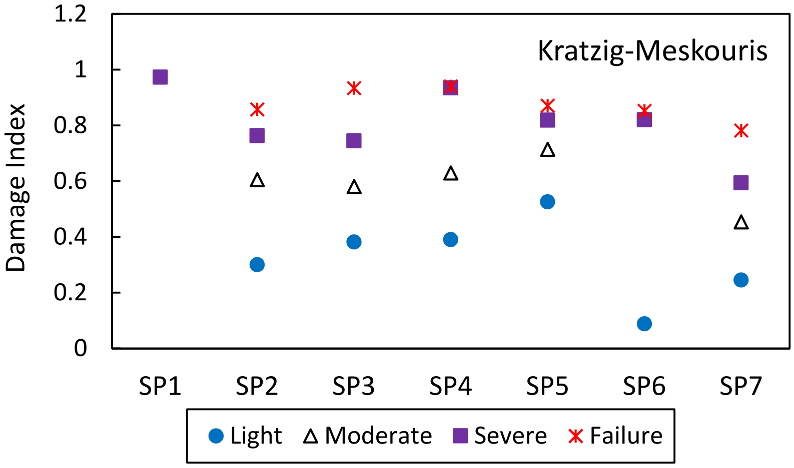

Figure 5.33. Estimated Damage Index Values Corresponding to Different Visual Damage Categories Based on Kratzig Model

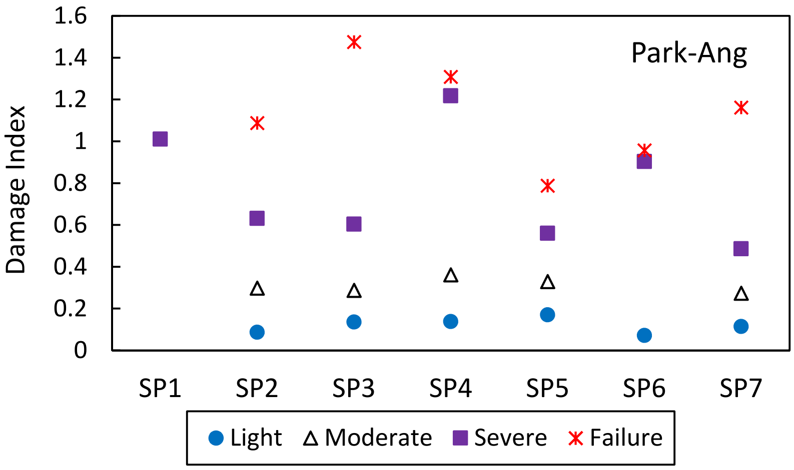

Figure 5.34. Estimated Damage Index Values Corresponding to Different Visual Damage Categories Based on Park Model

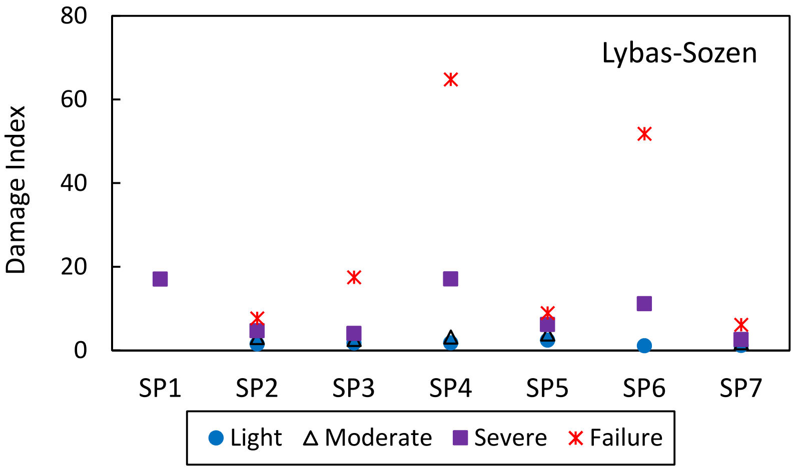

Figure 5.35. Estimated Damage Index Values Corresponding to Different Visual Damage Categories Based on Lybas Model

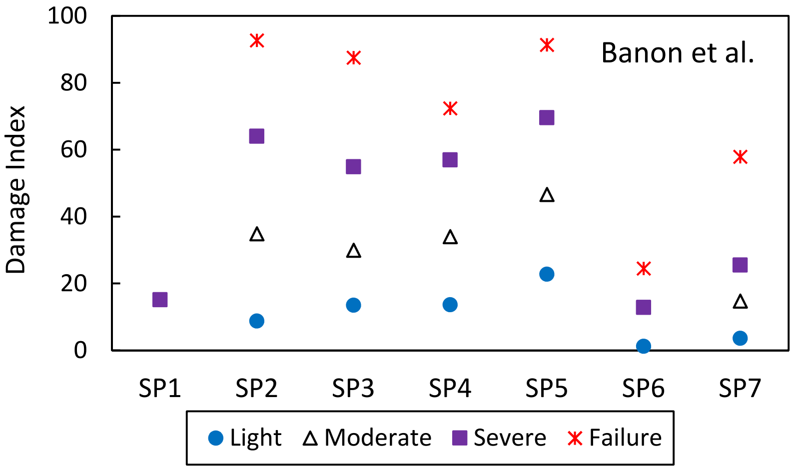

Figure 5.36. Estimated Damage Index Values Corresponding to Different Visual Damage Categories Based on Banon Model

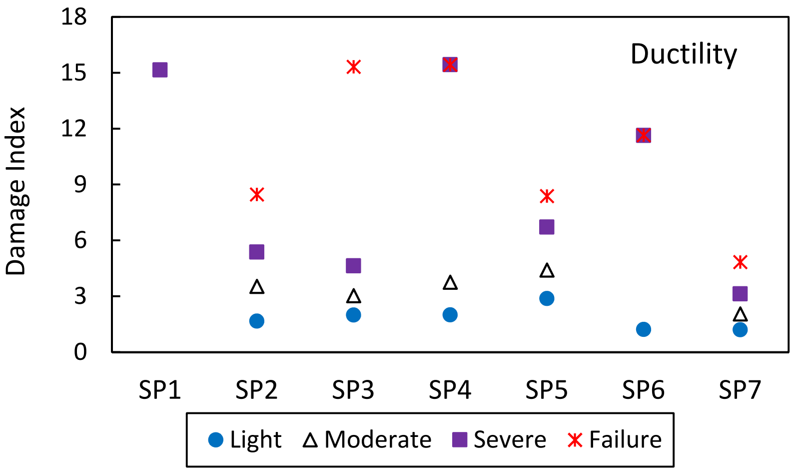

Figure 5.37. Estimated Damage Index Values Corresponding to Different Visual Damage Categories Based on Displacement Ductility

Table 5.6. Estimated Damage Values for Various Visual Damage Categories

Damage Index Model	Column Test Specimen						
	SP1	SP2	SP3	SP4	SP5	SP6	SP7
Visual Damage Category II - Light							
Stepehens-Yao		0.032	0.063	0.065	0.111	0.003	0.020
Wang-Shah		0.037	0.054	0.054	0.068	0.009	0.037
Roufaiel-Meyer		0.345	0.465	0.443	0.607	0.220	0.139
Kratzig-Emskouris		0.300	0.382	0.390	0.525	0.088	0.245
Park-Ang		0.087	0.136	0.138	0.170	0.072	0.114
Banon et al.		8.777	13.483	13.623	22.760	1.218	3.605
Lybas-Sozen		1.510	1.756	1.763	2.444	1.095	1.156
Visual Damage Category III - Moderate							
Stepehens-Yao		0.200	0.192	0.222	0.313		0.111
Wang-Shah		0.104	0.104	0.118	0.133		0.076
Roufaiel-Meyer		0.688	0.649	0.702	0.767		0.469
Kratzig-Emskouris		0.605	0.580	0.629	0.714		0.454
Park-Ang		0.298	0.287	0.361	0.330		0.273
Banon et al.		34.857	29.918	33.975	46.590		14.743
Lybas-Sozen		3.064	2.619	3.177	3.908		1.829
Visual Damage Category IV - Severe							
Stepehens-Yao	0.465	0.484	0.469	0.340	0.549	0.003	0.218
Wang-Shah	0.041	0.189	0.189	0.194	0.205	0.045	0.118
Roufaiel-Meyer	0.975	0.803	0.780	0.992	0.875	0.970	0.634
Kratzig-Emskouris	0.973	0.763	0.744	0.934	0.819	0.820	0.594
Park-Ang	1.010	0.631	0.603	1.217	0.560	0.903	0.486
Banon et al.	15.148	64.001	54.876	56.930	69.529	12.851	25.483
Lybas-Sozen	17.035	4.681	4.033	17.071	6.156	11.156	2.584
Visual Damage Category V - Failure							
Stepehens-Yao		0.827	0.823	0.826	0.835	0.491	0.727
Wang-Shah		0.287	0.317	0.246	0.278	0.082	0.253
Roufaiel-Meyer		0.891	1.007	1.019	0.927	1.012	0.904
Kratzig-Emskouris		0.857	0.934	0.940	0.871	0.852	0.781
Park-Ang		1.087	1.475	1.309	0.788	0.957	1.161
Banon et al.		92.678	87.523	72.364	91.326	24.496	57.878
Lybas-Sozen		7.666	17.480	64.799	8.908	51.817	6.134

5.8. EFFECT OF LOADING PROTOCOLS

One of the primary goals of this study was to characterize the applied lateral loading protocols to the specimens in terms of severity of observed damage. Identification of the worst loading scenario that a specimen is likely to experience during an earthquake will be essential in the generation of capacity curves and determination of structural demands for performance-based design. While all of the loading protocols applied to the specimens tested at the MAST Lab resulted in significant strength reduction and stiffness deterioration, the column specimens subjected to these loading protocols exhibited distinct behavior in terms of ultimate displacement ductility, rate of softening, energy dissipation and damage propagation.

To investigate the effect of the loading protocols, the cyclic load-deformation envelopes for each column specimen were defined by connecting the peak lateral displacements at the first cycle of each drift level. Such calculation for specimen SP2 is shown in Figure 5.38. Comparison of the cyclic envelopes indicates that among all seven specimens, specimen SP5, which had a larger axial load ratio ($P/f'_cA_g = 0.3$), and specimen SP7, which was subjected to biaxial loading, exhibited the smallest drift capacities (Figure 5.39). Specimen SP2 also reached its ultimate strength at a drift level smaller than those for specimens SP3, SP4, and SP6 which lost most of their strength during the final monotonic push at the end of their loading protocols. The displacement during the monotonic push applied to these specimens resulted in rapid strength reduction and stiffness deterioration, while the softening occurred gradually for specimens subjected to only cyclic load reversals (SP2, SP5, and SP7). The effect of the lateral loading protocols on the initial stiffness and peak load capacity of the specimens was insignificant.

The extent of damage to the specimens due to loading can be characterized by the energy that they dissipated during the tests. Accumulated dissipated energy during loading of the specimens is shown in Figure 5.40. Since the strength loss at the end of the test was different for each of the specimens, estimated energy dissipations of specimens SP2, SP4, SP5, SP6 and SP7 were truncated at the state of 50% strength loss (i.e., LUC50) so that the ultimate magnitudes for these specimens can be comparable. On the other hand, the energy dissipation of specimen SP1 and SP3 at LUC50 were obtained by extrapolation, as these specimens exhibited a final strength loss that was less than 50% of the peak lateral load capacity during loading of the specimens in the positive direction. As illustrated in Figure 5.40, column SP7 showed larger magnitudes of energy dissipation than did the other specimens, but reached a final value equal to that for specimen SP2. Calculated energy dissipation for specimen SP7 were obtained by summation of the corresponding values during loading of the specimen along X and Y directions. Specimen SP5 that featured a smaller cross-sectional dimension dissipated less energy than all other specimens except SP6 which dissipated energy mainly over one cycle. Energy dissipation in specimen SP6 was basically quite similar to that of specimen SP1 which was under monotonic loading. The ultimate monotonic push that was applied to specimens SP3 and SP4 resulted in a rapid increase in the dissipated energy. However, at LUC50, both of these specimens exhibited less dissipated energy than specimen SP2 that sustained more cyclic displacement excursions.

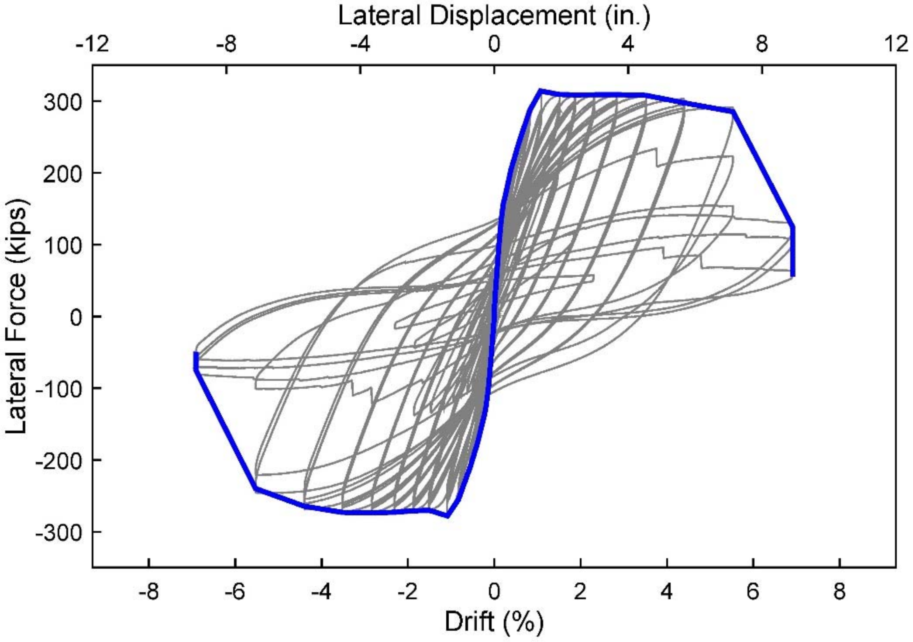

Figure 5.38. Generation of Cyclic Envelope for Specimen SP2

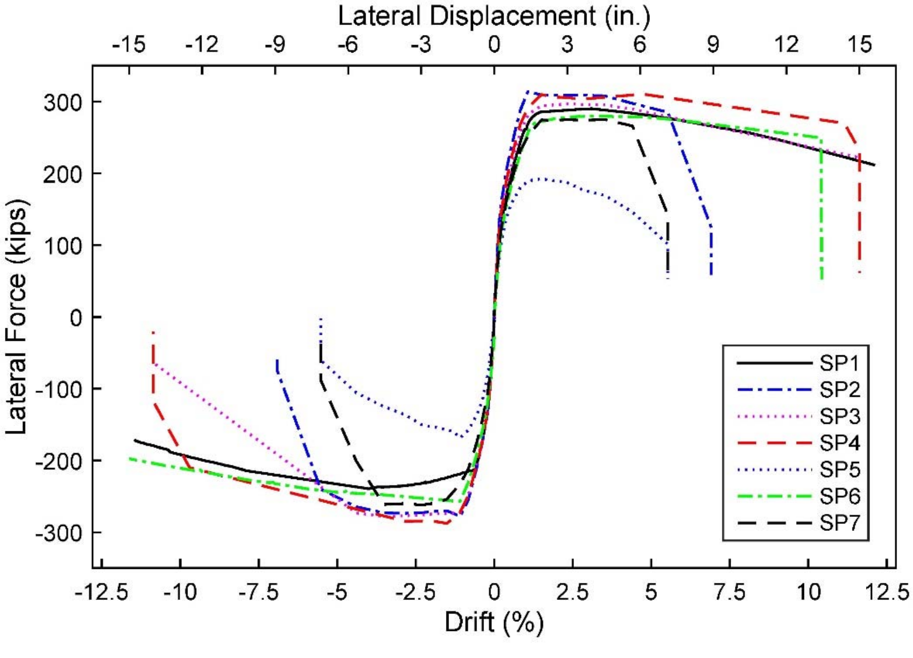

Figure 5.39. Force-Deformation Cyclic Envelopes for All Tests

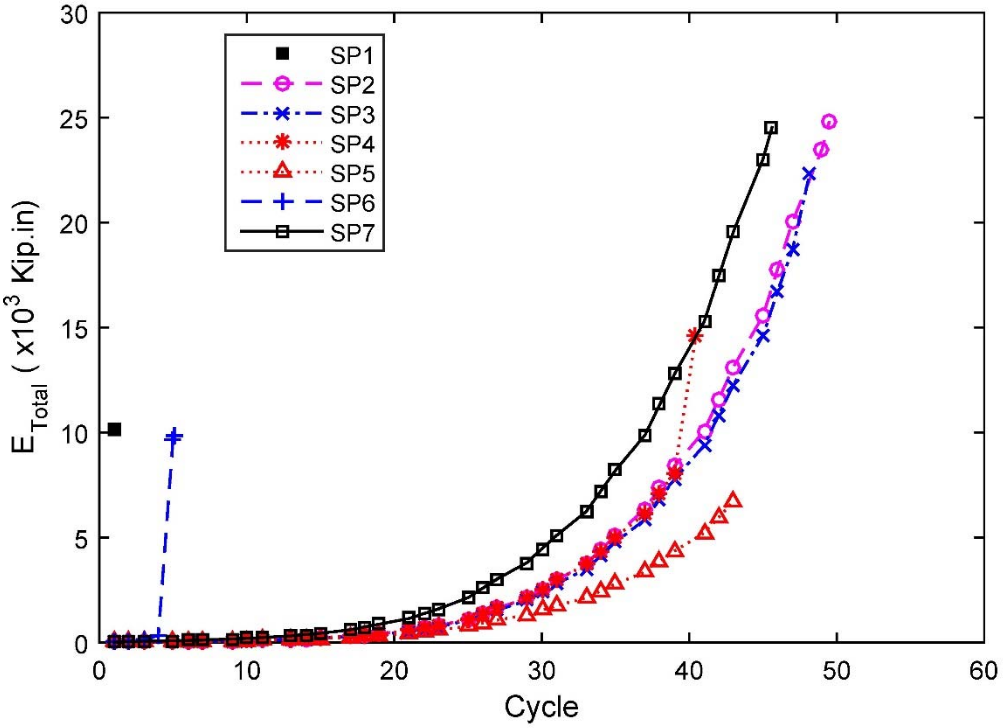

Figure 5.40. Calculated Energy Dissipation until Occurrence of 50% Strength Loss

Energy dissipation during loading was accompanied by the evolution of damage in the specimens. Calculated damage values based on the Lybas (Lybas & Sozen, 1977) model are shown in Figure 5.41. Specimen SP5 shows a higher rate of stiffness reduction during cyclic loading reversals. However, the applied monotonic displacement to specimens SP1, SP3, SP4, and SP6 results in major stiffness deterioration such that the calculated damage values at 50% strength loss (i.e., LUC50) of these specimens are significantly larger than those in cyclic tests. Estimated damage indices by the Stephens, Roufaiel and Kratzig models for all specimens, which are given in Figures to 5.44, suggest a higher extent of damage in specimen SP5 than specimen SP2 that experienced similar displacement excursions, but under a lower axial load ratio. On the other hand, the monotonic push which was applied during loading of specimens SP3, SP4, and SP6 also caused a major increase in the calculated damage values by the Roufaiel and Kratzig models. Specimen SP1 which was under monotonic loading as well as specimen SP6 which experienced the least number of cycles exhibit final damage values based on the Roufaiel model that are close to those of all other specimens except specimen SP3. The Kratzig model, on the hand, suggests a smaller damage value for SP6, and the Stephens model does not predict failure for SP6 at all. Calculated damage values by the Stephens, Roufaiel and Kratzig models do not capture the extent of damage in specimen SP7, which was subjected to the biaxial loading protocol, when only Y-direction response is used for estimating the damage indices. To obtain a more realistic value for specimen SP7, damage indices should be calculated in both loading directions and their effects combined. However, the combination of damage that occurs from loading in two orthogonal directions is challenging, especially if a unit value is expected at failure. Among the damage models considered, the one proposed by Park can inherently capture the effect of loading in two directions when the total energy dissipation during loading in both directions is taken into account. Calculated damage values obtained from the Park model (Figure 5.45) suggest a higher extent of damage in specimen SP7 than all other specimens except SP3.

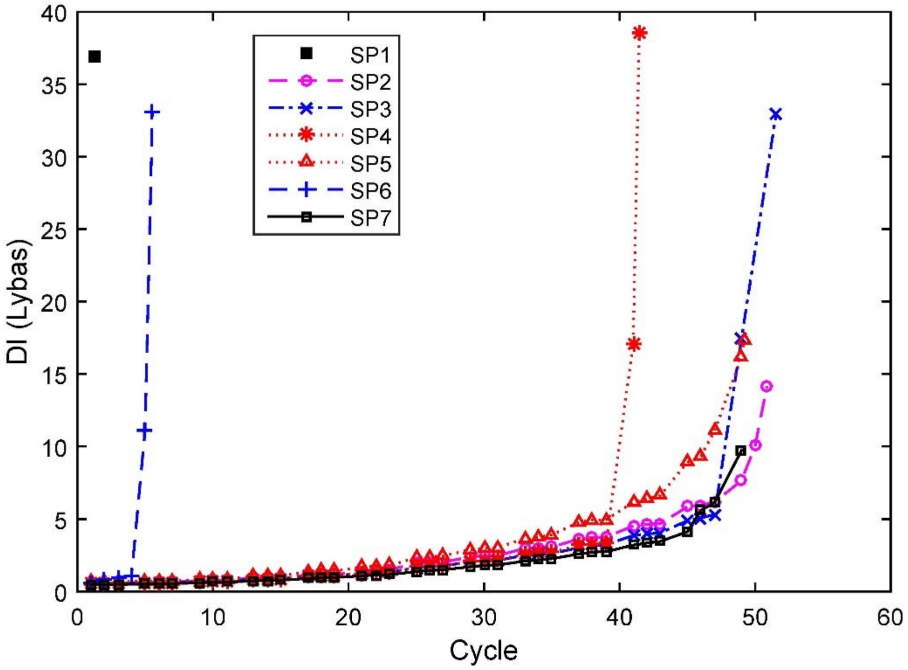

Figure 5.41. Damage Values by Lybas Model until Occurrence of 50% Strength Loss

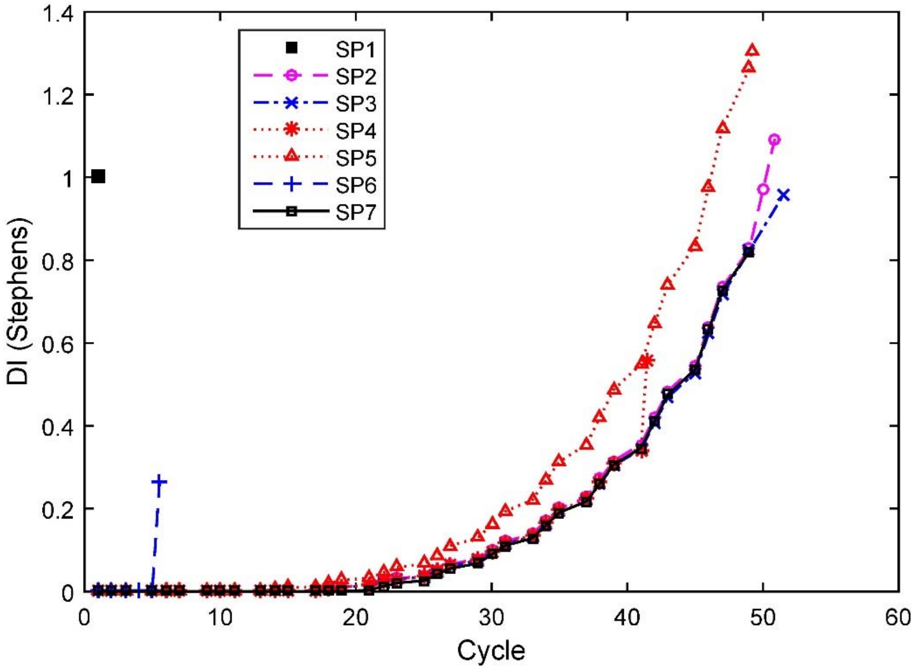

Figure 5.42. Damage Values by Stephens Model until 50% Strength Loss

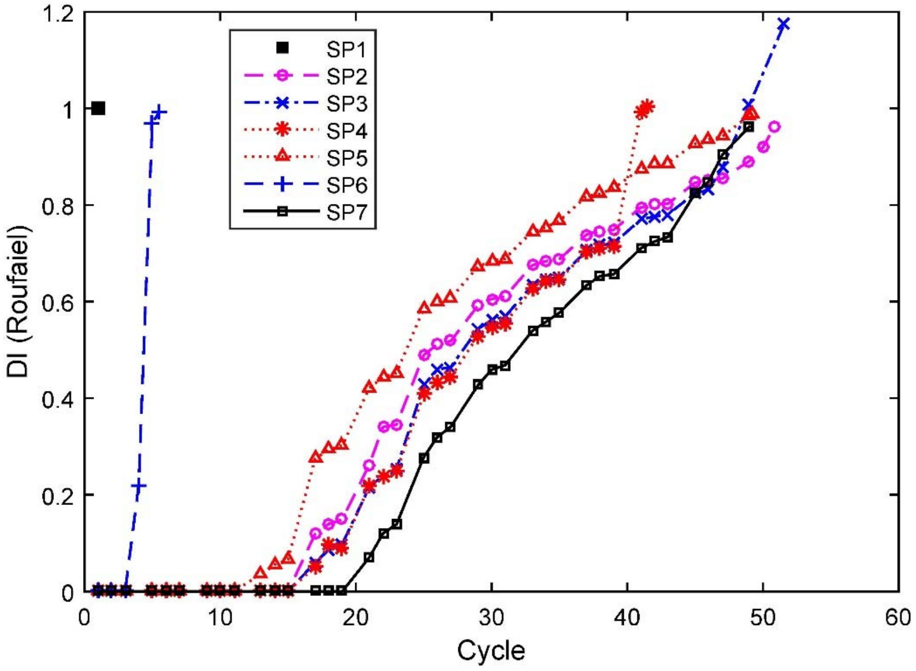

Figure 5.43. Damage Values by Roufaiel Model until 50% Strength Loss

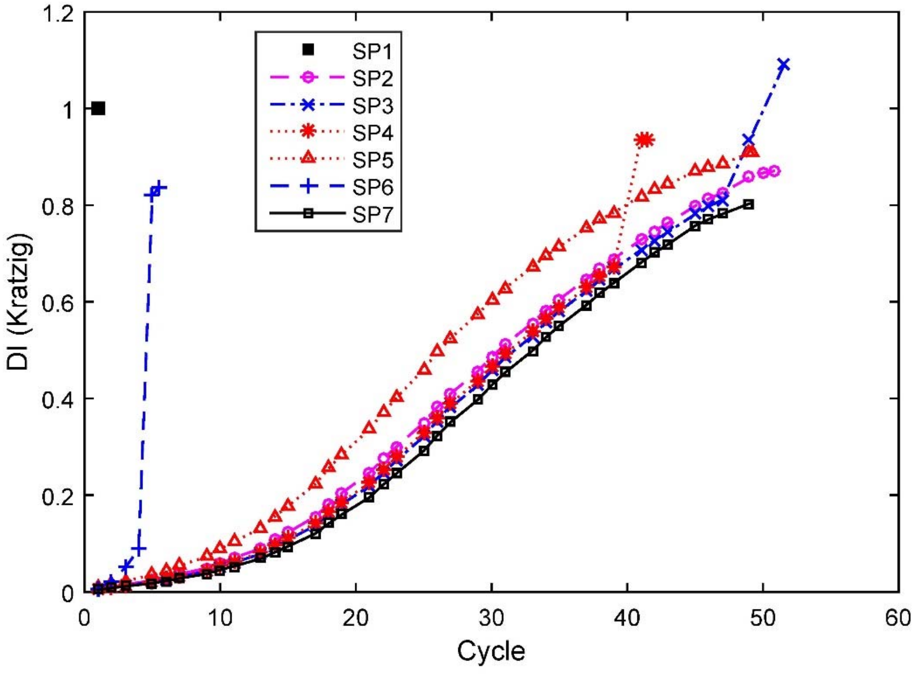

Figure 5.44.Damage Values by Kratzig Model until Occurrence of 50% Strength Loss

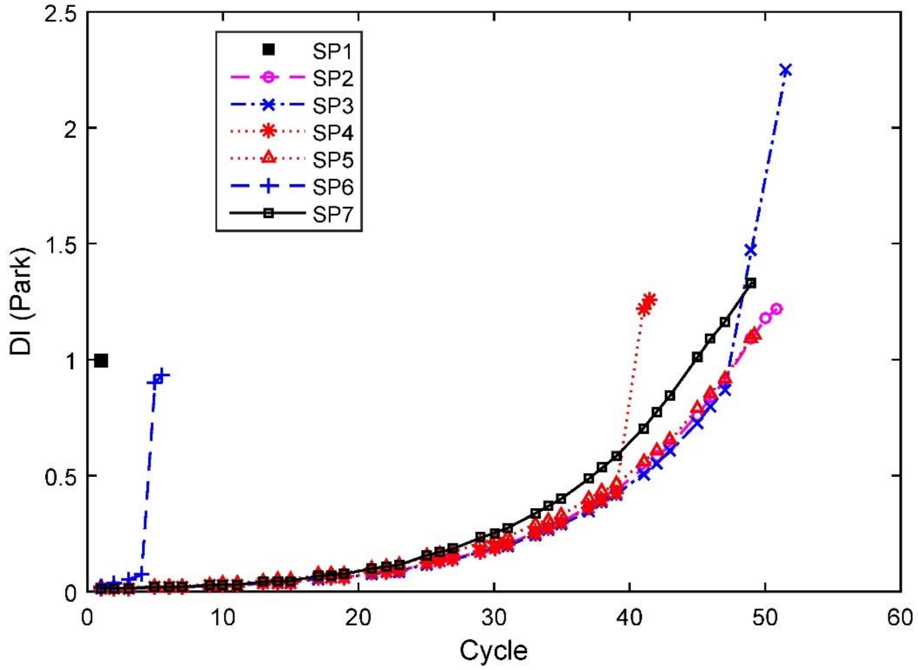

Figure 5.45. Damage Values by Park Model until Occurrence of 50% Strength Loss

5.9. CONCLUSIONS

The extent of damage during tests of seven RC columns subjected to distinct loading protocols was estimated using nine noncumulative and cumulative damage models. In addition, observed damage to the specimens during each test was categorized into five visual damage categories and used as a measure to validate the calculated damage indices. Among all damage index models that were studied, the model by Park and Ang (1985) provided an overall better estimate of actual damage in specimens. The observed and calculated damage were used along with performance characteristics of the columns based on force-deformation envelope, and energy dissipation to assess the applied loading protocols. The results of this study indicate that the column specimen subjected to biaxial loading (i.e., SP7) experienced more damage during loading. For this specimen, results from Park and Ang (1985) model were closer to the actual state of damage in the specimen as it can directly take the effect of biaxial loading into account provided that the calculated energy dissipation values include the hysteretic energy dissipated during loading in both directions. The study also shows that column specimen SP5, which had a similar loading protocol as of that for SP2, but under a larger axial load ratio, sustained a more severe extent of damage. In addition, the monotonic push displacement that was applied following a number of cyclic displacement reversals resulted in a rapid strength reduction in the specimens and a higher extent of damage as of that in the case of pure cyclic or monotonic displacements.

CHAPTER 6

SUMMARY, CONCLUSIONS, AND RECOMMENDATIONS

6.1. SUMMARY

A series of seven full-scale reinforced concrete columns were tested at the MAST Lab as a part of this study to increase the understanding of the performance of typical columns in high-rise buildings that are designed using current code requirements and then subjected to extreme seismic events. The columns featured cross-sectional dimensions that were larger than almost all columns tested previously under simulated seismic loadings and were subjected to distinct lateral loading protocols including a monotonic five cyclic uniaxial and biaxial, and a near-collapse loading protocol. To investigate the post-peak behavior of the columns, loading of the specimens continued beyond the common stopping point during previous tests. During these applied loading protocols, the specimens exhibited significant strength reduction (i.e., 80%) and stiffness deterioration.

Results from these tests were considered along with those from previous tests on RC columns to study the effects of cross-sectional size of column specimens on their seismic performance. To this end, five parameters were considered necessary to characterize column performance, and these include moment capacity, effective stiffness, drift capacity, displacement ductility, and longitudinal bar buckling. With the test data and these five parameters, the effect of cross-sectional depth of columns on each parameter was studied in detail.

The loading capabilities at the MAST Lab enabled the testing of full-scale column specimens at larger drift ratios than those applied during previous tests, and under these conditions, the column specimens exhibited a previously unobserved mode of failure which features in-plane buckling of the longitudinal reinforcing bars. A 3D FE model of the lower portion of the columns was analyzed in addition to that of isolated bars to investigate the in-plane buckling phenomenon that occurred in 6 of 7 tests at the MAST Lab. A parametric study was carried out to investigate the effect of concrete compressive strength, longitudinal bar size and spacing, tie spacing, and column cross-sectional on the buckling behavior of reinforcing bars.

Damage to the specimens during each test was quantified by several cumulative and noncumulative damage index models. In addition, the damage to the specimens was categorized by visual test observations and used as a measure to assess the calculated damage indices. Calculated and observed damage to the specimens were then considered along with the force-deformation cyclic envelope, and hysteretic energy dissipation during each test to study the effect of loading protocols.

6.2. CONCLUSIONS

Experimental and analytical investigation of the seismic performance of the full-scale RC columns in this research leads to the following conclusions:

1) A study of the parameters defining the seismic performance of RC columns confirms that effective stiffness, drift capacity, and displacement ductility of RC columns can be significantly affected by axial load and aspect ratios. The effect of axial load for stocky columns with aspect ratio smaller than 2 is minor. However, for columns with larger aspect ratios, an increase in the axial load ratio and aspect ratio is accompanied by an increase in the effective stiffness while it has an adverse effect on the drift capacity and displacement ductility.
2) It was also confirmed that the drift capacity and displacement ductility of RC columns are sensitive to the characteristics of the lateral loading protocols so that an increase in the number of loading cycles results in a reduction of drift capacity and displacement ductility. In addition, RC columns exhibit a lower drift capacity under biaxial loading condition than under a uniaxial loading protocol.
3) Flexural moment capacity, normalized effective stiffness, drift capacity, and displacement ductility of RC columns constructed with normal strength to moderately high strength concrete (2.5 ksi (17.24 MPA) $\leq f'_c \leq$ 10 ksi (68.94 MPA)) are not generally affected by the dimension of their cross-sectional depths.
4) The MAST tests revealed a mode of longitudinal bar buckling that has not been reported and is not considered in the structural design of RC columns: An in-

plane buckling mode was observed in which the bars buckle parallel to the face of the column as opposed to the presumption that they would only buckle in the outward direction.

5) In-plane buckling of bars typically occurred about the strong axis of the bars during tests at the MAST Lab while the common assumption is that longitudinal bars buckle only about their weak axis.
6) Results from FE modeling of the lower portion of the columns suggest that concrete with a larger nominal compressive strength (f'_c) helps to postpone in-plane buckling of the bars.
7) In addition, larger longitudinal bar sizes are recognized to be more likely to experience in-plane buckling as their restraint demands are higher. However, the effect of bar spacing is insignificant.
8) Unlike outward buckling, in-plane buckling of reinforcing bars is not controlled by tie-spacing. Rather, it is the concrete surrounding the bars that restrains the bars from in-plane buckling.
9) The specimens featuring larger cross-sectional dimensions that incorporate larger bar sizes are shown to be more critical to in-plane bar buckling.
10) An analysis of the damage evolution during tests of RC columns at the MAST Lab under distinct loading protocols reveals that columns will exhibit more damage during cyclic biaxial loading protocol as compared to uniaxial loading conditions.
11) All damage index models that were considered in this research, except the one proposed by Park and Ang (1985), are described for uniaxial loading. The

model proposed by Park and Ang (1985) can directly include the effect of biaxial loading if the hysteretic energy dissipated during loading in both directions is considered.

12) The study also shows that column SP5, which had a similar loading protocol to that of SP2, but under a larger axial load ratio, experienced more damage.

13) Finally a monotonic push displacement that was applied following a number of cyclic displacement reversals resulted in a rapid strength reduction in the specimens. Among all specimens, SP7 and SP3 which sustained a biaxial loading protocol and a uniaxial symmetric cyclic followed by a monotonic push, respectively exhibited more damage. On the other hand, the loading protocols with the smallest number of cycles (i.e., the monotonic and the near –collapse loading protocols) were the least damaging ones. The symmetric cyclic loading protocol that was applied to specimen SP2 was in the middle in terms of severity of resulted damage.

6.3. RECOMMENDATIONS FOR FUTURE RESEARCH

The current study recommends that the following topics be investigated in the future studies:

1) The in-plane buckling of reinforcing bars needs to be investigated experimentally in more detail. The effects of concrete compressive strength, longitudinal bar size and spacing, tie spacing and overall cross-sectional size of the columns require verification by conducting tests for which in-plane buckling is the main focus of the study.

2) A more detailed FE analysis to include the effects of deterioration of concrete surrounding the bars would be beneficial for a better estimation of the sensitivity of in-plane bar buckling to the relevant parameters.
3) Methods to prevent in-plane buckling of longitudinal bars need to be studied. Crossties with 180 degree end hooks may be helpful in restraining the bars from in-plane buckling.

REFERENCES

ACI Committee 318. (2011). *Building Code Requirements for Structural Concrete (ACI 318-11) and Commentary*. Farmington Hills, MI: American Concrete Institute.

ACI Committee 318. (2014). *Building Code Requirements for Structural Concrete (ACI 318-14) and Commentary*. American Concrete Institute.

ACI Committee 374. (2005). *Acceptance Criteria for Moment Frames Based on Structural Testing and Commentary (ACI 374.1–05)*. American Concrete Institute, Detroit, MI, USA.

Advisory Committee on Earthquake Hazards Reduction (ACEHR). (2008). *Effectiveness of the National Earthquake Hazards Reduction Program* (A Report from the Advisory Committee on Earthquake Hazards Reduction) (p. 34).

American Society of Civil Engineers (ASCE). (2000). *Prestandard and commentary for the seismic rehabilitation of buildings* (FEMA-356). Federal Emergency Management Agency, Washington, D.C.

American Society of Civil Engineers (ASCE). (2007). *Seismic Rehabilitation of Existing Buildings (ASCE/SEI 41-06)* (ASCE 41-06 Supplement No.1). American Society of Civil Engineers, Reston, VA.

Applied Technology Council (ATC). (2009a). *Effects of Strength and Stiffness Degradation of Seismic Response* (FEMA P440A). Federal Emergency Management Agency, Washington, D.C.

Applied Technology Council (ATC). (2009b). *Qualification of Building Seismic Performance Factors* (FEMA P695). Federal Emergency Management Agency, Washington, D.C.

ASTM A 370-03a. (2003). Standard Test Methods and Definitions for Mechanical Testing of Steel Products. ASTM International, West Conshohocken, PA.

ASTM A706/A706M-03a. (2003). Standard Specification for Low-Alloy Steel Deformed and Plain Bars for Concrete Reinforcement. ASTM International, West Conshohocken, PA.

ASTM C 39C/C39M. (2003). Standard Test Method for Compressive Strength of Cylindrical Concrete Specimens. ASTM International, West Conshohocken, PA.

ASTM Standard A615/A615M-03a. (2003). Specification for Deformed and Plain Carbon-Steel Bars for Concrete Reinforcement. ASTM International, West Conshohocken, PA.

ATC-40. (1996). Seismic evaluation and retrofit of concrete buildings. Applied Technology Council, Redwood City, CA.

Bae, S., & Bayrak, O. (2008). Seismic Performance of Full-Scale Reinforced Concrete Columns. *ACI Structural Journal*, *105*(2), 123–133.

Bae, S., Mieses, A. M., & Bayrak, O. (2005). Inelastic buckling of reinforcing bars. *Journal of Structural Engineering*, *131*(2), 314–321.

Banon, H. (1980). *Prediction of seismic damage in reinforced concrete frames*. Massachusetts Institute of Technology.

Banon, H., Irvine, H. M., & Biggs, J. M. (1981). Seismic damage in reinforced concrete frames. *Journal of the Structural Division*, *107*(9), 1713–1729.

Bayrak, O., & Sheikh, S. A. (1996). Confinement steel requirements for high strength concrete columns. In *Proceedings of the 11th World Conference on Earthquake Engineering*.

Bayrak, O., & Sheikh, S. A. (2001). Plastic hinge analysis. *Journal of Structural Engineering*, *127*(9), 1092–1100.

Berry, M. P., & Eberhard, M. O. (2005). Practical performance model for bar buckling. *Journal of Structural Engineering*, *131*(7), 1060–1070.

Berry, M. P., Parrish, M., & Eberhard, M. O. (2004). PEER structural performance database user's manual (version 1.0). *University of California, Berkeley*.

Bournas, D. A., & Triantafillou, T. C. (2010). Bar buckling in RC columns confined with composite materials. *Journal of Composites for Construction*, *15*(3), 393–403.

Bresler, B., & Gilbert, P. H. (1961). Tie requirements for reinforced concrete columns. *ACI Journal Proceedings*, *58*(11), 555–570.

Brown, W. A., Lehman, D. E., & Stanton, J. F. (2008). *Bar buckling in reinforced concrete bridge columns*. PEER Report 2007/11, Pacific Engineering Research Center, University of California, Berkeley, CA.

Chai, Y. H., Romstad, K. M., & Bird, S. M. (1995). Energy-based linear damage model for high-intensity seismic loading. *Journal of Structural Engineering*, *121*(5), 857–864.

Chung, Y. S., Meyer, C., & Shinozuka, M. (1987). Seismic damage assessment of reinforced concrete members.

Coffin, (LF) Jr. (1954). A study of the effects of cyclic thermal stresses in ductile metals. In *ASME* (Vol. 76, pp. 931–950).

Crisfield, M. A. (1981). A fast incremental/iterative solution procedure that handles "snap-through." *Computers & Structures*, *13*(1), 55–62.

Dhakal, R. P., & Fenwick, R. C. (2008). Detailing of plastic hinges in seismic design of concrete structures, *105*(6), 740–749.

Dhakal, R. P., & Maekawa, K. (2002). Reinforcement Stability and Fracture of Cover Concrete in Reinforced Concrete Members. *Journal of Structural Engineering*, *128*(10), 1253–1262.

Elwood, K. J., & Eberhard, M. O. (2009). Effective stiffness of reinforced concrete columns. *ACI Structural Journal*, *106*(4), 476–484.

Erduran, E., & Yakut, A. (2004). Drift based damage functions for reinforced concrete columns. *Computers & Structures*, *82*(2), 121–130.

Esmaeily-Gh, A., & Xiao, Y. (2002). *Seismic behavior of bridge columns subjected to various loading patterns* (PEER Report 2002/15). Pacific Earthquake Engineering Research Center, College of Engineering, University of California, Berkeley.

French, C. W., Schultz, A. E., HAJJAR, J. F., Shield, C. K., Ernie, D. W., Dexter, R. J., … Wan, C. P. (2004). Multi-axial subassemblage testing (MAST) system: Description and capabilities. In *Proceedings of the 13th World Conference on Earthquake Engineering, Vancouver, Canada*.

Frosch, R. J. (1999). Another look at cracking and crack control in reinforced concrete. *ACI Structural Journal*, *96*(3), 437–442.

Ghannoum, W., Sivaramakrishnan, B., Pujol, S., Catlin, A. C., Fernando, S., Yoosuf, N., & Wang, Y. (2012). ACI 369 rectangular column database. *Network for Earthquake Engineering Simulation (database), Dataset, DOI*, *10*, D36688J50.

Gilbersten, N. D., & Moehle, J. P. (1980). Experimental Study of Small-Scale R/C Columns Subjected to Axial and Shear Force Reversal. *Structural Research Series*, (481).

Gomes, A., & Appleton, J. (1997). Nonlinear cyclic stress-strain relationship of reinforcing bars including buckling. *Engineering Structures*, *19*(10), 822–826. http://doi.org/10.1016/S0141-0296(97)00166-1

Gosain, N. K., Jirsa, J. O., & Brown, R. H. (1977). Shear requirements for load reversals on RC members. *Journal of the Structural Division*, *103*(7), 1461–1476.

Haselton, C. B., Liel, A. B., Lange, S. T., & Deierlein, G. G. (2008). *Beam-column element model calibrated for predicting flexural response leading to global collapse of RC frame buildings* (PEER Report 2007/3). Pacific Earthquake Engineering Research Center, College of Engineering, University of California, Berkeley.

Ingham, J. M., Liddell, D., & Davidson, B. J. (2001). Influence of loading history on the response of a reinforced concrete beam. *Bulletin of the New Zealand National Society for Earthquake Engineering*, *34*(2), 107–124.

Jaradat, O. A., McLean, D. I., & Marsh, M. L. (1998). Performance of Existing Bridge Columns under Cyclic Loading? Part 1: Experimental Results and Observed Behavior. *ACI Structural Journal*, *95*(6).

Jeong, G. D., & Iwan, W. D. (1988). The effect of earthquake duration on the damage of structures. *Earthquake Engineering & Structural Dynamics*, *16*(8), 1201–1211.

Kent, D. C., & Park, R. (1971). Flexural members with confined concrete. *Journal of the Structural Division*, *97*(7), 1969–1990.

Kratzig, W. B., & Meskouris, M. (1987). Nonlinear seismic analysis of reinforced concrete frames. *Earthquake Prognostics*, 453–462.

Kreger, M. E., & Linbeck, L. (1986). Behavior of reinforced concrete columns subjected to lateral and axial load reversal. In *Proceedings of the Third US National Conference on Earthquake Engineering* (pp. 24–28).

Kunnath, S. K., El-Bahy, A., Taylor, A. W., & Stone, W. C. (1997). Cumulative seismic damage of reinforced concrete bridge piers. In *Technical Report NCEER*. US National Center for Earthquake Engineering Research.

Kunnath, S. K., Reinhorn, A. M., & Lobo, R. F. (1992). IDARC version 3.0: a program for the inelastic damage analysis of reinforced concrete structures.

Lee, J., & Fenves, G. L. (1998). Plastic-damage model for cyclic loading of concrete structures. *Journal of Engineering Mechanics*, *124*(8), 892–900.

Lehman, D. E., & Moehle, J. P. (1998). Influence of longitudinal reinforcement ratio on column response. In *Eleventh European Earthquake Engineering Conference*.

Lehman, D. E., & Moehle, J. P. (2000). *Seismic performance of well-confined concrete bridge columns*. Pacific Earthquake Engineering Research Center.

Lubliner, J., Oliver, J., Oller, S., & Onate, E. (1989). A plastic-damage model for concrete. *International Journal of Solids and Structures*, *25*(3), 299–326.

Lybas, J. M., & Sozen, M. A. (1977). Effect of Beam Strength and Stiffness on Dynamic Behavior of R/C Coupled Walls. *Department of Civil Engineering, University of Illinois*.

Mander, J. B., & Cheng, C.-T. (1995). Replaceable hinge detailing for bridge columns. In *Proceedings of the National Seismic Conference on Bridges and Highways: "Progress in research and practice."* San Diego, CA.

Mander, J. B., Panthaki, F. D., & Kasalanati, A. (1994). Low-cycle fatigue behavior of reinforcing steel. *Journal of Materials in Civil Engineering*, *6*(4), 453–468.

Mander, J. B., Priestley, M. J. N., & Park, R. (1984). *Seismic Design of Bridge Piers.* Research Report 84-2, Department of Civil Engineering, University of Canterbury, Christchurch, New Zealand.

Manson, S. S. (1953). Behavior of materials under conditions of thermal stress.

Massone, L. M., Polanco, P., & Herrera, P. (2014). Experimental and Analytical Response of RC Wall Boundary Elements. Presented at the 10th U.S. National Conference on Earthquake Engineering, Anchorage, AK.

Mehanny, S. S., Kuramoto, H., & Deierlein, G. G. (2001). Stiffness Modeling of Reinforced Concrete Beam-Columns for Frame Analysis. *ACI Structural Journal*, *98*(2), 215–225.

Mercan, B., Schultz, A. E., & Stolarski, H. K. (2010). Finite element modeling of prestressed concrete spandrel beams. *Engineering Structures*, *32*(9), 2804–2813.

Miner, M. A. (1945). Cumulative damage in fatigue. *Journal of Applied Mechanics*, *12*(3), 159–164.

Monti, G., & Nuti, C. (1992). Nonlinear cyclic behavior of reinforcing bars including buckling. *Journal of Structural Engineering*, *118*(12), 3268–3284.

Moyer, M. J., & Kowalsky, M. J. (2003). Influence of tension strain on buckling of reinforcement in concrete columns. *ACI Structural Journal*, *100*(1), 75–85.

National Institute of Standards and Technology (NIST). (2009). *Research Required to Support Full Implementation of Performance-Based Seismic Design* (NIST GCR 09-917-2). National Institute of Standards and Technology Building and Fire Research Laboratory, Gaithersburg, Maryland.

Nojavan, A., Schultz, A. E., Chao, S.-H., Haselton, C. B., Simasathien, S., Palacios, G., & Liu, X. (2014). Preliminary Results for NEESR Full-Scale RC Column Tests under Collapse-Consistent Loading Protocols. Presented at the 10th U.S. National Conference on Earthquake Engineering, Anchorage, AK.

Nojavan, A., Schultz, A. E., Haselton, C., Simathathien, S., Liu, X., & Chao, S.-H. (2015). A New Data Set for Full-Scale Reinforced Concrete Columns under Collapse-Consistent Loading Protocols. *Earthquake Spectra*, *31*(2), 1211–1231.

Palacios, G. (2015). *Performance of full-scale ultra-high performance fiber-reinforced concrete column subjected to extreme earthquake-type loading and effect of surface preparation on the cohesion and friction factors of the aashto interface shear equation*. The University OF Texas at Arlington.

Palmgren, A. (1924). Die lebensdauer von kugellagern. *Zeitschrift Des Vereins Deutscher Ingenieure*, *68*(14), 339–341.

Pantazopoulou, S. J. (1998). Detailing for reinforcement stability in RC members. *Journal of Structural Engineering*, *124*(6), 623–632.

Papia, M., Russo, G., & Zingone, G. (1988). Instability of longitudinal bars in RC columns. *Journal of Structural Engineering*, *114*(2), 445–461.

Park, R. (1989). Evaluation of ductility of structures and structural assemblages from laboratory testing. *Bulletin of the New Zealand National Society for Earthquake Engineering*, *22*(3), 155–166.

Park, Y.-J., & Ang, A. H.-S. (1985). Mechanistic seismic damage model for reinforced concrete. *Journal of Structural Engineering*, *111*(4), 722–739.

Park, Y.-J., Ang, A. H.-S., & Wen, Y.-K. (1987). Damage-limiting aseismic design of buildings. *Earthquake Spectra*, *3*(1), 1–26.

Paulay, T., & Priestley, M. J. . (1992). *Seismic Design of Reinforced Concrete and Masonry Buildings* (1 edition). New York: Wiley-Interscience.

Powell, G., & Simons, J. (1981). Improved iteration strategy for nonlinear structures. *International Journal for Numerical Methods in Engineering*, *17*(10), 1455–1467.

Pujol, S. (2002, August). *Drift capacity of reinforced concrete columns subjected to displacement reversals*. Purdue University.

Qiu, F., Li, W., Pan, P., & Qian, J. (2002). Experimental tests on reinforced concrete columns under biaxial quasi-static loading. *Engineering Structures*, *24*(4), 419–428.

Ramm, E. (1981). *Strategies for tracing the nonlinear response near limit points*. Springer.

Rodriguez, M. E., Botero, J. C., & Villa, J. (1999). Cyclic stress-strain behavior of reinforcing steel including effect of buckling. *Journal of Structural Engineering*, *125*(6), 605–612.

Roufaiel, M. S., & Meyer, C. (1987). Analytical modeling of hysteretic behavior of R/C frames. *Journal of Structural Engineering*, *113*(3), 429–444.

Saatcioglu, M., & Grira, M. (1999). Confinement of reinforced concrete columns with welded reinforced grids. *ACI Structural Journal*, *96*(1), 29–39.

Scribner, C. F. (1986). Reinforcement buckling in reinforced concrete flexural members. *ACI Journal Proceedings*, *83*(6), 966–973.

Sivaramakrishnan, B. (2010). *Non-linear modeling parameters for reinforced concrete columns subjected to seismic loads*. The University of Texas at Austin.

Stephens, J. E., & Yao, J. T. (1987). Damage assessment using response measurements. *Journal of Structural Engineering*, *113*(4), 787–801.

Stone, W. C., Cheok, G. S., & Stanton, J. F. (1995). Performance of hybrid moment-resisting precast beam-column concrete connections subjected to cyclic loading. *ACI Structural Journal*, *91*(2), 229–249.

Stone, W. C., & Taylor, A. W. (1993). *Seismic performance of circular bridge columns designed in accordance with AASHTO* (NIST Building Science Series No. 170). Gaithersburg, MD: National Institute of Standards and Technology.

Suda, K., Murayama, Y., Ichinomiya, T., & Shimbo, H. (1996). Buckling behavior of longitudinal reinforcing bars in concrete column subjected to reverse lateral loading. In *Proc., 11th World Conf. on Earthquake Engineering*.

Takemura, H., & Kawashima, K. (1997). Effect of loading hysteresis on ductility capacity of reinforced concrete bridge piers. *Journal of Structural Engineering*, *43*, 849–858.

Wang, M.-L., & Shah, S. P. (1987). Reinforced concrete hysteresis model based on the damage concept. *Earthquake Engineering & Structural Dynamics*, *15*(8), 993–1003.

Williams, M. S., & Sexsmith, R. G. (1995). Seismic damage indices for concrete structures: a state-of-the-art review. *Earthquake Spectra*, *11*(2), 319–349.

Williams, M. S., Villemure, I., & Sexsmith, R. G. (1997). Evaluation of seismic damage indices for concrete elements loaded in combined shear and flexure. *ACI Structural Journal*, *94*(3).

Yao, J. T. P., & Munse, W. H. (1962). Low-cycle axial fatigue behavior of mild steel. *ASTM Special Technical Publication*, *338*, 5–24.

Yarandi, M. S. (2007). *Seismic retrofit and repair of existing reinforced concrete bridge columns by transverse prestressing*. University of Ottawa, Canada.

Zhou, X., Higashi, Y., Jiang, W., & Shimizu, Y. (1985). Behavior of reinforced concrete column under high axial load. *Transactions of the Japan Concrete Institute*, *7*, 385–392.

APPENDIX A

CONSTRUCTION, INSTRUMENTATION, AND INSTALLATION OF SPECIMENS

A.1. CONSTRUCTION

The specimens were constructed in an upright position at the University of Texas at Arlington (UTA) and shipped to the MAST Lab for testing. Reinforcement details for perimeter and space frame colum specimens are shown in Figs. A.1 to A.4. As illustrated in Figure A.5 the reinforcing cage was built horizontally and placed into the concrete forms prior to pouring of the concrete. The specimens were constructed along with a footing block, and a top block to be connected to the MAST strong floor and loading crosshead, respectively (Figure A.6).

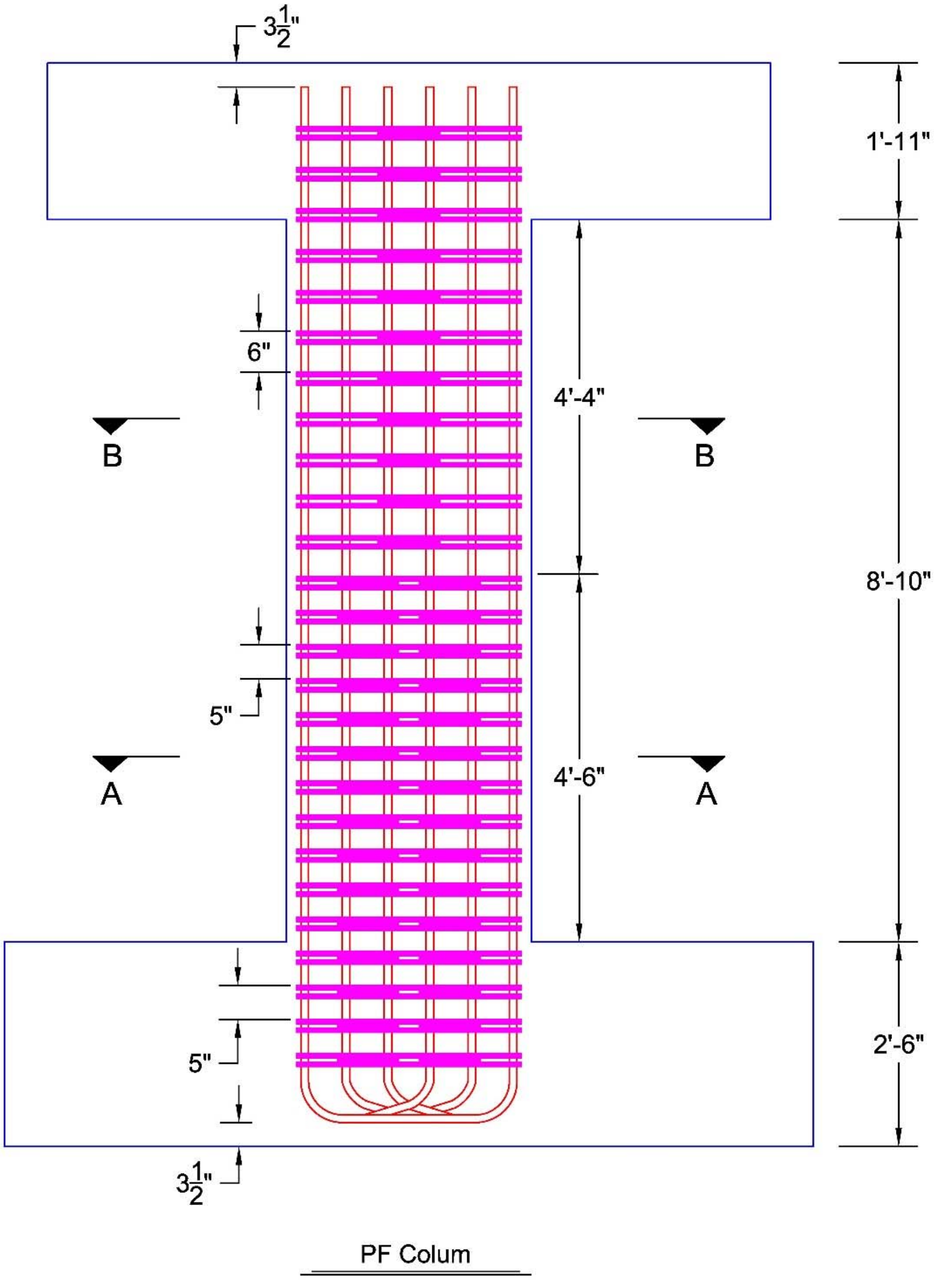

Figure A.1. Reinforcement Details for Perimeter Frame (PF) Column Specimens

(Designed and created by the author and reported by (Palacios, 2015))

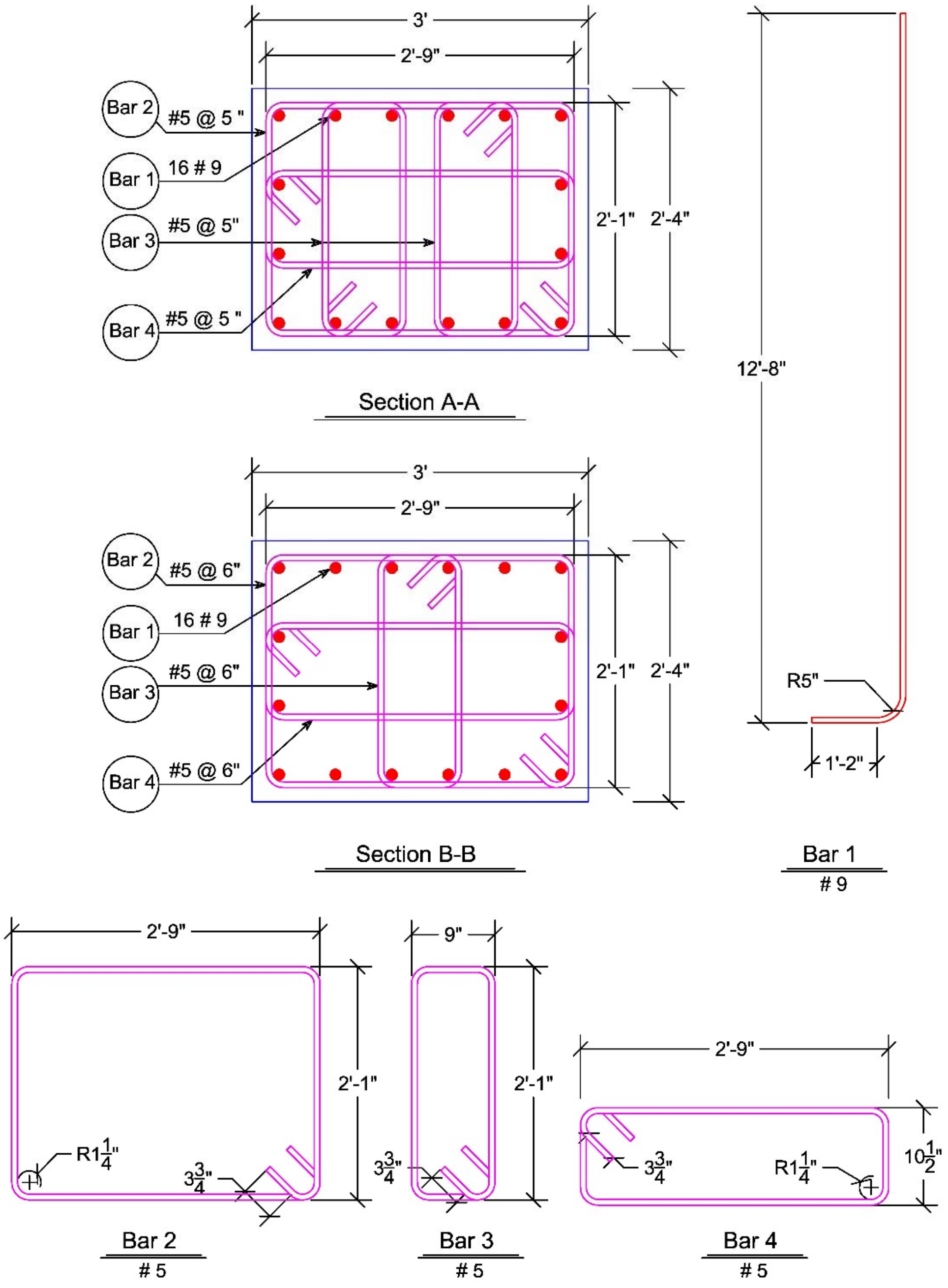

Figure A.2. Reinforcement Details for Perimeter Frame (PF) Column Specimens (Designed and created by the author and reported by (Palacios, 2015))

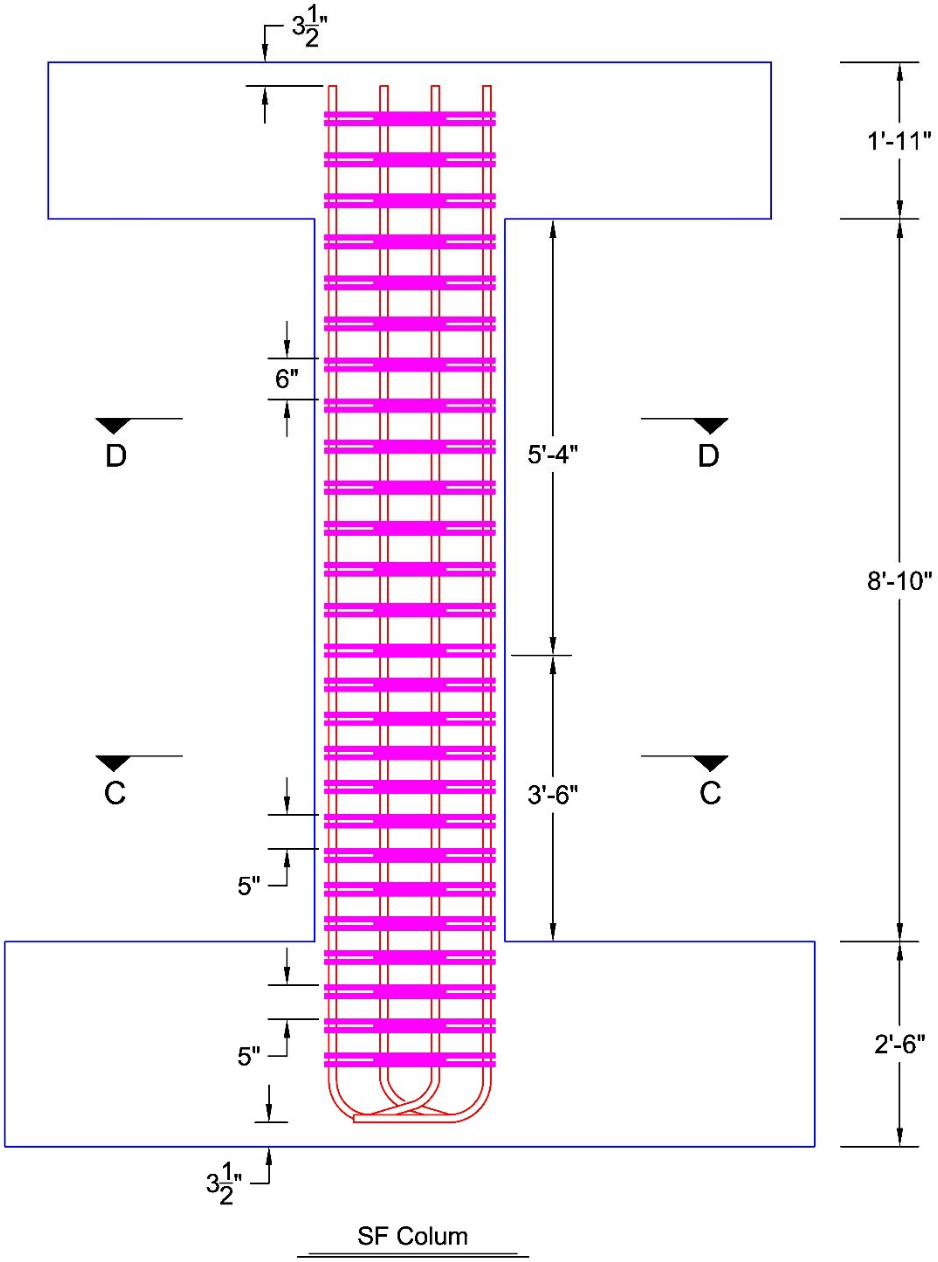

Figure A.3. Reinforcement Details for Space Frame (SF) Column Specimens

(Designed and created by the author and reported by (Palacios, 2015))

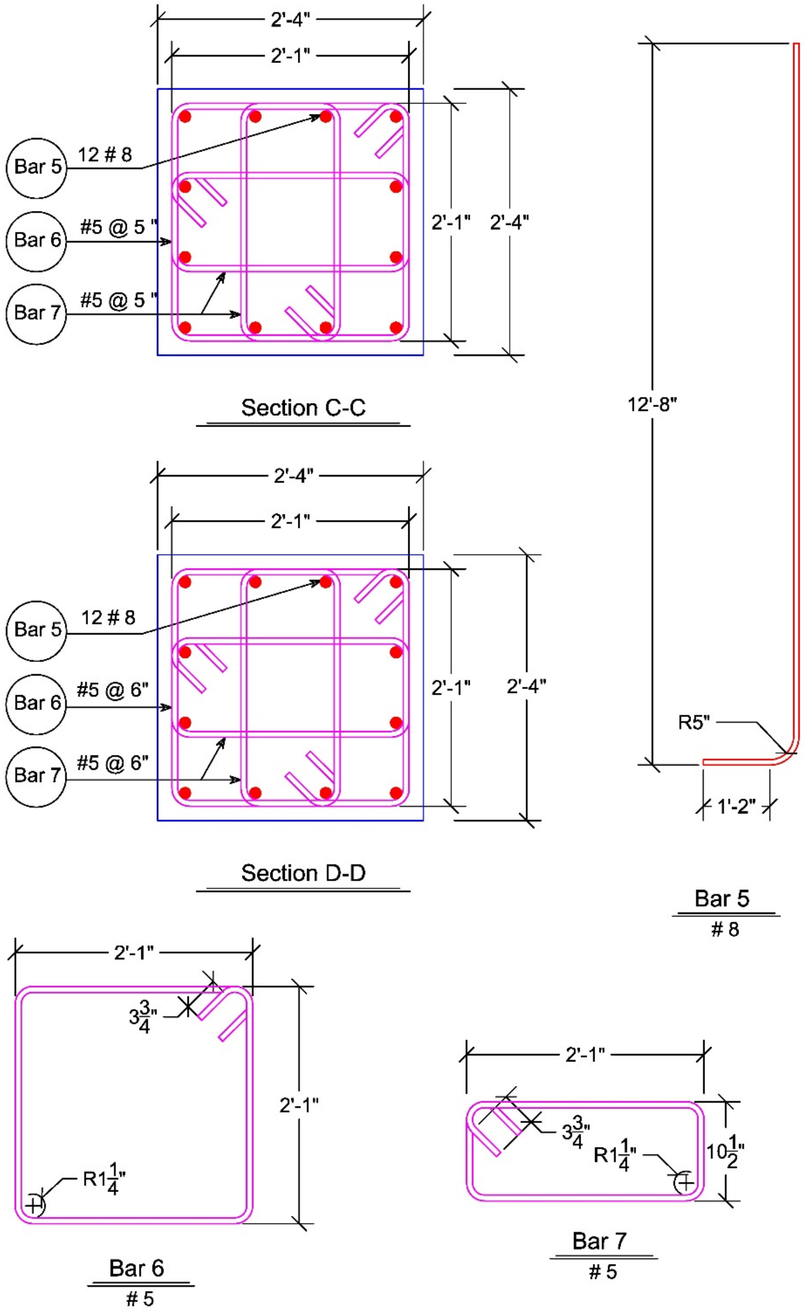

Figure A.4. Reinforcement Details for Space Frame (SF) Column Specimens

(Designed and created by the author and reported by (Palacios, 2015))

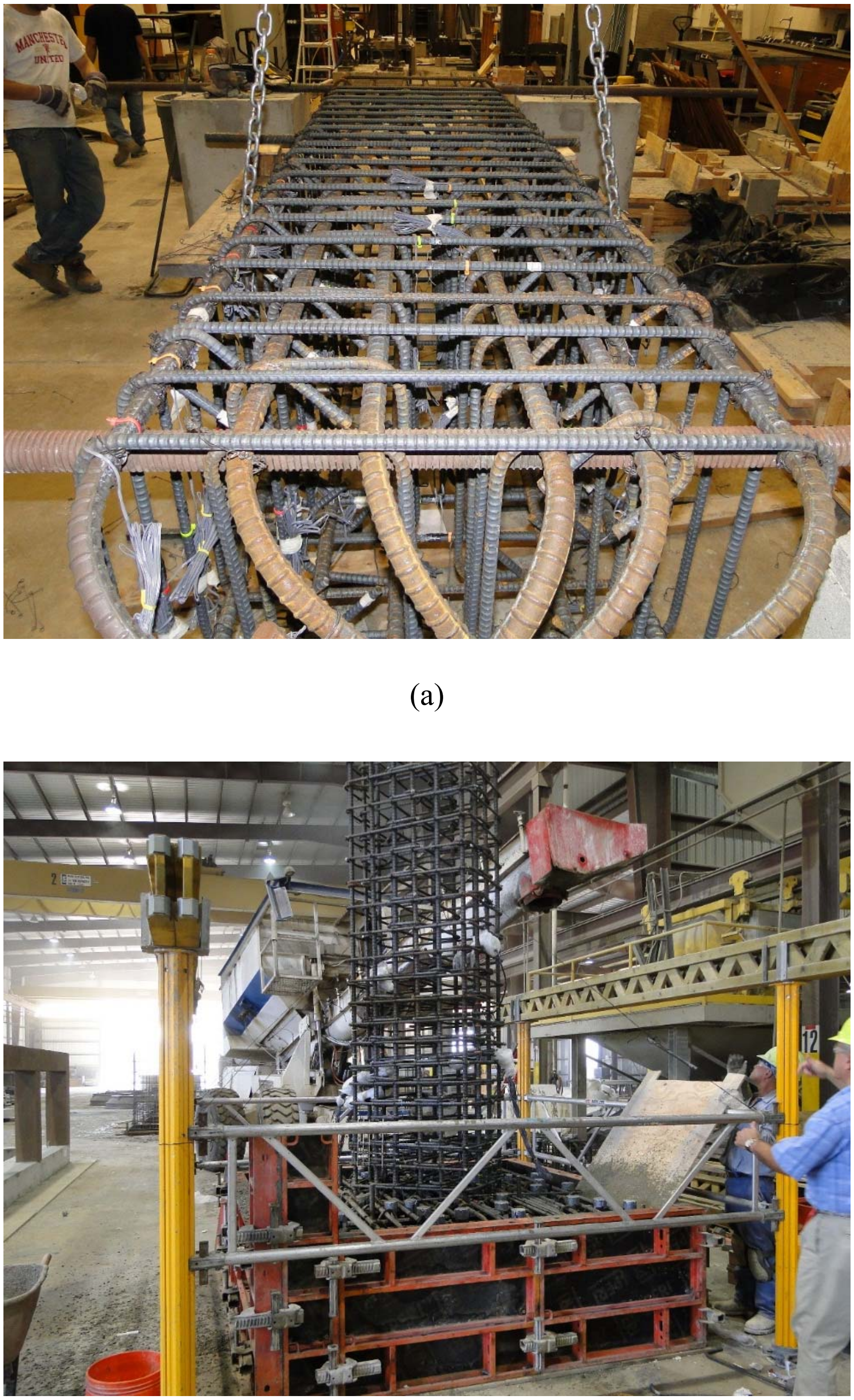

(a)

(b)

Figure A.5. (a) Building Reinforcing Cage, (b) Placing the Cage in the Forms

Figure A.6. Forming Column and Top Block

A.2. INSTRUMENTATION

Prior to pouring concrete, strain gages were installed on reinforcing bars, transverse hoops, and into the concrete. To install the strain gages on reinforcing bars, first the desired location of the strain gage on the bar was marked. The surface of the bar at the marked location was grounded, and sanded with 400 grit sandpaper to provide a smooth surface for the strain gage (Figure A.7). The smoothed surface of the bars were cleaned (Figure A.8). The gages were oriented so that pulling their wires out of the concrete would not require the wires to fold back and cause any damage to the gage wires. The gages were taped to the bar. The location of the strain gages were then coated with layers of polyurethane, nitrile rubber, moisture sealing electrical tape to protect the gages.

In addition, aluminum anchors were placed in the specimens prior to pouring the concrete (Figure A.9). These anchors were used when connecting the external sensors (i.e., LVDTs, string pots and tiltmeters) to the specimens at the MAST Lab (Figures A.10 and A.11).

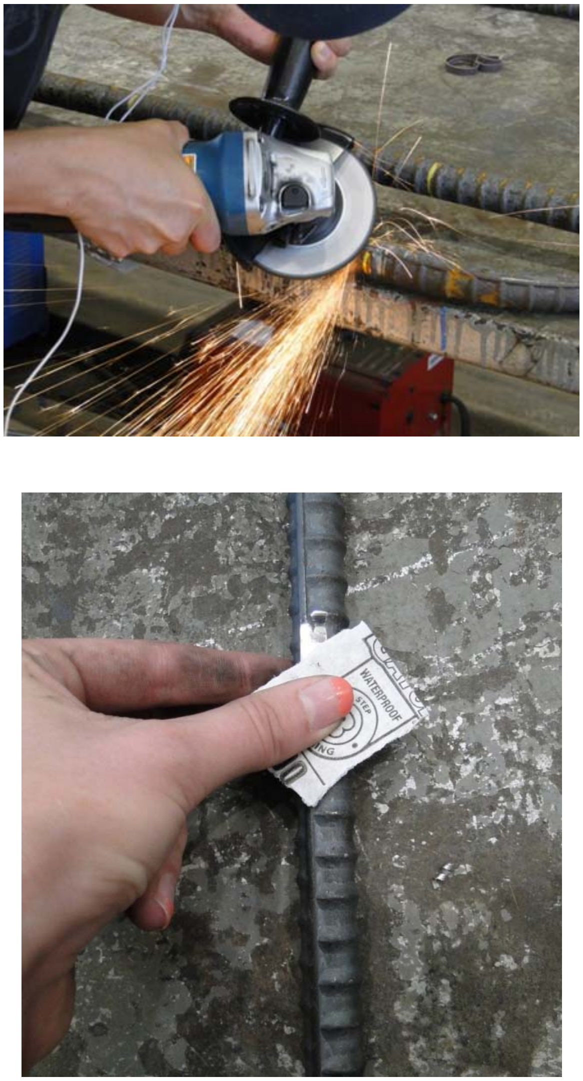

Figure A.7. Grinding and Cleaning of Bars Prior to Strain Gage Installation

Figure A.8. Attaching the Strain Gage to the Prepared Surface of the Bar

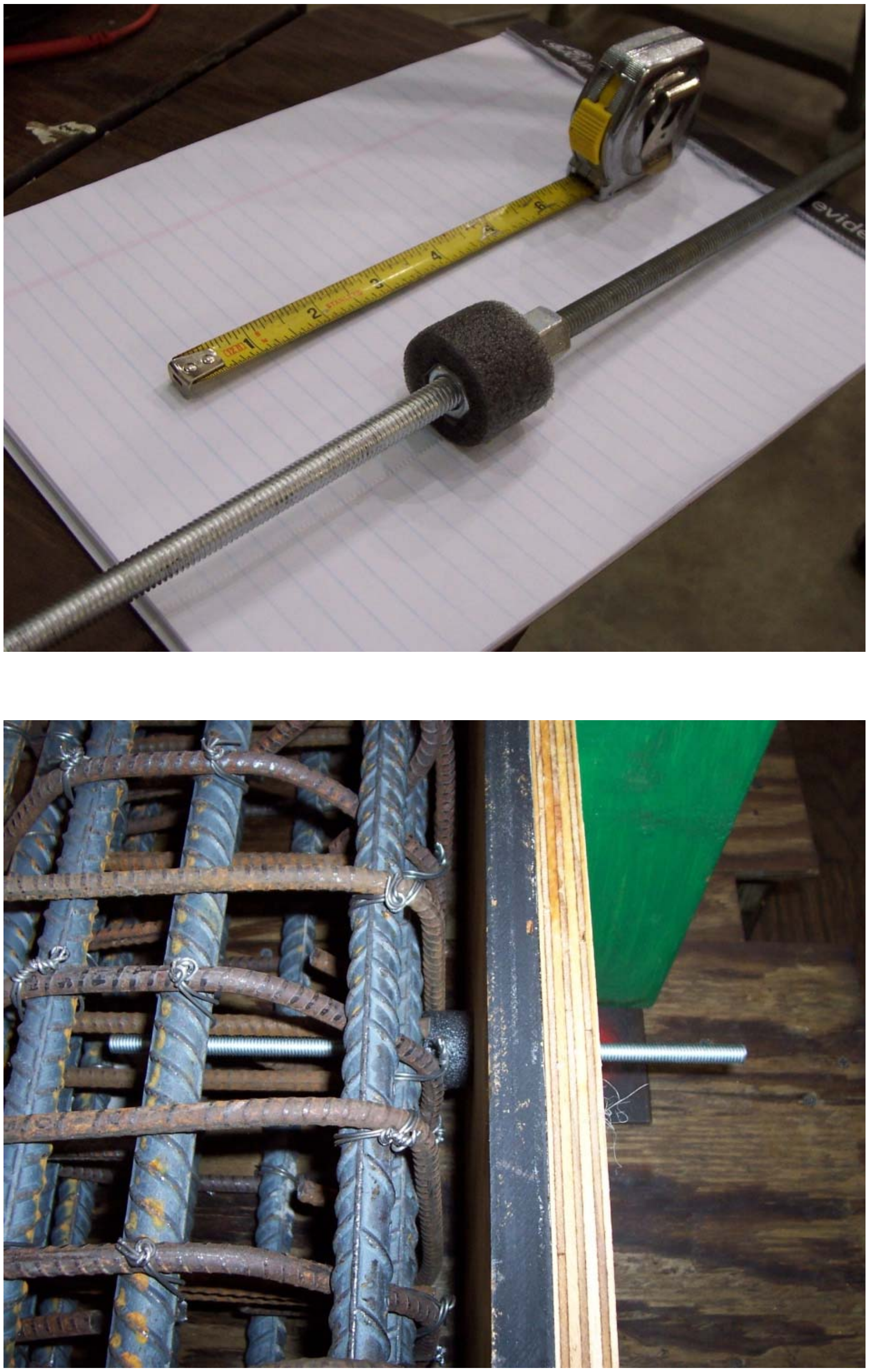

Figure A.9. Installation of an Aluminum Anchor for External Instrumentation

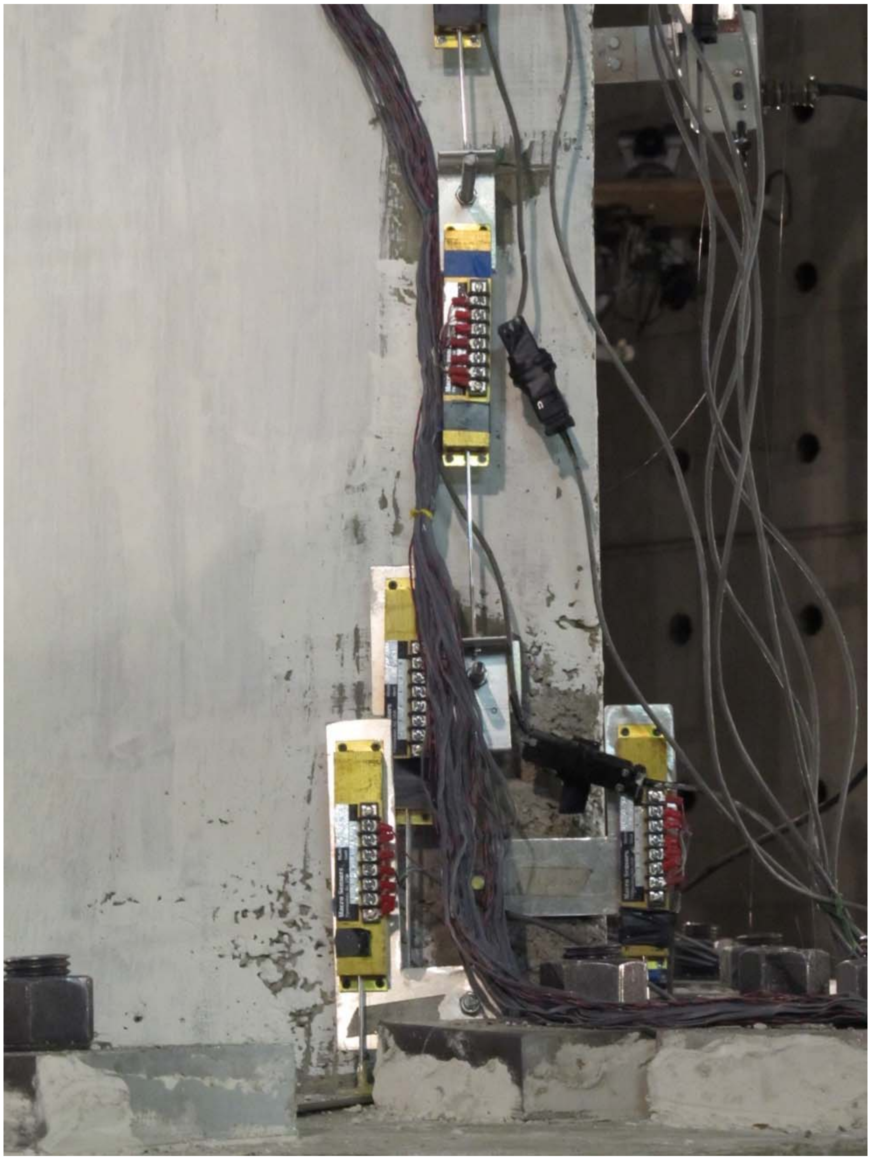

Figure A.10. Installation of Vertical LVDTs on SE Face of the Column

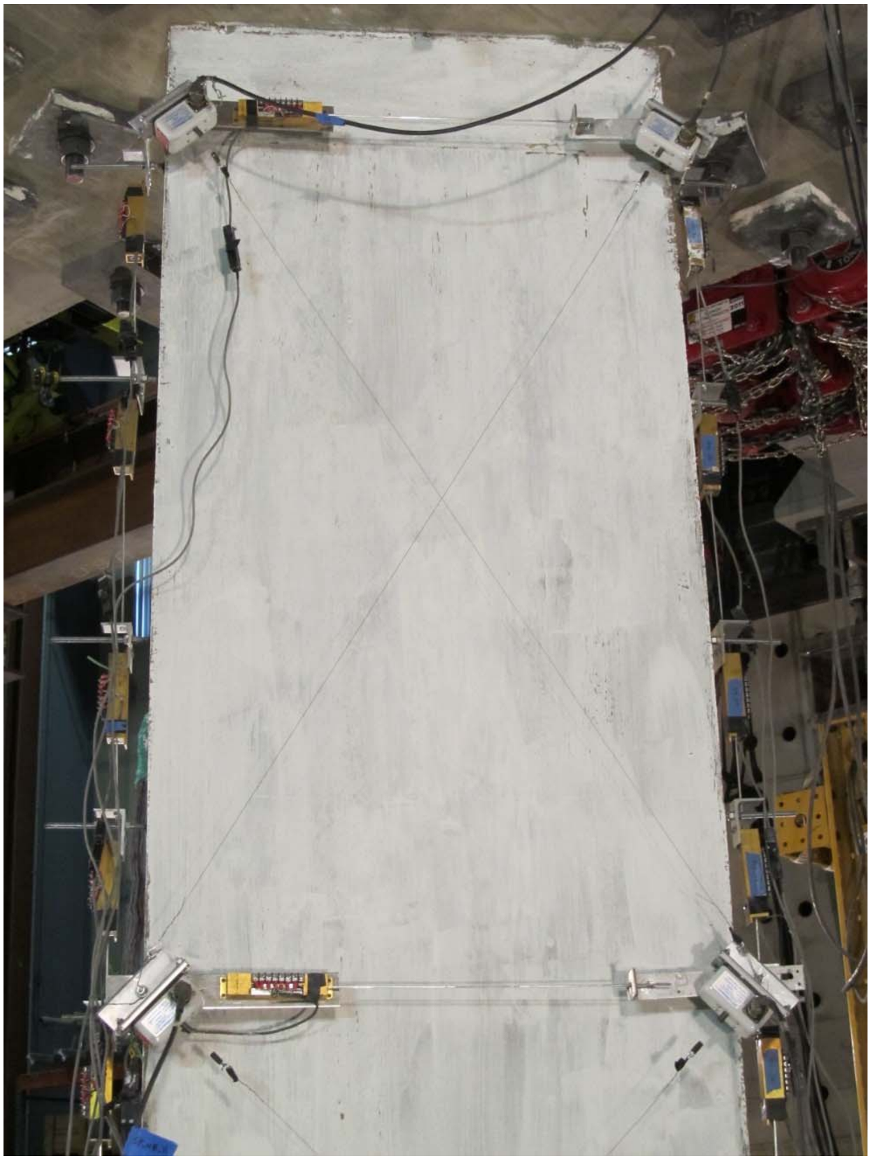

Figure A.11. Installation of LVDTs and String Pots on NE Face of the Column

A.3. SHIPPING AND INSTALLATION

To protect the specimens from tensile cracking, the specimens were post tensioned using four threaded rods, each 1 in. in diameter. Lifting and tilting of the specimens was carried out using 2 ½ in. holes that were designed in the footing and top blocks. Loading of the specimens at UTA, specimen shipping, unloading and tilting up the specimens at the MAST Lab are represented in Figures A.12 to A.16. At the MAST Lab, the specimens were placed on top of a three-piece spacer block that was constructed at the University of Minnesota so that the minimum required height condition for the loading crosshead is satisfied (Figures A.17, and A.18).

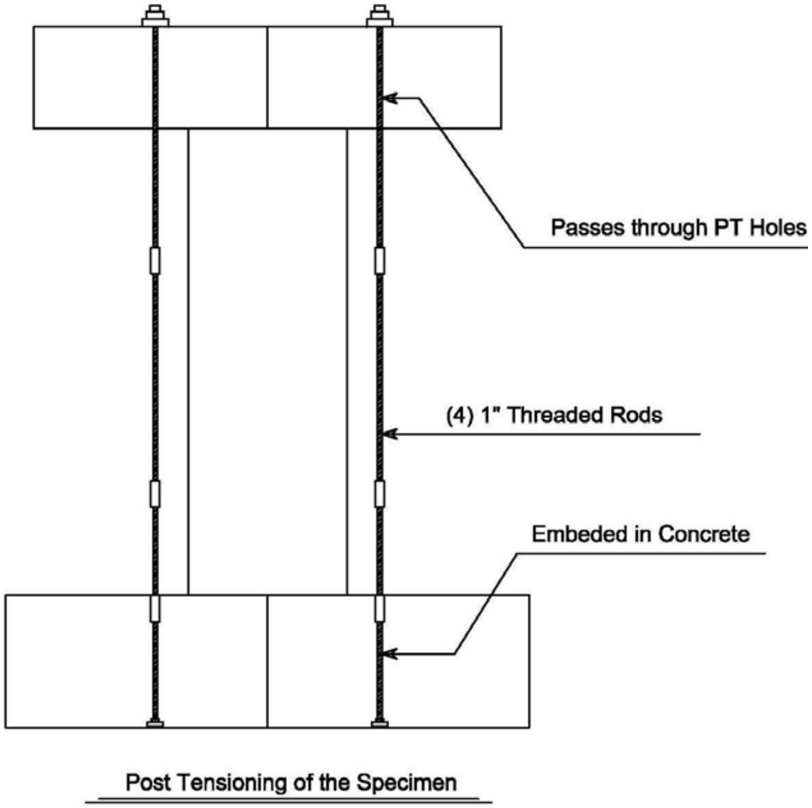

Figure A.12. Post Tensioning of the Specimen Prior to Shipping

Figure A.13. Lifting the Specimen Before Shipping

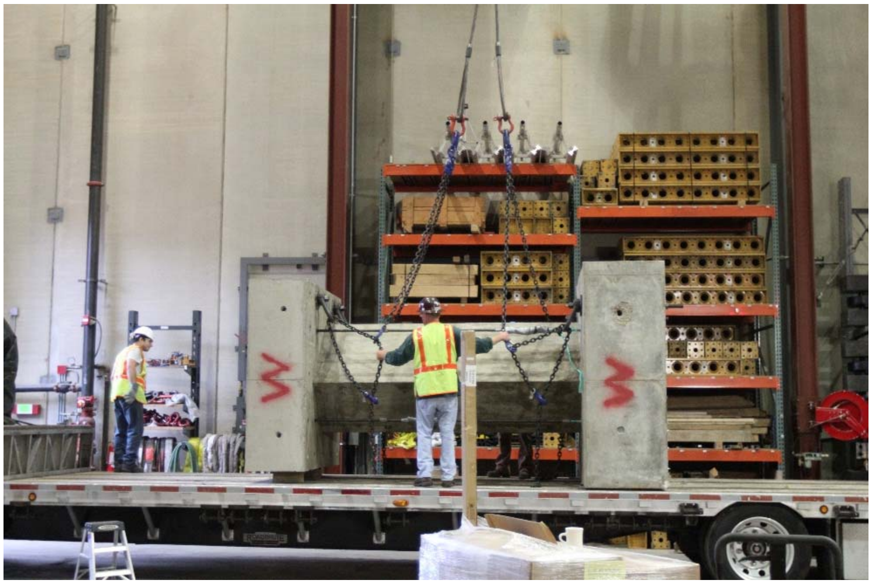

Figure A.14. Delivery of the Specimen to the MAST Lab

Figure A.15. Unloading the Specimen at the MAST Lab

Figure A.16. Tilting Up the Specimen at the MAST Lab

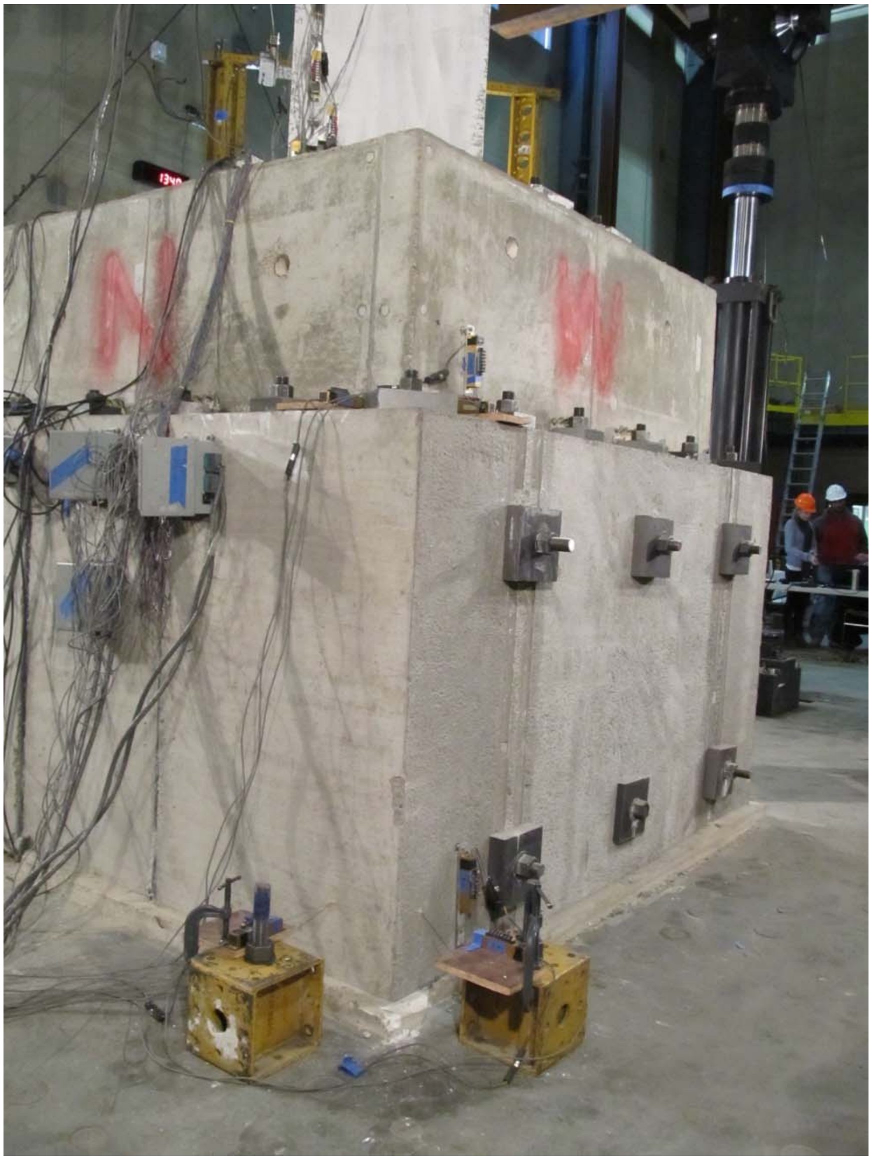

Figure A.17. Three-Piece Spacer Block

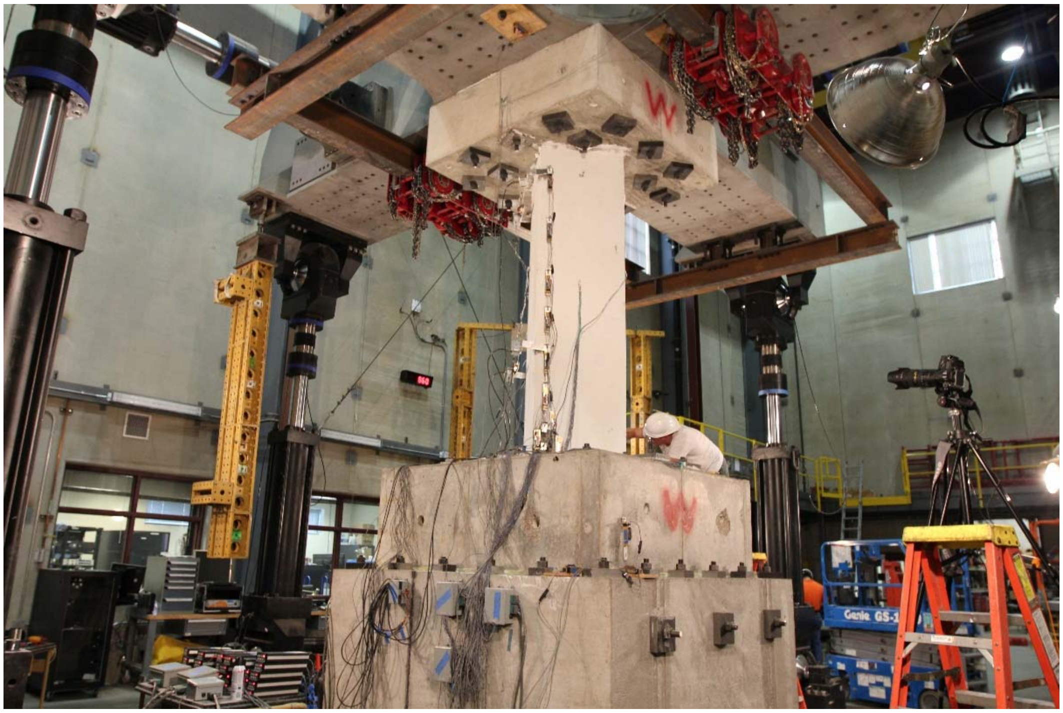

Figure A.18. Installation of the Specimen on Top of the Spacer Blocks